

**PONTIFICIA UNIVERSIDAD
CATÓLICA DEL PERÚ**

Escuela de Posgrado



Biopolymer composites as triboelectric layers for the
development of triboelectric nanogenerator (TENG)

Tesis para obtener el grado académico de Maestro en Ingeniería y

Ciencia de los Materiales que presenta:

Virgilio Brian Delgado De Lucio

Asesor:

Dr. Fernando Gilberto Torres García

Lima, 2023


Informe de Similitud

Yo, Fernando Gilberto Torres García, docente de la Escuela de Posgrado de la Pontificia Universidad Católica del Perú, asesor de la tesis titulada: "**Biopolymer composites as triboelectric layers for the development of triboelectric nanogenerator (TENG)**", del autor Virgilio Brian Delgado De Lucio,

dejo constancia de lo siguiente:

- El mencionado documento tiene un índice de puntuación de similitud de 17%. Así lo consigna el reporte de similitud emitido por el software *Turnitin* el 18/10/2023.
- He revisado con detalle dicho reporte y la Tesis Profesional no advierte indicios de plagio.
- Las citas a otros autores y sus respectivas referencias cumplen con las pautas académicas.

Lugar y fecha: San Miguel 18 de octubre de 2023

Apellidos y nombres del asesor: Torres García, Fernando Gilberto	
DNI: 07879100	Firma 
ORCID: 0000-0002-3123-266X	

ABSTRACT:

The escalating global energy demand, propelled by rapid industrial expansion, has underscored the imperative of transitioning to cleaner and more sustainable energy sources to combat pollution and mitigate the adverse effects of global warming. Triboelectric nanogenerators (TENGs) have emerged as a promising technology capable of harnessing ambient mechanical energy and converting it into electrical power. This research initiative seeks to advance the field by focusing on the development of composite materials derived from a synergy of biopolymers extracted from natural sources, particularly potatoes, and inorganic fillers.

The comprehensive objectives of this study encompass the extraction of biopolymers from natural resources, the meticulous characterization of composite materials to ascertain their mechanical, physicochemical, and morphological properties, the fabrication of TENGs employing these composite materials, and an exhaustive evaluation of the TENGs' performance metrics.

Remarkably, the composite materials exhibit outstanding dielectric properties, characterized by exceptional dielectric permittivity (ϵ) values. At a fundamental level, these materials showcase impressive dielectric constant (ϵ') values, with specific examples reaching into the millions at a frequency of 1 Hz. Furthermore, the dielectric loss (ϵ'') values, representing the imaginary component of permittivity, also exhibit notable characteristics. For instance, certain composite materials demonstrate ϵ'' values that mirror the remarkable ϵ' values, signifying their potential to excel in energy storage applications.

What sets this research apart is not only the development of materials with exceptional dielectric properties but also the exploration of their practical application in triboelectric nanogenerators. The TENGs fashioned from these composite materials consistently exhibit remarkable voltage outputs, further underscoring their potential for various energy harvesting applications.

ACKNOWLEDGEMENTS:

Firstly, I would like to express my deepest gratitude to my parents for their unconditional love, constant support, and unwavering faith in me throughout this journey. Thank you for being my guide, my pillar of strength, and my inspiration. Your words of encouragement and exemplary perseverance have brought me this far, and I couldn't be more thankful.

I would also like to thank my spouse, Erika, for being my life partner and my greatest emotional support. Thank you for understanding my long hours of study and work, for motivating me in the tough times, and for being my source of joy and motivation in the good times. Your love, patience, and understanding have been instrumental in my pursuit of this project.

Furthermore, I extend my heartfelt gratitude to PhD. Fernando Torres for their expert guidance and invaluable advice throughout this process. Your knowledge and skills have been crucial in the construction of this work.

Lastly, I want to thank all the individuals who have in some way contributed to the completion of this project, from my family and friends to my classmates and professors. Without their support, this work would not have been possible.

Thank you all from the bottom of my heart!

Virgilio Brian Delgado De Lucio

This work was financed by CONCYTEC-PROCIENCIA in the framework of the " Proyectos de Investigación Aplicada y Desarrollo Tecnológico 2020-02" contest [Contrato N° 166-2020-FONDECYT], Project "Fabricación de un nanogenerador triboeléctrico biodegradable (bioTENG) a partir de nanomateriales obtenidos de recursos renovables de la Sierra peru

CONTENT INDEX:

ABSTRACT:.....	1
ACKNOWLEDGEMENTS:	4
CONTENT INDEX:	5
FIGURE INDEX.....	7
TABLE INDEX.....	10
EQUATION INDEX	11
INTRODUCTION:	12
OBJECTIVES.....	15
CHAPTER 1. THEORETICAL FRAMEWORK.....	16
1.1 TENGs	16
1.1.1 Description	16
1.1.2 Working principle and physical phenomena	16
1.1.5 Types of TENGs.....	21
1.1.6 Strategies for increase electrical outputs.....	25
1.1.7 Materials for TENGs.....	29
1.1.8 Applications	35
1.2 Biopolymers	35
1.2.1 Starch.....	36
1.3 Inorganic fillers	38
1.4 Polymer Composites with ceramic fillers for high dielectric constants	40
Chapter 2. Materials and methods	42
2.1 SF-TENG assembly	42
2.2 Freestanding layer fabrication	44
2.2.1 Materials.....	44
2.2.2 Procedure	45
2.3 Materials Characterization	46
2.3.1 Dynamic Light Scattering (DLS) assay	46
2.3.2 Fourier Transform Infrared (FT-IR) Spectroscopy	47
2.3.3 Broad Band Dielectric Spectroscopy (BDS)	47
2.3 Test Bench	48

2.4 Electrical Tests	51
2.4.1 Open Circuit Voltage (Voc)	52
2.4.2 Short Circuit Current (Isc).....	53
2.4.3 Capacitor Charging and powering LEDs.....	54
Chapter 3 Result and Discussion	55
3.1 Dynamic Light Scattering Test results	55
3.2 Fourier Transform-Infrared Spectroscopy results	56
3.3 Broadband Dielectric Spectroscopy results	59
3.4 Electrical Outputs Results	62
3.4.1 Open Circuit Voltage	62
3.4.2 Short Circuit Current	74
3.4.3 Capacitor Charging	79
CONCLUSIONS	81
BIBLIOGRAPHY.....	82

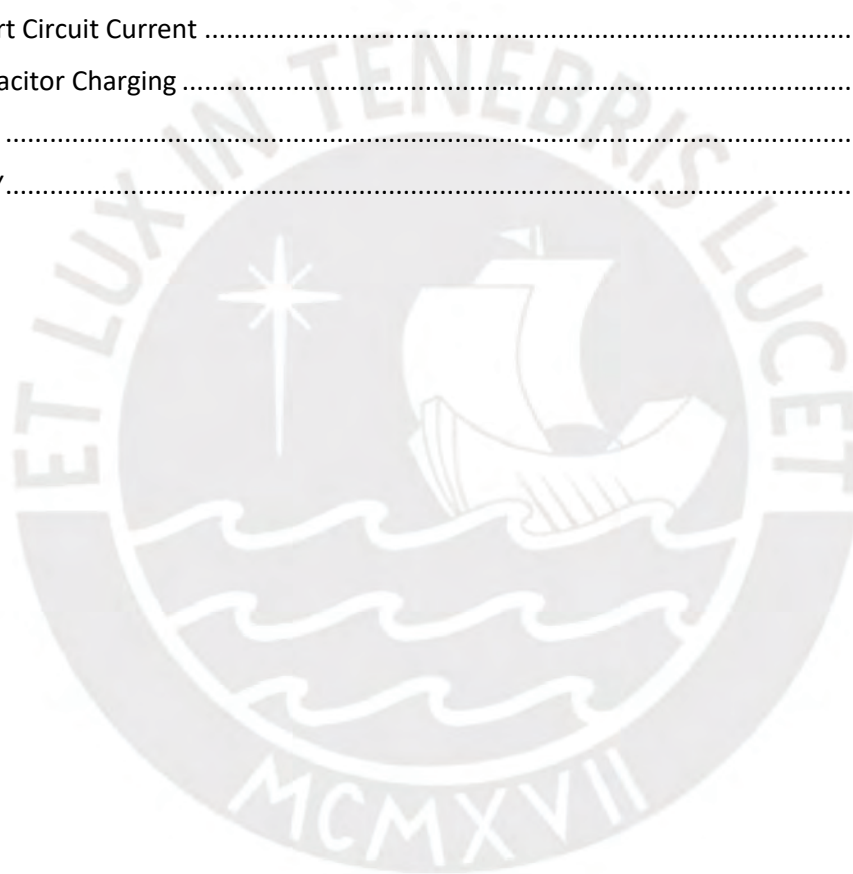


FIGURE INDEX

<i>Figure 1</i>	Schematic diagram of power generation principle of TENG by vertical contact separation mode. [27].....	19
<i>Figure 2</i>	Device structure of the TENG.....	23
<i>Figure 3</i>	Theoretical models of CFTENGs. (a) model of a typical dielectric freestanding layer CFTENG. (b) equivalent circuit model of the dielectric CFTENG electrostatic system. (c) model of a typical metal freestanding layer CFTENG.....	24
<i>Figure 4</i>	Fraction (%) of the electron acceptor, A, and donor, B, materials used in 100 randomly selected articles from 2012 to 2020.[13].....	30
<i>Figure 5</i>	The quantified triboelectric series. The error bar indicates the range within a standard deviation. Source data are provided as a Source Data file [41].....	32
<i>Figure 6</i>	Tribo-electric charge density is compiled with highly porous and deformable knitted fabrics made from twenty-one types of polymer fibers.[46].....	33
<i>Figure 7</i>	The triboelectric material series of polymeric materials and 2D material. Their chemical structures are shown on their right [47].....	34
<i>Figure 8</i>	Components of SF-TENG (1) Freestanding Layer, (2) Stator Layer, and (3) Electrodes[54].....	42
<i>Figure 9</i>	Sliding Freestanding Triboelectric Nanogenerator set up.....	44
<i>Figure 10</i>	Supplies: 1)Yungay Potato Starch, 2) Barium Titanate Oxide (BTO) 3) Distilled Water 200mL 4) Glycerol (Plasticizer) 4gr0.....	44
<i>Figure 11</i>	Instruments: 1) Electronic analytical balance 2) Laboratory magnetic stirrer (+heater) 3) pH test paper 4) Ultrasonic processor 5) Oven.....	45
<i>Figure 12</i>	A) Petri dish with the Starch/Composite film, B) Starch/Composite film before cutting, C) Starch/composite size, dimensions of 8x8 cm ²	46
<i>Figure 13</i>	Spectrum Two FT-IR Spectrometer.....	47
<i>Figure 14</i>	Novocontrol Alpha-A modular Broadband Dielectric System.....	48
<i>Figure 15</i>	Sliding Freestanding Triboelectric Nanogenerator bench setup.....	48
<i>Figure 16</i>	LMD Software Motion Terminal – Program Code.....	49
<i>Figure 17</i>	Sliding Freestanding Triboelectric Nanogenerator Bench 3D Drawing.....	50
<i>Figure 18</i>	Labjack Height of 8.1 centimeters.....	50
<i>Figure 19</i>	Sliding freestanding Triboelectric Nanogenerator with the oscillatory motion.....	51
<i>Figure 20</i>	Open Circuit Voltage Measurements Setup.....	52
<i>Figure 21</i>	Open Circuit Voltage Measurement Setup with Full Bridge Rectifier.....	53
<i>Figure 22</i>	1) Oscilloscope DPO 2022, 2) Low-Noise Preamplifier Model SR560 Stanford Research Systems	53
<i>Figure 23</i>	Capacitor charging and voltage measurement setup.....	54

<i>Figure 24</i>	Sliding Freestanding Triboelectric Nanogenerator Circuit for Capacitor Charging	55
<i>Figure 25</i>	BaTiO ₃ Nanoparticles Hydrodynamic Diameter distribution	56
<i>Figure 26</i>	BaTiO ₃ Nano-particles FT- IR Complete Spectrum.....	56
<i>Figure 27</i>	BaTiO ₃ Nano-particles FT- IR, Peaks on 502 cm ⁻¹ , 510 cm ⁻¹ correspond stretching modes in Ti-O (both normal and bending modes), respectively.....	57
<i>Figure 28</i>	BaTiO ₃ Nano-particles FT- IR, Peaks on 858 cm ⁻¹ , 1422 cm ⁻¹ , and 1749 cm ⁻¹ correspond Ti-OH, COO ⁻ , Ba-OH, respectively.	57
<i>Figure 29</i>	Pristine Starch FT- IR Spectrum	57
<i>Figure 30</i>	Starch/NP-BTO 0.25% w/w Composite FT- IR Spectrum.....	58
<i>Figure 31</i>	Starch/NP-BTO 0.50% w/w Composite FT- IR Spectrum.....	58
<i>Figure 32</i>	Starch/NP-BTO 0.75% w/w Composite FT- IR Spectrum.....	58
<i>Figure 33</i>	Starch/NP-BTO 1.00% w/w Composite FT- IR Spectrum.....	59
<i>Figure 34</i>	Starch/Composites FT – IR Spectra	59
<i>Figure 35</i>	The real part of the Dielectric Permittivity for Starch/Composite Samples.....	60
<i>Figure 36</i>	The real part of the Dielectric Permittivity for Starch/Composite Samples.....	60
<i>Figure 37</i>	Dielectric Loss of the Starch/Composite Samples.....	61
<i>Figure 38</i>	Dielectric properties of Starch/Composite samples	61
<i>Figure 39</i>	Open circuit voltage for FS-TENG Pristine Starch (f=1Hz)	62
<i>Figure 40</i>	Rectified Open circuit voltage for FS-TENG Pristine Starch (f=1Hz).....	62
<i>Figure 41</i>	Fast Fourier Transform of Pristine Starch Open circuit voltage Signal.....	63
<i>Figure 42</i>	Fast Fourier Transform of Pristine Starch Open circuit voltage Signal.....	63
<i>Figure 43</i>	Open circuit voltage for FS-TENG Pristine Starch (Random Movements)	64
<i>Figure 44</i>	Rectified Open circuit voltage for FS-TENG Pristine Starch (Random Movements)	65
<i>Figure 45</i>	Open circuit voltage for SF-TENG Starch/NP-BTO 0.25% w/w Composite (f=1Hz).....	65
<i>Figure 46</i>	Rectified Open circuit voltage for SF-TENG Starch/NP-BTO 0.25% w/w Composite (f=1Hz)	66
<i>Figure 47</i>	Open circuit voltage for SF-TENG Starch/NP-BTO 0.25% w/w Composite (Random Movements)	66
<i>Figure 48</i>	Rectified Open circuit voltage for SF-TENG Starch/NP-BTO 0.25% w/w Composite (Random Movements).....	67
<i>Figure 49</i>	Open circuit voltage for SF-TENG Starch/NP-BTO 0.50% w/w Composite (f=1Hz).....	68
<i>Figure 50</i>	Rectified Open circuit voltage for SF-TENG Starch/NP-BTO 0.50% w/w Composite (f=1Hz)	68
<i>Figure 51</i>	Open circuit voltage for SF-TENG Starch/NP-BTO 0.50% w/w Composite (Random Movements)	68
<i>Figure 52</i>	Rectified Open circuit voltage for SF-TENG Starch/NP-BTO 0.50% w/w Composite (Random Movements).....	69
<i>Figure 53</i>	Open circuit voltage for SF-TENG Starch/NP-BTO 0.75% w/w Composite (f=1Hz).....	70

<i>Figure 54</i>	Rectified Open circuit voltage for SF-TENG Starch/NP-BTO 0.75% w/w Composite (f=1Hz)	70
<i>Figure 55</i>	Open circuit voltage for SF-TENG Starch/NP-BTO 0.75% w/w Composite (Random Movements)	71
<i>Figure 56</i>	Rectified Open circuit voltage for SF-TENG Starch/NP-BTO 0.75% w/w Composite (Random Movements)	71
<i>Figure 57</i>	Open circuit voltage for SF-TENG Starch/NP-BTO 1.00% w/w Composite (f=1Hz)	72
<i>Figure 58</i>	Rectified Open circuit voltage for SF-TENG Starch/NP-BTO 1.00% w/w Composite (f=1Hz)	72
<i>Figure 59</i>	Open circuit voltage for SF-TENG Starch/NP-BTO 1.00% w/w Composite (Random Movements)	73
<i>Figure 60</i>	Rectified Open circuit voltage for SF-TENG Starch/NP-BTO 1.00% w/w Composite (Random Movements)	73
<i>Figure 61</i>	Rectified Open circuit voltage for SF-TENG Starch/NP-BTO 1.00% w/w Composite (Random Movements)	73
<i>Figure 62</i>	Voltage Measurements taken by Oscilloscope DPO2022	74
<i>Figure 63</i>	Short circuit current for FS-TENG Pristine Starch (f=1Hz)	74
<i>Figure 64</i>	Rectified Short circuit current for -SF-TENG Pristine Starch (f=1Hz)	75
<i>Figure 65</i>	Short circuit current for SF-TENG Starch/NP-BTO 0.25% w/w Composite (f=1Hz)	75
<i>Figure 66</i>	Rectified Short circuit current for SF-TENG Starch/NP-BTO 0.25% w/w Composite (f=1Hz)	76
<i>Figure 67</i>	Short circuit current for SF-TENG Starch/NP-BTO 0.50% w/w Composite (f=1Hz)	76
<i>Figure 68</i>	Rectified Short circuit current for SF-TENG Starch/NP-BTO 0.50% w/w Composite (f=1Hz)	77
<i>Figure 69</i>	Short circuit current for SF-TENG Starch/NP-BTO 0.75% w/w Composite (f=1Hz)	77
<i>Figure 70</i>	Rectified Short circuit current for SF-TENG Starch/NP-BTO 0.75% w/w Composite (f=1Hz)	77
<i>Figure 71</i>	Short circuit current for SF-TENG Starch/NP-BTO 1.00% w/w Composite (f=1Hz)	78
<i>Figure 72</i>	Rectified Short circuit current for SF-TENG Starch/NP-BTO 1.00% w/w Composite (f=1Hz)	78
<i>Figure 73</i>	Starch/Composite Freestanding layers charging 3.4uF Capacitor	79

TABLE INDEX

Table 1 :	Materials for SF - TENGs.....	42
Table 2 :	FS-TENG componets size	43
Table 3 :	Dielectric properties for composite samples	61
Table 4 :	Maximum FS-Teng outputs registered.....	80



EQUATION INDEX

(Eq. 1) 18
(Eq. 2) 20
(Eq. 3) 20
(Eq. 4) 21
(Eq. 5) 22



INTRODUCTION:

In the last years, the energy demand has been increasing rapidly due to the expanding industrial activity caused by the development of society and the economy.[1] Many energy sources as the traditional (e.g., coal, oil, and gas) have been contributing to global electrical power generation. [2] Nevertheless, they also have a strong contribution to pollution owing to the emission of greenhouse gases and other air contaminants. [3]. Renewable energy sources provide an excellent opportunity for reducing the aforementioned issue and reducing global warming, its sharing in the total energy utilized has increased in recent years. [1]

Besides the well-known renewable sources such as solar, wind, wave, and so on, there are others which have been never regarded before. One of them is environmental random energy sources like human walking, body shaking, hand touching, rain dropping, wheel rotation, and machine roar. [4] Whilst they are identical in principle to large-scale renewable energy generation, the amount of energy produced is much smaller being typically tens of microwatts to a few watts [5] which is the scale of nano/micro energy. This allows to us make an introduction to a new concept is Energy harvesting (also called Energy scavenging) which is the conversion of environmental energy into electrical energy for use in self-powered electronic devices or circuits.

New electronic technology follows the trend of miniaturization, portability, and functionality which means that each people can have at least dozens to hundreds of such small electronics. Powering by batteries such electronics along with the recently growing demand for sensors by emerging Internet of Things (IoT) at any time will become impractical. Considering the following drawbacks that this entails: (1) huge number of batteries to power them, (2) large scope of distribution, (3) difficulty to track (4) and poor recyclability, it implies environmental impact and possible health hazards. Hence, other power sources for independent and continuous operations of such small electronics are needed. [6]

At this point, energy harvesters such as nanogenerators make their entrance as batteries green alternative. The first one was developed by Wang and coworkers in 2006 to scavenge ambient mechanical energy based on the piezoelectric effect. [7] Its mechanism is the induction of an electric charge in response to an applied mechanical strain [8] its nature is

closely related to the generation of electric dipole moments in solids. The dipole moments may either be induced by ions on crystal lattice sites with asymmetric charge surroundings may be carried by molecular groups directly.[9].

In January 2012, the triboelectric nanogenerator (TENG) was invented. This device is considered a powerful technology for transforming random mechanical energy from the environment into electricity. TENGs' mechanism is based on the coupling of triboelectrification and electrostatic induction, with unique benefits of low weight, high-power density, high efficiency, and low fabrication cost. [7] TENGs use Maxwell's displacement current as the driving force for effectively converting mechanical energy into electric power/signal, regardless of whether nanomaterials are used or not. [10]. An electrical potential between the surfaces is initiated, when the charges are moved apart on the contact surfaces. There are four basic working modes of the TENGs, that are classifying depending on the direction of the polarization alteration and electrode configuration, including vertical contact-separation (CS) mode, lateral sliding (LS) mode, single-electrode (SE) mode, and freestanding triboelectric-layer (FT) model [11]

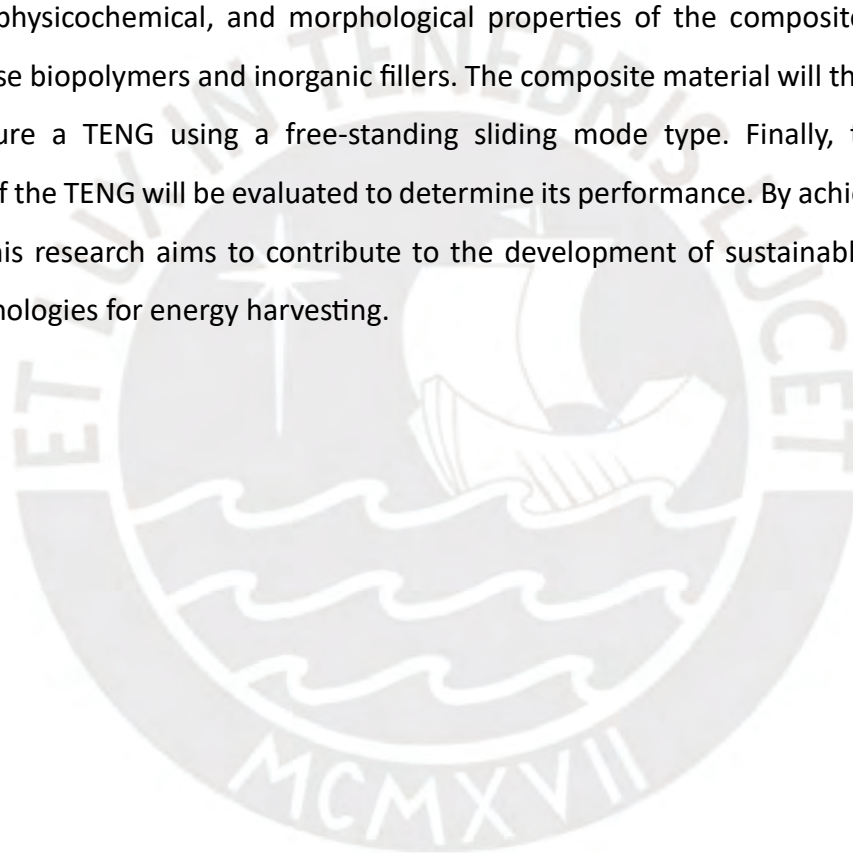
Until now, there are many studies that focus on the output TENGs performance improvement of system design and circuit design. However, studies regarding the design of materials have not been so exploited. It is because the mesoscopic understanding of the electrification mechanism is not well set, TENGs materials are restricted to a few species. The main strategy to enhance the output electric power of TENGs have been increase the charge generation, due to the performance of TENGs is proportional to the charge density of the contact surface and also the square of the charge density is the main framework used to quantify a TENG's performance as a material figure of merit.[12]

Other approaches from the materials perspective in order to increase the electrical TENGs outputs have been reported. These approaches incorporate increasing the contact area by fabricating microscale or nanoscale surface structures, surface functionalization to expand the surface charge density or to ease triboelectric charge transfer, alteration of the surface property by electrical poling or doping, and creation of new materials by molecular synthesis or nanocomposite formation. Changing the intrinsic material properties (dielectric constant, polarity, work function, etc.) has been pursued through nanocomposite formation, electrical poling, chemical doping, and material synthesis. In an effort to improve charge generation, nanocomposite materials have been studied extensively.[12]

Exist a necessity for a better understanding of the triboelectric effect of the materials, how the chemical composition of the materials and the interaction of the triboelectric layers are correlated with the charge density [13]

According to Kim in 2020 “A material with a high dielectric constant can be a good candidate for high-density charge generation”[12]

The aim of this research is to develop a composite material using biopolymers and inorganic fillers for use as triboelectric layer surfaces in the fabrication of triboelectric nanogenerators. The first step will be to obtain biopolymers from natural resources such as potato and microorganisms. The next phase will involve developing and characterizing the mechanical, physicochemical, and morphological properties of the composite materials based on these biopolymers and inorganic fillers. The composite material will then be used to manufacture a TENG using a free-standing sliding mode type. Finally, the output parameters of the TENG will be evaluated to determine its performance. By achieving these objectives, this research aims to contribute to the development of sustainable and eco-friendly technologies for energy harvesting.



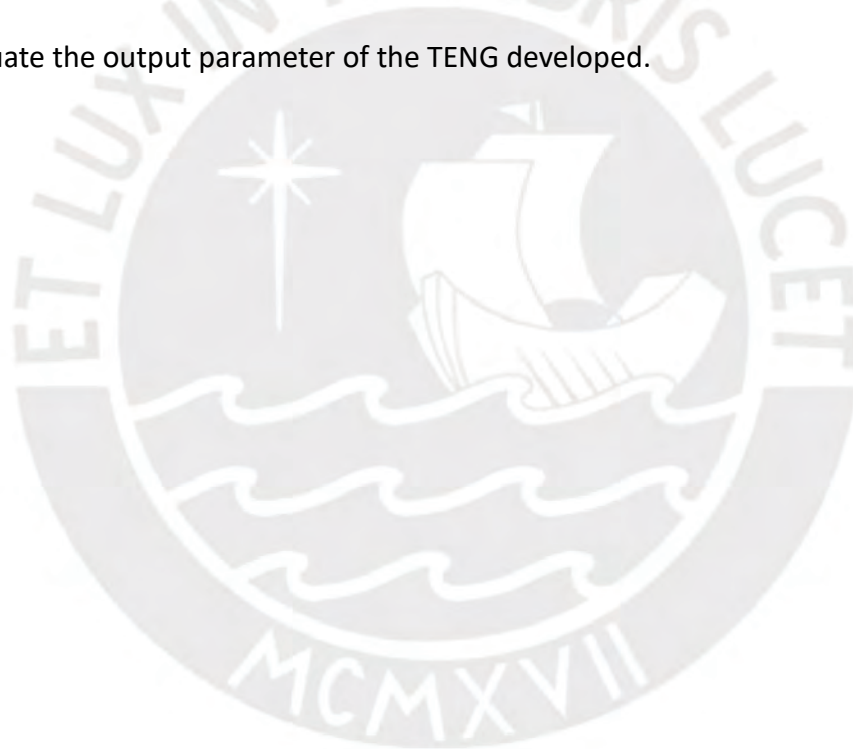
OBJECTIVES

1. General Objective

- To develop composite based on biopolymer and inorganic filler to be use as triboelectric surfaces to fabricate triboelectric nanogenerator.

2. Specific Objectives:

- To obtain biopolymers from natural resources such as potato and microorganism
- To develop and characterize the mechanical, physicochemical and morphological properties of composite materials based on biopolymers and inorganic fillers
- To manufacture a TENG using a free-standing sliding mode type.
- To evaluate the output parameter of the TENG developed.



CHAPTER 1. THEORETICAL FRAMEWORK

1.1 TENGs

1.1.1 Description

Triboelectric Nanogenerators, which were invented by Dr. Zhong Lin Wang from the Georgia Institute of Technology, are a novel technology designed to generate electrical energy by utilizing residual mechanical energy sometimes called randomly distributed, irregular, and wasted low-frequency energy source.[10] These sources such as human motion, mechanical vibration, wind, ocean waves and so on[14] typically involve the friction or contact between different materials, and by applying a mechanical force on the TENG, electric charges are produced. TENGs have many potential applications due to their high-power density, high efficiency, low weight, and low fabrication cost[14] also can harvest electrical energy from a variety of sources, and their durability, flexibility, and cost-effectiveness make them particularly useful for energy generation in difficult environments and in developing countries with limited energy resources.[15]

1.1.2 Working principle and physical phenomena

The triboelectric nanogenerator (TENG) works based on the coupling effect of contact electrification phenomenon also known as Triboelectric effect and electrostatic induction[14]. Contact electrification which is a phenomenon that occurs when two different materials come into contact and then separate. When the two materials come into contact, electric charge are transferred from one material to the other, this charge transfer can be of different types, such as transfer of electrons, ions, or nanomaterial[16,17]. However, recent studies show that most of the charge transferred in TENGs is due to the transfer of electrons[18,19], this last mechanism arise due to differences in their electron affinity and work function of the contacted layers. This results in the formation of positive and negative charges on the two surfaces. Contact electrification can also result in the formation of a mosaic of surface charges on the two surfaces in contact. This occurs due to the spatial distribution of different charge carrier densities on the surface,

resulting in a mosaic-like pattern of surface charges. [20,21] When the materials are separated, the positive and negative charges remain on their respective surfaces, creating an electric potential difference between them. This potential difference can be used to generate an electrical current.[22].

The phenomenon of electrification can be explained by three different models, each of which is related to the types of materials that are in contact.

The first model is the band structure model, which is used when one surface is made of a metallic material and the other is made of a dielectric material. In this model, the metallic material is defined by the Fermi distribution of its electrons, which depends on the temperature of the material. On the other hand, the dielectric material is defined by its molecular orbitals. When the two surfaces come into contact, the electrons in the metallic material have more energy than the unoccupied molecular orbitals on the surface of the dielectric material. As a result, the electrons from the metallic material can jump to lower energy levels in the dielectric material, explaining why dielectrics are considered electron acceptors in contact with metals.[13,18,23]

The second model is the molecular orbital model, which is used to describe charge transfer between two dielectric materials. In this model, the transfer of charge is explained by the overlap of the molecular orbitals of the two materials. When the two surfaces come into contact, the molecular orbitals on each surface overlap, allowing for the transfer of electrons between the two materials.[13,24]

The third model was proposed by Wang and uses potential wells to explain electron transfer. As the two surfaces approach each other, the potential barriers between the surfaces overlap, and the wave functions that describe these potential wells combine. This results in a decrease in the barrier, facilitating the transfer of electrons from wells with higher energy levels to those with lower energy levels through quantum tunneling.[13,25]

In summary, the three models of electrification by contact each describe different mechanisms by which electric charge can be transferred between two surfaces. The band structure model is used when one surface is metallic and the other is dielectric, the molecular orbital model is used when both surfaces are dielectric, and the potential well model is used to explain electron transfer through quantum tunneling.

The phenomenon of permanent charges generated during contact and resulting polarization is central to the functioning of Triboelectric Nanogenerators (TENGs). The polarization effect generated by electrification is best described using Maxwell's equations, which govern all electromagnetic phenomena. These equations provide a mathematical framework to describe how electric and magnetic fields interact with each other and with matter. Specifically, the equations introduce a new term called Polarization P_s , which is generated by the electrification of the TENG sheets during contact. By taking into account this new term, the Maxwell equations can be used to model and analyze the behavior of TENGs and predict their output parameters such as voltage, current and power. [26], Rewriting Maxwell's equations in terms of polarization (P_s):

$$\begin{aligned}
 \epsilon \nabla \cdot \mathbf{E} &= \rho - \nabla \cdot \mathbf{P}_s, \\
 \nabla \cdot \mathbf{B} &= 0, \\
 \nabla \times \mathbf{E} &= -\frac{\partial \mathbf{B}}{\partial t}, \\
 \nabla \times \mathbf{H} &= \mathbf{J} + \epsilon \frac{\partial \mathbf{E}}{\partial t} + \frac{\partial \mathbf{P}_s}{\partial t}.
 \end{aligned}$$

(Eq. 1)

The vertical separation-contact model of a TENG consists of two dielectric layer that are attached to an electrode at each end, which in turn are connected to an electrical resistance. The TENG's operation can be explained step by step as follows:

1. Both dielectric surfaces are brought into contact, allowing for electrification by contact to occur.

2. As a result of the contact electrification, a polarization occurs on the surfaces, generating permanent charges of opposite sign on each surface.
3. When the two dielectric surfaces are separated, the positive charges on one surface attract the electrons of its electrode towards itself, while the negative charges on the other surface repel the electrons from its electrode. This generates a current in the opposite direction to the movement of the electrons by convention.
4. The flow of current ceases at the end of separating the surfaces to a maximum distance. The TENG then moves on to the next half of the cycle, producing a current in the opposite direction.

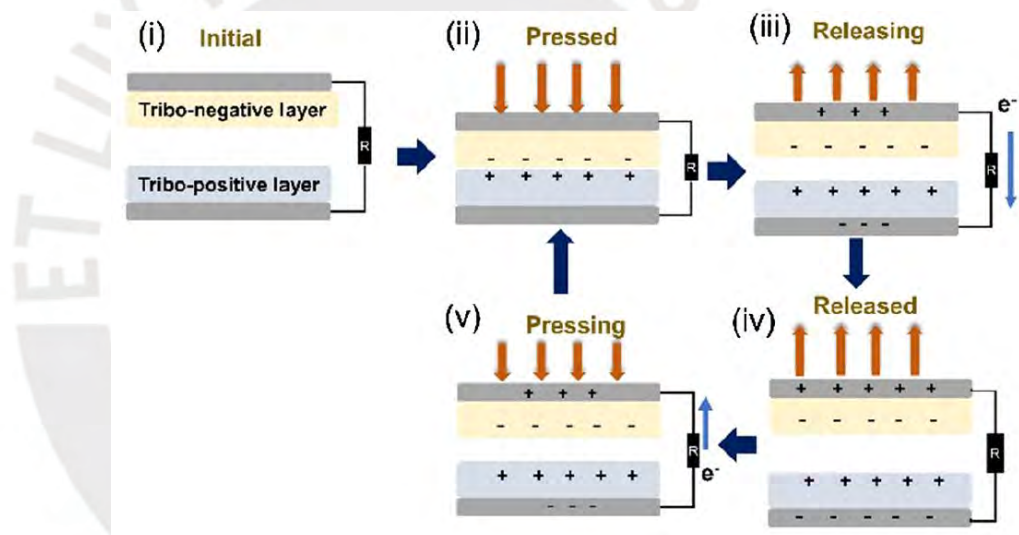


Figure 1 Schematic diagram of power generation principle of TENG by vertical contact separation mode. [27]

During the operation of the TENG, there are currents and voltages that depend on time. Therefore, it is possible to derive expressions for these parameters that can be considered as design parameters. These design parameters can then be optimized to improve the performance and efficiency of the TENG.

Therefore, it is possible to derive expressions for these parameters that can be considered as design parameters. These design parameters can then be

optimized to improve the performance and efficiency of the TENG. The following equation is the expression of the current density taking into account the model described above:

$$J_D = \sigma_T \frac{dH}{dt} \frac{d_1 \varepsilon_0 / \varepsilon_1 + d_2 \varepsilon_0 / \varepsilon_2}{(d_1 \varepsilon_0 / \varepsilon_1 + d_2 \varepsilon_0 / \varepsilon_2 + z)^2} + \frac{d\sigma_T}{dt} \frac{H}{d_1 \varepsilon_0 / \varepsilon_1 + d_2 \varepsilon_0 / \varepsilon_2 + z}$$

(Eq. 2)

The second part of the equation refers to the changes in the saturation of the charge within the dielectric layer over a series of contact cycles. Eventually, the saturation reaches a maximum and the term becomes zero, which typically happens after around 10 cycles of contact and detachment. After this transient part, the equation can be reduced to a simpler form that relates the charge density of the dielectric layer to the current density of the TENG.

$$J_D \approx \underbrace{\sigma_T}_{(P_1)} \underbrace{\left(\frac{dH}{dt} \right)}_{(P_2) \text{ Device}} \underbrace{\left(\frac{d_1 \varepsilon_0 / \varepsilon_1 + d_2 \varepsilon_0 / \varepsilon_2}{(d_1 \varepsilon_0 / \varepsilon_1 + d_2 \varepsilon_0 / \varepsilon_2 + z)^2} \right)}_{(P_3)}$$

(Eq. 3) **Triboelectric effect** **Electrostatic induction**

There are three expressions that can be customized based on the desired characteristics. The first expression, denoted as P1, represents the charge density of the dielectric material, which is influenced by various factors such as the chemical composition of the materials, their interaction during contact, and their mechanical properties such as elasticity and friction. The second expression, P2, describes the operating mode of the TENG, with the contact or sliding speed playing a crucial role. The third expression, P3, is a function of the geometry of the surfaces in contact, the distance between them, and the dielectric constants of the materials involved[13,28]. In the same way it is possible to obtain the expression for the potential drop between both layers.

$$\Phi_{AB} = -\sigma(z, t)[d_1/\varepsilon_1 + d_2/\varepsilon_2] - H(t)[\sigma(z, t) - \sigma_T]/\varepsilon_0$$

(Eq. 4)

These constitutive equations can be used to optimize the design of the TENG by choosing materials with desirable dielectric properties, such as high permittivity.

1.1.5 Types of TENGs

TENGs can be classified into various working modes[29] based on their operational principles and design configurations. The number of working modes can vary, depending on the specific criteria used for categorization. These criteria may include factors such as the type of materials used, the structural arrangement of the device, or the specific application requirements.

In terms of types and designs, there exist several variations of triboelectric nanogenerators, each offering its own unique features and configurations. These variations allow for customization and optimization of TENGs for different purposes. For example, one design might focus on maximizing the surface area of contact between the materials to enhance charge transfer[30], while another design could prioritize flexibility and portability for wearable applications [31,32].

Furthermore, the number of working modes for TENGs can be influenced by the categorization criteria employed. As the field of triboelectric nanogenerators continues to advance, the understanding and classification of these devices' working modes will likely evolve, leading to new insights and improvements in their design and functionality.

Next, we will delve into the main working modes of triboelectric nanogenerators, exploring their diverse approaches to charge generation, separation, and collection.

Contact-mode

The Triboelectric Nanogenerator (TENG) operates in contact mode and involves two fundamental processes. Firstly, during Contact Electrification, when two materials with varying electron affinities make contact and then separate, there is a transfer of electrons between them due to differences in their electronegativities. This transfer results in the accumulation of charges on the surfaces of the materials involved, causing one material to become negatively charged (with excess electrons) and the other positively charged (electron-deficient).

Secondly, there is Electrostatic Induction that occurs after the contact electrification. When the two materials are separated, an electric potential difference or voltage is established between them due to the earlier charge transfer during contact. This voltage leads to the accumulation of charges of opposite polarity on the electrodes connected to the materials, creating an electric current when a closed circuit is formed.

To describe this process mathematically, an equation for the metal-to-dielectric contact-mode TENG can be used. The equation is as follows: [33]

$$R \cdot \dot{Q}(t) = \frac{-Q(t)}{S \cdot \epsilon_0} \left(\frac{d_2}{\epsilon_2} + x(t) \right) + \frac{\sigma x(t)}{\epsilon_0}$$

with $x(t) = vt + \frac{1}{2}at^2$

Here, R represents an arbitrary resistor connected to the external circuit, Q(t) is the time-dependent quantity of transferred charge, S is the area of the top electrode, ϵ_0 is the vacuum permittivity, d_2 is the thickness of the dielectric material, ϵ_2 is the relative dielectric constant of the dielectric material, x(t) is the varying distance with time between the top electrode and the dielectric material, σ is the triboelectric charge density induced by the contact electrification, v is the velocity of the top electrode, and a is the acceleration of the top electrode. [33]

In essence, this equation relates the transfer of charge to various parameters such as the dielectric properties, distance variation, charge density, and motion of the components involved in the TENG operation. It helps in

understanding and quantifying the energy generation process in a contact-mode TENG.[33]

Sliding mode

the sliding-mode TENG has two types: dielectric-to-dielectric and conductor-to-dielectric.

Dielectric-to-Dielectric TENG: Both materials in contact are dielectric (insulating) materials, charge separation occurs due to the triboelectric effect when the materials contact and separate, as they separate, opposite charges build up, creating an electric field, this electric field can be used to generate electrical energy in an external circuit. [34]

Conductor-to-Dielectric TENG: One material is a conductor, and the other is a dielectric material, charge transfer also happens due to the triboelectric effect during contact and separation, the key difference is that the conductor allows charges to flow more easily, as a result, there is a flow of current generated in an external circuit, producing electrical energy. [34]

Both types of TENGs utilize relative motion and the triboelectric effect for charge separation, but they differ in the nature of the materials involved and how the generated charges are harnessed for electricity. The choice depends on the specific application and material properties. [34]

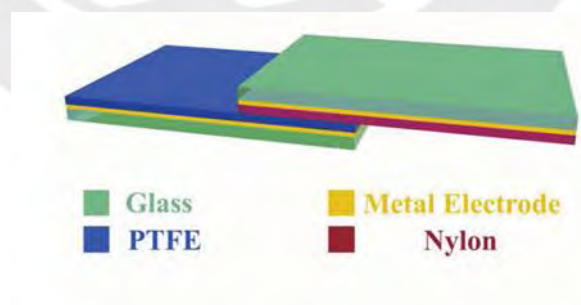


Figure 2 Device structure of the TENG

Freestanding triboelectric layer

FTENGs (Freestanding Triboelectric Nanogenerators) can operate in a non-contact mode without a significant loss in output, greatly boosting energy

conversion efficiency by reducing friction and inelastic collision losses. They fall into two categories:

Contact Mode Stand-Alone Triboelectric Nanogenerators (CFTENG): These use vertical charge separation. They rely on changes in capacitance between the tribocharged surface and two electrodes, with the position of the independent layer crucial to their operation. CFTENGs are excellent for collecting vibration energy without distortion. [35]

Sliding Mode Independent Triboelectric Nanogenerators (SFTENG): These achieve in-plane charge separation and can be classified by their independent layer material. Dielectric SFTENGs maintain consistent capacitance, while metallic SFTENGs show variations with the independent layer's position. SFTENGs tolerate variations in the independent layer's height well, operating effectively without contact. Increasing electrode distance enhances open circuit voltage and height tolerance. Optimal electrode separation increases with the independent layer's height. [35]

This theoretical analysis provides valuable insights into output, structural design, and optimization, guiding the rational design of TENGs to maximize electrical output for energy harvesting and sensitive self-powered sensors. [35]

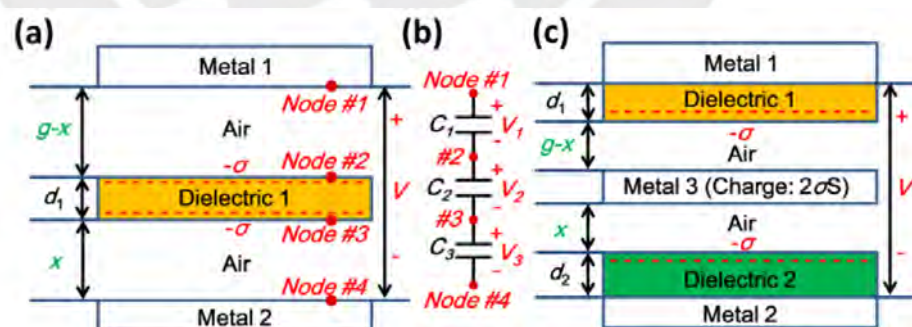


Figure 3 Theoretical models of CFTENGs. (a) model of a typical dielectric freestanding layer CFTENG. (b) equivalent circuit model of the dielectric CFTENG electrostatic system. (c) model of a typical metal freestanding layer CFTENG.

1.1.6 Strategies for increase electrical outputs

The materials used in TENGs construction have not been thoroughly investigated. TENG materials are limited to a few species, and studies have mainly focused on morphological optimization of contact surfaces. However, recent research has explored new material design approaches to enhance TENG electric power output. In 2020, Kim and coworkers make a review [12], in this review discusses four representative TENG component layers and their material requirements. These components are the following:

(a) Charge-generating layer: The charge-generating layer is a fundamental component of triboelectric nanogenerators (TENGs) as it plays a vital role in converting mechanical energy into electrical energy. The performance of TENGs is proportional to the charge density of the contact surface. Therefore, enhancing the charge density of the contact surface is essential to improve TENGs' electric power output.

One approach to increase the contact surface area is to fabricate microscale or nanoscale surface structures. Various methods can be employed for microstructure fabrication, including force-assembled colloidal arrays, soft lithography, anodic aluminum oxide, block-copolymer assembly, and surface nanomaterial fabrication. By increasing the contact area, the number of charges generated by the TENGs can be increased.

Another approach to enhance TENGs' electric power output is surface functionalization. The functionalization process aims to increase the surface charge density or facilitate triboelectric charge transfer. A large difference in surface potentials between two contact surfaces results in a large triboelectric output. Surface modification can be achieved through ion doping, radical injection, plasma treatment, or self-assembled monolayers (SAMs). SAMs with electron-donating and electron-withdrawing functional end groups can effectively change the surface dipoles of the contact layer, significantly enhancing or reducing the triboelectric output.

Modification of the surface property through electrical poling or doping is another approach to improve TENG performance. Changing the intrinsic material properties, such as dielectric constant, polarity, and work function, can be achieved through nanocomposite formation, electrical poling, chemical doping, material synthesis, or lipid layers on the surface of natural substances. For instance, a material with a high dielectric constant can be a good candidate for high-density charge generation. Lipid-based TENGs have a higher positive charge density than other TENGs, but the reason for this is still not fully understood.

Finally, creating new materials through molecular synthesis or nanocomposite formation can lead to improved TENG performance. By engineering materials at the molecular level, it is possible to design materials with specific triboelectric properties that can be tailored to specific applications. Therefore, the development of new materials for TENGs is essential to maximize their potential in various applications

(b) Charge-trapping layer:

Plays an important role in enhancing their performance. One of the challenges with TENGs is the sharp decrease in triboelectric potential due to the combination of opposite charges at the interface between the triboelectric layer and the counter electrode. Charge traps in the charge-trapping layer can prevent this charge combination and improve the overall performance of TENGs.

Charge traps can be formed in polymer insulators through physical or chemical defects. Physical defects include amorphous free volume, crosslinking points, and imperfections in the crystal lattice. Chemical defects include dangling bonds and functional groups in the polymer chains.

Polymers containing aromatic rings in their chains, such as polystyrene (PS) and polyimide (PI), have many trapping sites due to the nonuniform energy chain levels along their main chain. Additionally, the addition of aromatic polymer films between the PVDF layer and the collector electrode can trap

triboelectric charges and increase the triboelectric output by 7-9 times compared to the device without the interlayer.

In summary, the charge-trapping layer is an important component of TENGs that can help prevent the sharp decrease in triboelectric potential and improve overall performance. The use of polymers with aromatic rings and the addition of aromatic polymer films are promising approaches to create charge traps and enhance the performance of TENGs

(c) Charge collecting layer

is an essential component of triboelectric nanogenerators (TENGs) and TENG sensors, which are devices that convert mechanical energy into electrical energy. However, practical applications of deformable TENGs and TENG sensors are currently limited due to the need for reliable deformability in the electrodes. Extensive research has been conducted to find suitable deformable electrodes for these devices.

One promising solution is the use of conductive elastic nanocomposites as alternative electrodes. These composites allow for low-cost printing over a large area and are mechanically stable under repeated mechanical impacts and friction. Elastomer composites made of metal flakes or metal nanosheets have been used to fabricate deformable TENGs. Another option for highly stretchable electrodes is liquid metals. Due to their fluidic nature at room temperature, liquid metals can be injected into a micro-channel fabricated in an elastomer matrix.

In addition to these options, conducting polymers in liquid state are also being explored as a potential electrode material for deformable TENGs. Electrolyte gels, such as hydrogels and ion gels, also allow for high stretchability and high transparency, making them promising candidates for charge-collecting layers. Overall, the development of reliable and effective deformable electrodes is critical for the practical application of TENGs.

a. High Dielectric constant

The pursuit of high-permittivity dielectric materials, driven by the demand for energy sources and advancements in microelectronics, has garnered significant attention.

Materials with colossal permittivity (CP), characterized by permittivity values surpassing 1000, have undergone extensive research. Their permittivity greatly exceeds that of conventional solid dielectrics, holding promise for advancing modern electronics, sensors, energy storage, multifunctional devices, and more.[36]

Traditional ferroelectric oxides attain high permittivity during the paraelectric-ferroelectric transition temperature. Emerging CP materials, such as $\text{CaCu}_3\text{Ti}_4\text{O}_{12}$ (CCTO), exhibit unique dielectric properties and have been extensively studied in the temperature range of 100 to 600 K. While other oxides like complex nickelates, ferrites, and NiO also display CP characteristics, their high dielectric loss hampers their use in capacitive components. Doping has been suggested as a strategy to mitigate loss or enhance permittivity, despite its potential negative impact on other dielectric properties. [36]

To date, various dielectric materials such as polydimethylsiloxane (PDMS), poly(methyl methacrylate) (PMMA), polyimide (PI), polyvinylidene difluoride (PVDF), and polytetrafluoroethylene (PTFE) have been used without modifications, resulting in extremely weak electrical signals. PVDF, known for its good piezoelectric/pyroelectric response and low acoustic impedance, has been extensively studied in mechanical energy harvesting technologies. Following the principle that grafting one polymer onto another polymer structure can combine the benefits of each original polymer, Won Lee in 2017 synthesized PVDF-graft-Poly(tert-butyl acrylate) (PtBA) copolymers through atom transfer radical polymerization (ATRP) as an efficient dielectric to enhance the output performance of triboelectric nanogenerators (TENG).[37]

1.1.7 Materials for TENGs

a. Donor and Acceptors materials

During the material selection process for constructing a TENG, several characteristics are carefully considered to ensure optimal performance. These characteristics include portability, light weight, flexibility, durability, availability, and cost-effectiveness, environmental friendliness, among others[38–40]. However, an important aspect to consider is the material's propensity to acquire a specific charge when subjected to mechanical loading. This charge can either be positive or negative, depending on the material's electron affinity, which categorizes them as electron donor or acceptor materials.

Electron affinity refers to the tendency of a material to either gain or lose electrons. Materials with a high electron affinity have a greater inclination to gain electrons and become negatively charged, thereby acting as electron acceptors[13]. On the other hand, materials with a low electron affinity have a higher likelihood of losing electrons and becoming positively charged, earning them the designation of electron donor materials.

When designing a TENG, the careful selection of suitable electron donor and acceptor materials is critical for efficient charge transfer during the triboelectric process. By pairing materials with contrasting electron affinities, a significant charge imbalance is created at the interface between the two materials upon contact and separation. [33] This charge separation facilitates the generation of electricity within the TENG.

As the research on triboelectric nanogenerators (TENGs) has progressed, different materials with varying electronic affinities have been utilized. Zhang and colleagues, in their comprehensive review on material choices for TENGs, compiled a list of commonly used materials [13]

For electron donors, materials such as aluminum (Al), copper (Cu), skin, nylon, polyethylene terephthalate (PET), silver (Ag), gold (Au), cellulose,

acrylic, polyurethane (PU), polyvinyl alcohol (PVA), Kapton, latex, carbon black/carbon nanotubes (CB/CNT), silk, textile, chi-gly, steel, graphene, and indium tin oxide (ITO) have been commonly employed[13]. Each of these materials possesses unique electrical and mechanical properties, enabling efficient charge transfer during triboelectric interactions.

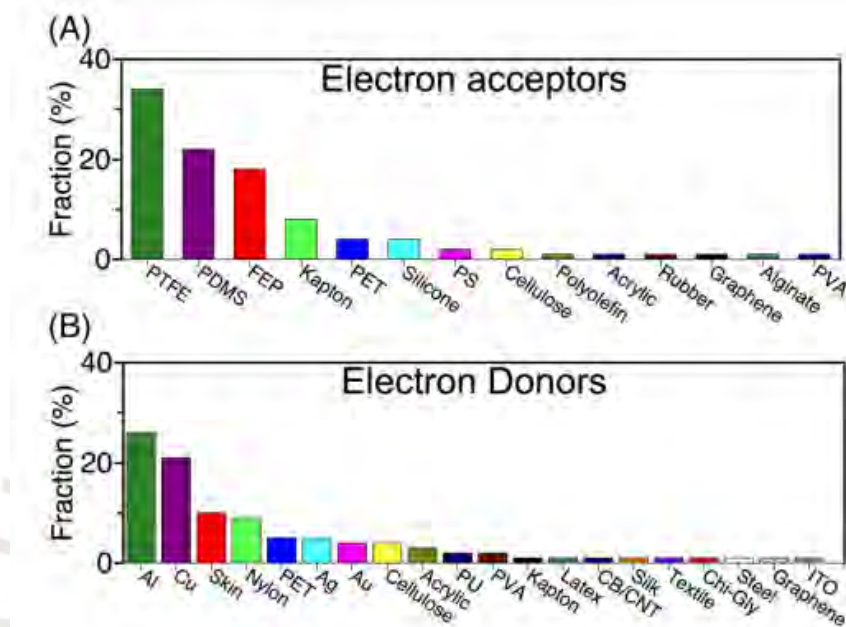


Figure 4 Fraction (%) of the electron acceptor, A, and donor, B, materials used in 100 randomly selected articles from 2012 to 2020.[13]

It is worth noting that ongoing research in the field of TENGs focuses on exploring new materials and their properties to enhance the performance and efficiency of these devices. By understanding the electron affinity of different materials and their impact on charge transfer, researchers can optimize TENG designs for specific applications, leading to advancements in energy harvesting and portable power generation.

b. Triboelectric series

In 1757, Wilcke published a paper in which he described the results of experiments he had conducted on the electrical properties of various materials. He observed that when two different materials were brought

into contact and then separated, one of the materials tended to acquire a positive charge while the other acquired a negative charge. Wilcke's work was the first systematic study of the triboelectric effect, and he created a list of materials arranged in order of their tendency to gain or lose electrons through friction. This list became known as the triboelectric series. [13,41] The triboelectric series is important because it helps us understand how the triboelectric effect works and which materials are likely to generate a charge when they come into contact with each other. The series has been expanded and refined over the years, for examples by the works of Shaw and Henniker[41] and it now includes hundreds of materials.

In certain applications, the presence of static charge can have detrimental effects, leading to various unwanted outcomes such as explosions[42], equipment malfunction[43], fire hazards, and even harm to personnel[44]. To address these concerns, it becomes essential to explore solutions that can minimize static charge accumulation and prevent electrostatic discharge or attraction. In this context, the triboelectric series offers a valuable framework for material selection. By carefully considering the position of materials within the triboelectric series, it becomes possible to identify suitable combinations that can effectively mitigate static charge effects. This approach plays a crucial role in designing and implementing systems that prioritize safety, reliability, and overall performance in industries ranging from electronics and manufacturing to aerospace and hazardous environments.[41,45]

Zou's 2019 article, "Quantifying Triboelectric Series," proposes a standardized method for measuring triboelectric charge density in materials. Traditional methods often suffer from issues like poor contact and surface roughness, leading to inconsistent and unpredictable results. Zou's approach solves these problems by using liquid mercury as the base material for testing, ensuring better contact and reproducibility. This method aligns with the concept of the triboelectric series, which ranks materials based on their electron-gaining or -losing tendencies

when in contact. By employing this standardized method and considering the triboelectric series, researchers can obtain reliable and comparable results, advancing our understanding and application of triboelectric charge phenomena. Additionally, Zou's work introduces a graphic representation of the triboelectric ranking, facilitating the identification of materials with high or low triboelectric properties.[41]

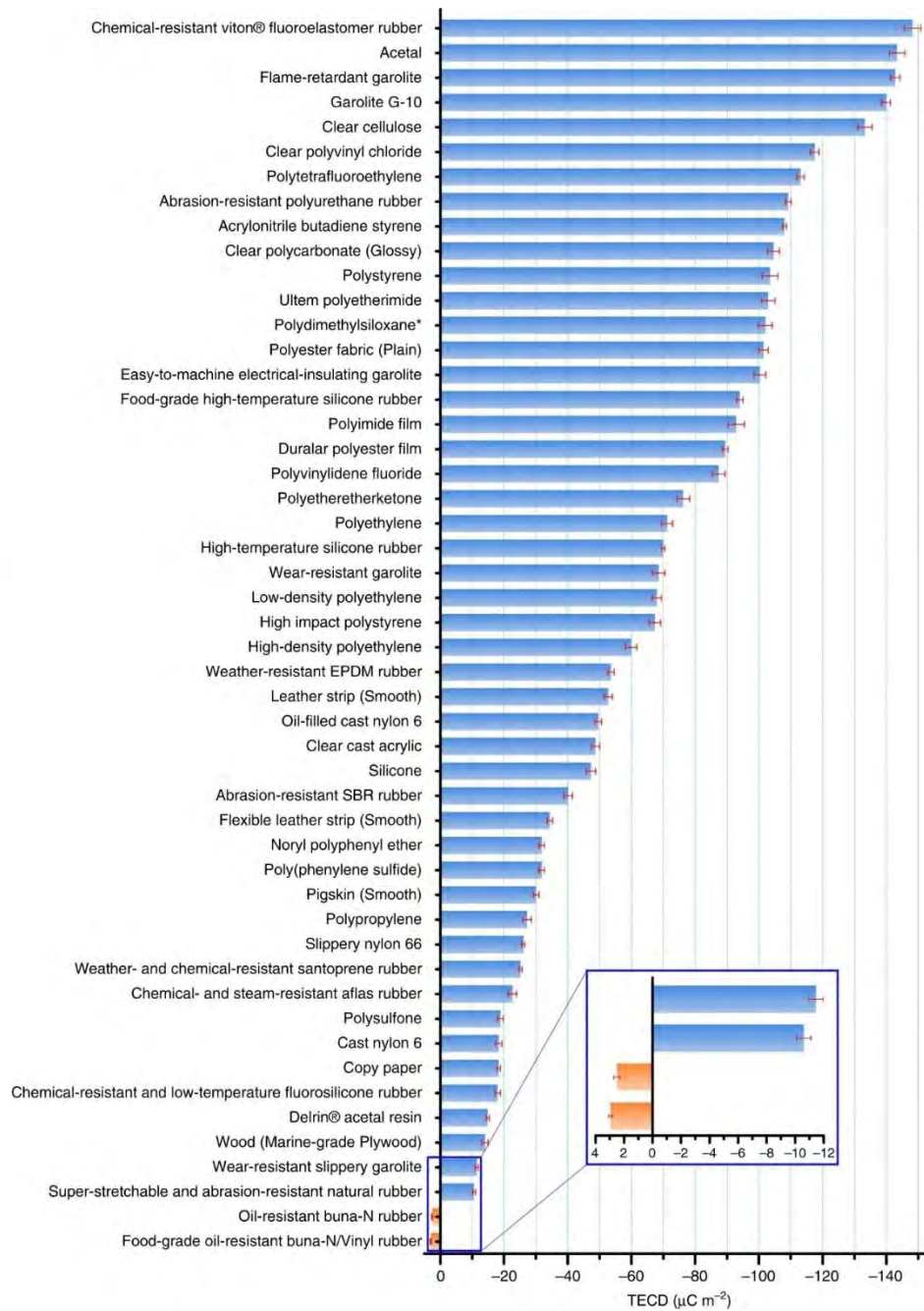


Figure 5 The quantified triboelectric series. The error bar indicates the range within a standard deviation. Source data are provided as a Source Data file [41]

In his 2018 research titled "Triboelectric charge density of porous and deformable fabrics made from polymer fibers," Liu investigates the triboelectric charge density of porous fabrics under the Sliding working mode. This study includes a quantitative triboelectric series, which measures the triboelectric charge density. Liu's method for measuring the charge density involves evaluating the charge generated through the friction between the fabrics and a reference surface. This quantitative approach offers a precise and reproducible way to determine the triboelectric charge density, crucial for understanding and optimizing the performance of porous fabrics in various applications.[46]

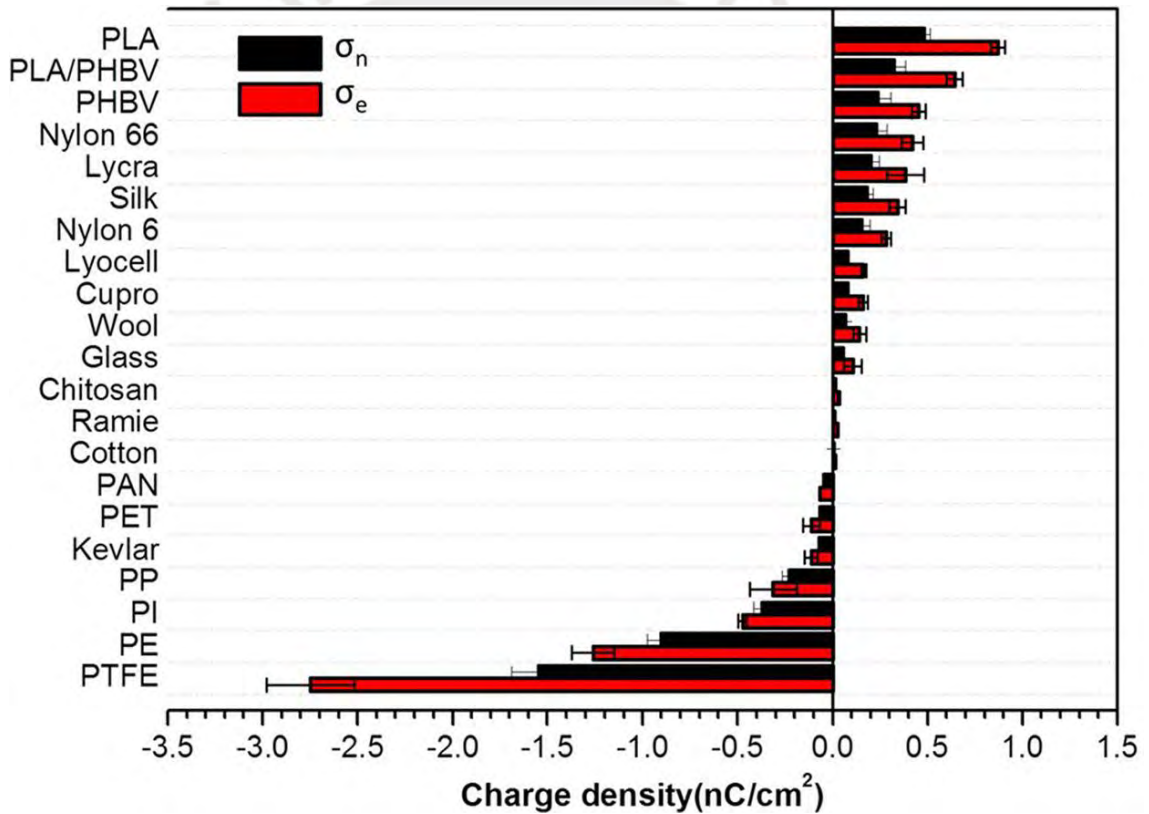


Figure 6 Tribo-electric charge density is compiled with highly porous and deformable knitted fabrics made from twenty-one types of polymer fibers.[46]

Another triboelectric series that was studied by Seol et al. examined the triboelectric properties of various 2D materials. This research aimed to expand our understanding of the electrostatic behavior and interactions

between these materials. Graphene, molybdenum disulfide (MoS_2), and tungsten diselenide (WSe_2) were identified as highly electronegative materials in the triboelectric series, meaning they tend to gain electrons when in contact with other materials. On the other hand, hexagonal boron nitride (h-BN) and borophene exhibited a higher tendency to donate electrons, making them more electropositive in nature. This knowledge of the triboelectric series of 2D materials not only provides valuable insights into their fundamental properties but also paves the way for the development of efficient energy harvesting devices, sensitive sensors, and self-powered technologies. By harnessing the unique characteristics of these materials, researchers can explore new avenues for renewable energy generation, wearable electronics, and environmental monitoring systems.[47]

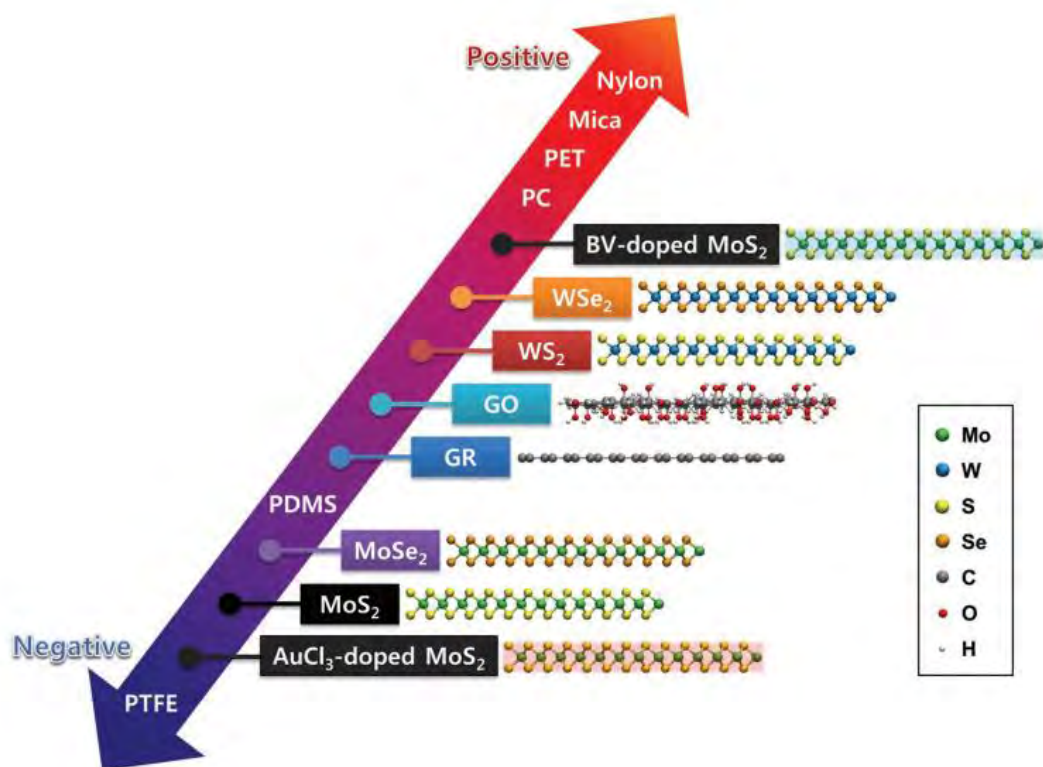


Figure 7 The triboelectric material series of polymeric materials and 2D material. Their chemical structures are shown on their right [47]

1.1.8 Applications

TENGs has demonstrated outstanding capability in direct high voltage/low current power source [48] in applications such as electrospinning for fabricating various polymer nanofibers and electro spray that serves in engineering tissues and drug delivery; also it has been used in [49]molecular mass spectroscopy[50]; micromotor for use in micro/nanoelectromechanical systems[51,52], generation of micro-plasma with potential utilization in wound treatment, dust removal and so on[53]; other fields in which TENGs find uses are in Field electron emitters [54] where its low current working mode is adequate to power them in order to prevent exfoliation of emitter nanowires surfaces [54,55]

1.2 Biopolymers

Biomaterials refer to materials that are either natural or derived from natural sources, and possess the ability to biodegrade and coexist harmoniously with living organisms. In comparison to plastics, biomaterials offer several distinct benefits, such as being eco-friendly, having the capacity to remodel and regenerate, and being able to be utilized in diverse applications, such as energy harvesting, self-powered sensing, and medical therapy.

In recent years, biomaterials have emerged as a promising alternative to traditional materials due to their unique characteristics. For instance, they can be obtained from renewable sources, which are environmentally friendly, and their biodegradable properties make them suitable for the development of sustainable materials. Biomaterials also exhibit excellent mechanical and physicochemical properties, which can be tailored according to specific application requirements. Furthermore, their compatibility with biological systems makes them ideal candidates for the fabrication of biomedical devices such as sensors, implants, and drug delivery systems. Given these advantages, the field of biomaterials is expected to continue growing and making significant contributions to a variety of industries.[4]

1.2.1 Starch

In recent years, there has been an emergence of environmentally-friendly, biodegradable, and low-cost electronic products made from natural materials such as cellulose, lignin, proteins, and starch. Starch has been used as a raw material for the production of biodegradable plastics due to its biodegradable properties, low cost, and abundant availability. [56] Thermoplastic starch (TPS) and polylactic acid (PLA) are the most important biodegradable plastics available in the market, and both use starch as their raw material. [57]

Starch is a natural polysaccharide made up of glucose monomers and can be found in various crops such as rice, wheat, and potatoes. It can be divided into two types: amylose and amylopectin. Amylose has a linear chain structure with good extensibility in solution, while amylopectin has a branched structure with a higher molecular weight. Amylose is made up of α -1,4 linkages while amylopectin has α -1,4 linkages in the backbone and α -1,6 linkages at the branched points.[56,58]

a. Starch extraction

There are different methods that can be used to extraction products made of starch for biomedical applications. These methods include phase separation, electrostatic spinning, fiber meshing, three-dimensional solid fabrication techniques, and injection molding.[58]

Phase separation is a technique where two or more phases are separated from a single solution, resulting in a material with a specific structure. [58]Electrostatic spinning involves the use of an electric field to produce nanofibers from a polymer solution. [59]. Fiber meshing is a method where fibers are arranged in a mesh-like structure to create a scaffold. [60]. Three-dimensional solid fabrication techniques involve the use of computer-aided design (CAD) to create a three-dimensional model, which is then printed layer-by-layer to form the final product.[61] Injection molding involves melting the polymer and injecting it into a mold to create a specific shape. These methods can be used to create different types of starch-based products for biomedical applications. [58]

The phase separation method for manufacturing starch films involves creating a homogeneous mixture of starch, water, and a plasticizer such as glycerol or sorbitol. The mixture is then heated and stirred until the starch is gelatinized. Next, the mixture is cooled to induce phase separation and the formation of two distinct phases: one rich in starch and one rich in water and plasticizer. The starch-rich phase is recovered and placed in a mold to dry and form a film. Adding different plasticizers can adjust the film's properties, such as elasticity and mechanical strength. [56]

In 2011 Torres extracted starch was from tubers, roots, and seeds, and then films were prepared by casting. The dried starch was diluted in distilled water to form a 5% starch solution and partially hydrolyzed in dilute hydrochloric acid (0.1 N) to adjust the pH to 2.0. Glycerol was added at a ratio of 2:5 (glycerol: starch (dry basis)), and the starch solution was homogenized by stirring for 15 minutes at 95°C. Then, the solution was neutralized in dilute sodium hydroxide (0.1 N) to adjust the pH to 10 to stop hydrolysis. Finally, the starch solution (7% w/w) was spread on Petri dishes and placed in an oven at 40°C. After 16 hours of drying, films of about 200 µm in thickness were. [58]

b. Starch properties

Biodegradable: Starch films are biodegradable, which means that they can be broken down by microorganisms and decompose into natural elements such as carbon dioxide, water, and biomass. This property makes starch films an environmentally friendly option for energy storage.[62]

Biocompatible: Starch films are also biocompatible, meaning that they are not toxic and can be used in contact with living tissue without causing harm. This property is important for energy storage applications where the material may come into contact with biological systems.[58]

Renewable: Starch is a renewable resource because it is derived from plants that can be grown and harvested on a continuous basis. This property makes starch films a sustainable option for energy storage compared to non-renewable materials.[56]

Mechanical properties: Starch films have good mechanical properties such as high tensile strength, flexibility, and elasticity. These properties are important for energy

storage applications as they ensure that the material can withstand the stresses and strains associated with energy storage devices.[63]

Thermal stability: Starch films have good thermal stability, which means that they can withstand high temperatures without degrading or losing their properties. This property is important for energy storage applications where the material may be exposed to high temperatures during use.[57,63]

Overall, starch films have several properties that make them suitable for energy storage applications, including their biodegradability, biocompatibility, renewability, mechanical properties, and thermal stability.

c. Starch as a tribolayer and matrix for composite films

The amorphous regions and hydroxyl groups present in starch make it a suitable material for use as a triboelectric positive material in bio-triboelectric nanogenerators (bio-TENGs). These properties contribute to the triboelectric polarity of starch being positive, which can be useful for generating energy in bio-TENGs. By utilizing starch as a tribolayer and matrix for composite films, it is possible to create biodegradable and biocompatible materials that can generate energy through mechanical friction. [4]

In addition to its potential use as a tribolayer, starch has also been investigated as a matrix material for composite films. Composite films are made by combining two or more different materials to create a material with specific properties. Starch can act as a matrix material in these composites, providing a renewable and biodegradable alternative to traditional petroleum-based matrix materials. [64]

1.3 Inorganic fillers

Researchers are highly interested in using inorganic nanomaterials to enhance Triboelectric Nanogenerators (TENGs) for several reasons: a) Unique Charge Distribution: Inorganic nanomaterial-coated surfaces exhibit distinct charge distributions on flat surfaces. b) Enhanced Charge Transfer: Inorganic nanomaterials possess high surface energy, facilitating improved charge transfer between

triboelectric surfaces. c) Dielectric Property Modification: Inorganic nanomaterials can alter the dielectric properties of composites containing them, influencing TENG performance. d) Extra Functionalities: Nanomaterials can introduce additional characteristics to TENGs, making them suitable for specific applications.[65]

This review provides a description of how inorganic nanomaterials, in this case BTO, used in TENGs can lead to further advancements in this field.

1.3.1 BTO

A Description of the filler

BTO serves a specific role within the TENG system, aiming to enhance its triboelectric properties and influence its charge generation and transfer characteristics. Barium titanate is renowned for its unique electrical properties, and its integration into TENGs is recognized for its potential to enhance power generation and overall performance across various applications. [66]

Systematic investigations have been carried out on various electrical properties of BaTiO₃, including temperature-dependent permittivity, dielectric loss, polarization characteristics, and insulation resistivity. These pertinent reports suggest that the electrical properties of BaTiO₃ base materials can be tailored through the introduction of heterogeneous ions or the implementation of diverse sintering methods.[67]

B BTO as a high dielectric constant material and filler for composite films

In a 2019 study conducted by Yan Shao, it was observed that the introduction of BaTiO₃ particles into the BC (Barium Titanate) film led to an increase in surface roughness and dielectric constant. Specifically, when 13.5% BaTiO₃ was incorporated, the resulting TENG system achieved notable improvements. It exhibited an open voltage of 181 V and a short current of 21 μ A. These enhancements represented a significant increase, with the open voltage experiencing a 150% boost and the short current a remarkable

210% enhancement when compared to a setup using a pure BC film in conjunction with PDMS (Polydimethylsiloxane). [66]

The 2020 Liangxia study describes the successful synthesis of BaTiO₃ ceramics co-doped with Mg and Nb at various doping concentrations. The key findings and properties of these co-doped ceramics are summarized below: a) The synthesized ceramics maintain a single perovskite structure. b) The ceramic undergoes a phase transition from tetragonal to pseudocubic BaTiO₃. c) The addition of MgO in concentrations up to 1.0 at% has minimal impact on the microstructure, resulting in ceramics with high density and low internal porosity. [67,68]

In summary, co-doping of BaTiO₃ ceramics with Mg and Nb in specific proportions and concentrations leads to the development of materials with remarkable dielectric properties and temperature stability, making them suitable for various electronic and electrical applications. [67,69]

1.4 Polymer Composites with ceramic fillers for high dielectric constants

Materials with high dielectric constants are in demand for applications like microelectronics' bypass capacitors and energy-storage devices. In general, ceramics, particularly ferroelectric ones, exhibit high dielectric constants but are brittle with low dielectric strength. On the other hand, polymers are flexible, easy to process, and possess high dielectric strength, but they typically have a very low dielectric constant, often less than 10. [70]

Barium titanate (BaTiO₃) is a lead-free ferroelectric ceramic material known for its high dielectric constant. It is commonly used as a filler in polymer-based compounds. Doping modifications of this filler material prove beneficial in enhancing the interfacial interaction and consequently improving the dielectric properties and energy storage capabilities of the composite materials. [71,72]

For instance, in a study by Baiju et al., they prepared compounds using BaTiO₃ doped with cobalt mixed with graphene nanoplatelets. They confirmed that cobalt doping positively influences the enhancement of BaTiO₃'s dielectric constant. Researchers have also found that doping ceramics can promote densification,

improve dielectric temperature stability, and increase the dielectric constant. These effects can be advantageous for enhancing the dielectric and energy storage properties of ceramic-filled composites. [71,72]

Minshu's 2022 study features the development of new polymeric composite dielectric materials aimed at energy storage applications. The findings demonstrate that by examining the dielectric properties of a series of closely related compounds, trends in the characteristics of the filler materials can be deduced. The results align with the anticipated result that the introduction of organic elements and groups with higher polarizability improves the dielectric permittivity of mixed metal phosphonates.[72]

In the context of polymer composites with ceramic fillers for high dielectric constants, carbon-based fillers are preferred materials. These fillers can create percolative systems with exceptionally high dielectric constants. For instance, composites made from multiwalled carbon nanotubes and polyvinylidene fluoride exhibit a dielectric constant (ϵ) of 300 with a low percolation threshold of 1.61% (0.0161 volume fraction). Similarly, graphene-polyvinylidene fluoride composites achieve an ϵ value of 100 at a percolation threshold of 0.61%. Functionalization with polyvinyl alcohol increases ϵ to 225 at a percolation threshold of 2.24%. [73]

However, the challenge lies in the thermal stability of the polymers used in such composites because they are thermoplastic in nature. To address this issue, the study introduces a polyurethane (PU)-based composite with nanoplatelet graphene (NGP) as a high-dielectric-constant material. PU is a thermosetting polymer with excellent mechanical strength, making it suitable for high-temperature applications without losing its material properties. Additionally, composites of carbon nanotubes and PU have previously exhibited electromagnetic wave absorption, indicating their capability to create polarizable composites with NGP fillers. This research explores the properties of this high-dielectric-constant material within the context of polymer composites with ceramic fillers for enhanced dielectric performance. [73]

Chapter 2. Materials and methods

This chapter will offer a comprehensive description of the materials utilized, the methodology employed in synthesizing the Starch/BTO composite films, and the assembly of the Sliding Freestanding Triboelectric Nanogenerator (SF-TENG).

2.1 SF-TENG assembly

The SF-TENG consists of three main components, as depicted in the illustration... (1) Freestanding layer, (2) Stator Layer, and (3) Electrodes. Both the Freestanding layer and the Stator Layer constitute the triboelectric layers of the Nanogenerator.

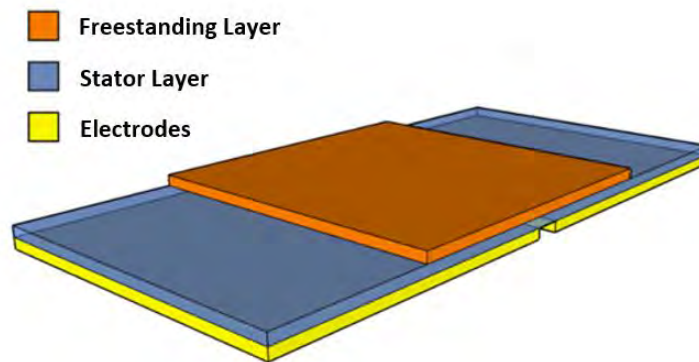


Figure 8 Components of SF-TENG (1) Freestanding Layer, (2) Stator Layer, and (3) Electrodes[54]

For the purposes of this research, the materials employed are defined in Table 1. The Stator is crafted from an adhesive Teflon sheet, while the electrodes are made of copper and secured to a transparent acrylic base using double-sided tape. In the case of the Freestanding layer, experiments were conducted with various materials, including pure Yungay potato starch biopolymer, as well as four composite films comprising a starch matrix with varying concentrations of Barium Titanate (BTO) fillers.

Table 1 : Materials for SF - TENGs

Freestanding Layer	Stator Layer	Electrodes
Starch		
Composite1	Teflon film	
Composite2	(PTFE)	Copper films
Composite3		
Composite4		

To assess the impact of increasing the dielectric constant of one of the triboelectric layers on the electrical outputs, five prototypes were constructed, with dimensions detailed in Table 2. The materials for the Stator, electrodes, foam, and base remained consistent across all five prototypes, with the only variation being in the Freestanding layer. For this layer, five different materials were considered, namely pure Starch film and composite films with a starch polymer matrix reinforced with Barium Titanate nanoparticles (NP-BTO) at concentrations of 0.25%, 0.50%, 0.75%, and 1.00% by weight.

Table 2 : FS-TENG componets size

Component	Material	Size (sqcm)
Freestanding Layer	Starch (Yungay Potato)	
	Starch/NP-BTO (0.25% w/w)	
	Starch/NP-BTO (0.50% w/w)	8x8
	Starch/NP-BTO (0.75% w/w)	
	Starch/NP-BTO (1.00% w/w)	
Stator Layer	Teflon	10x20
Electrodes	Copper	8x8
Foam	Polyurethane	10x15
Base	Copper	8x8

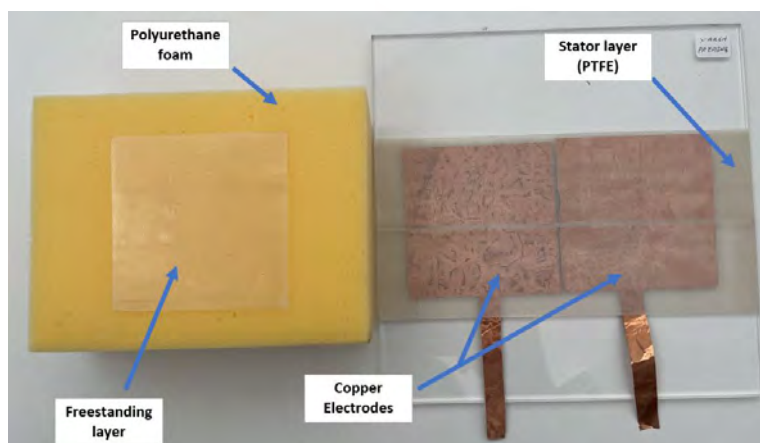


Figure 9 Sliding Freestanding Triboelectric Nanogenerator set up

2.2 Freestanding layer fabrication

Next, a detailed description of the materials and procedures used in the fabrication of the materials for the Freestanding layer will be provided.

2.2.1 Materials

A) Supplies:

1. Yungay Potato Starch 10gr
2. Barium Titanate Oxide (BTO) 0.025gr/0.050gr/0.075gr/0.100gr
3. Distilled Water 200mL
4. Glycerol (Plasticizer) 4gr



Figure 10 Supplies: 1)Yungay Potato Starch, 2) Barium Titanate Oxide (BTO) 3) Distilled Water 200mL
4) Glycerol (Plasticizer) 4gr0

B) Instruments:

1. 01 Electronic analytical balance
2. 01 Laboratory magnetic stirrer (+heater)
3. 01 pH test paper
4. 01 Ultrasonic processor
5. 01 Oven

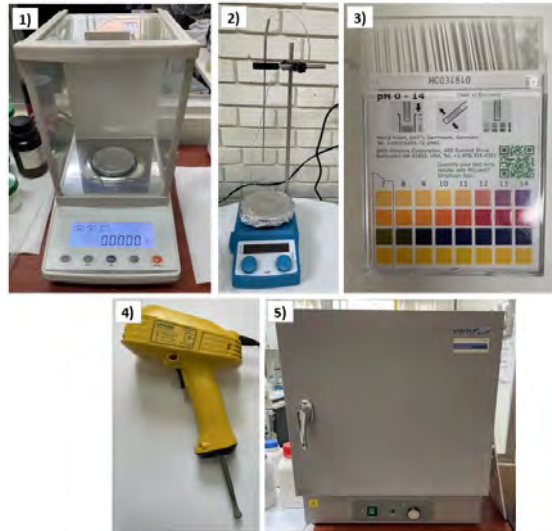


Figure 11 Instruments: 1) Electronic analytical balance 2) Laboratory magnetic stirrer (+heater) 3) pH test paper 4) Ultrasonic processor 5) Oven

C) Utensils:

1. 01 250mL Beaker Glass (for preparing the starch solution)
2. 01 100mL Beaker Glass (for sonicating the BTO nanoparticles)
3. 01 Glass stirring rod
4. Stirrer magnet
5. Petri dishes (15cm diameter)
6. SUS forceps

2.2.2 Procedure

To prepare the starch/BTO composite solution, start by placing 200 ml of distilled water in a 250 ml beaker glass. Next, put the 250 ml beaker glass in the Laboratory magnetic stirrer (with heater) and set the temperature to 95°C, and the stirring speed to 350 RPM (ensuring the appropriate choice of the stirrer magnet). Meanwhile, weigh out 10 grams of Yungay potato starch and gradually add the powder to the stirring distilled water, ensuring no lumps remain in the solution. Proceed by hydrolyzing the solution with hydrochloric acid (0.1N) to achieve a pH of 2.00. In a separate step, weigh 4 grams of glycerol and add it to the solution, stirring continuously for 15 minutes to ensure homogenization. To stop the hydrolysis, neutralize the solution with sodium hydroxide, adjusting the pH to 10. Measure the volume of solution lost due to heating, and then add an equal volume of distilled

water to a 100 ml beaker glass, along with the nanoparticles (according to the aforementioned concentrations). Sonicate the nanoparticles for 15 minutes in intervals of 5 minutes of sonication and 1 minute of equipment resting. Carefully pour the nanoparticle blend into the starch solution, continuing sonication for an additional 15 minutes as per the intervals mentioned earlier. Finally, transfer the resulting composite solution into petri dishes and place the dishes in an oven set at 40°C for a 16-hour drying period. Once dried, the film is obtained inside the petri dish, as illustrated in Figure 12 A. Subsequently, remove the film from the petri dish using tweezers, as shown in Figure 12 B. Lastly, cut it to dimensions of 8x8 cm², as depicted in Figure 12C.

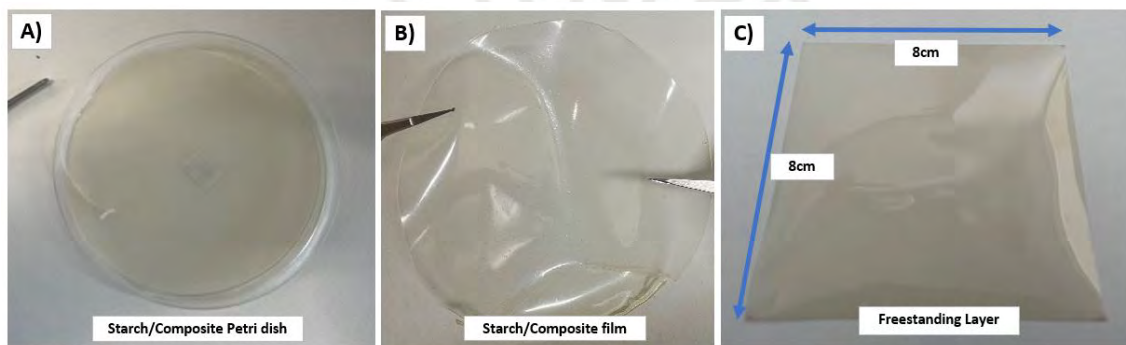


Figure 12 A) Petri dish with the Starch/Composite film, B) Starch/Composite film before cutting, C) Starch/composite size, dimensions of 8x8 cm²

2.3 Materials Characterization

This section will comprehensively detail the characterization of both starch films and composite materials, featuring a starch polymer matrix with BTO nanoparticles as fillers. The focus of this characterization will extend beyond mechanical properties, encompassing structural composition and electrical attributes

2.3.1 Dynamic Light Scattering (DLS) assay

Barium Titanate nanoparticles were procured from the Merck Sigma Aldrich laboratory with a specified size of <100nm. To confirm the size of these nanoparticles, a Dynamic Light Scattering (DLS) test was conducted. In this test, a solution with a predetermined concentration of nanoparticles is prepared to determine their hydrodynamic radius. Generally, it is expected that the hydrodynamic radius of barium titanate particles will be slightly larger.

The DLS test involves exposing the nanoparticle solution to a laser beam, which scatters light off the particles. By analyzing the fluctuations in scattered light, the hydrodynamic radius, or the effective size of the particles in a solution, can be determined. This characterization technique provides valuable insights into the size and distribution of nanoparticles in the solution.

2.3.2 Fourier Transform Infrared (FT-IR) Spectroscopy

To confirm the composition of the starch film and validate its identity, Fourier-Transform Infrared Spectroscopy (FTIR) was utilized. FTIR is a powerful analytical technique that involves measuring the absorption of infrared light by a sample. In this context, FTIR analysis consists of subjecting the starch film to infrared radiation and recording the specific wavelengths of light absorbed by the sample.

By comparing these absorption patterns to a known library of starch spectra, FTIR provides a reliable means of identifying the presence of starch within the film. This analytical method aids in ensuring an accurate assessment of the starch-based material's composition.



Figure 13 Spectrum Two FT-IR Spectrometer

2.3.3 Broad Band Dielectric Spectroscopy (BDS)

As one of the main objectives of this thesis was to validate the hypothesis that increasing the dielectric constant of one of the triboelectric layers enhances electrical outputs, we employed the Alpha-A Analyzer by Novocontrol for the Broadband Dielectric Spectroscopy (BDS) test to measure the dielectric properties of the materials under examination. Our focus in this research primarily centered on

the real dielectric permittivity property, which directly correlates with energy storage through dipole fields within the material. We also explored dielectric loss, associated with the imaginary part of permittivity, to comprehensively understand the material's electrical characteristics.



Figure 14 Novocontrol Alpha-A modular Broadband Dielectric System

2.3 Test Bench

A test bench was constructed to facilitate test replication and standardization, allowing for the comparison of electrical outputs among different FS-TENGs. This one comprises a linear motor array (Newmark Systems, model: CS-500-4, Max speed: 1.5m/sec), a Faraday cage, and an adjustable laboratory platform. The linear motor maintains a constant 1Hz oscillatory motion, while the Faraday cage shields against undesirable noise, particularly in terms of current, given the susceptibility of these small currents to interference from electromagnetic fields. The adjustable labjack sets the contact pressure between triboelectric layers (Figure 15).

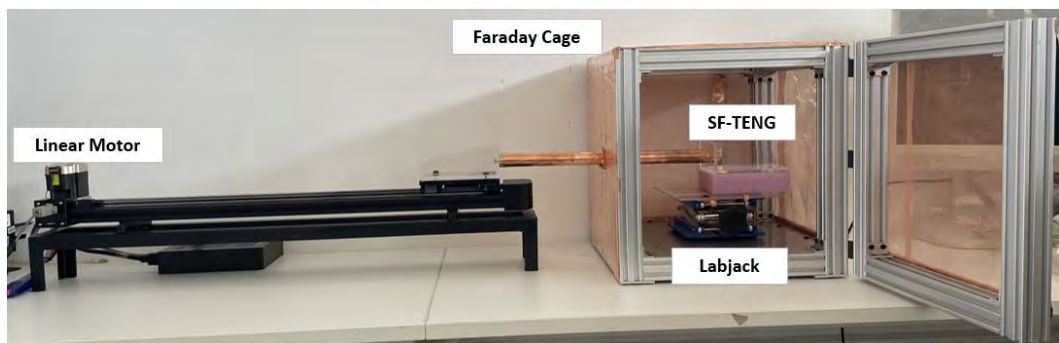
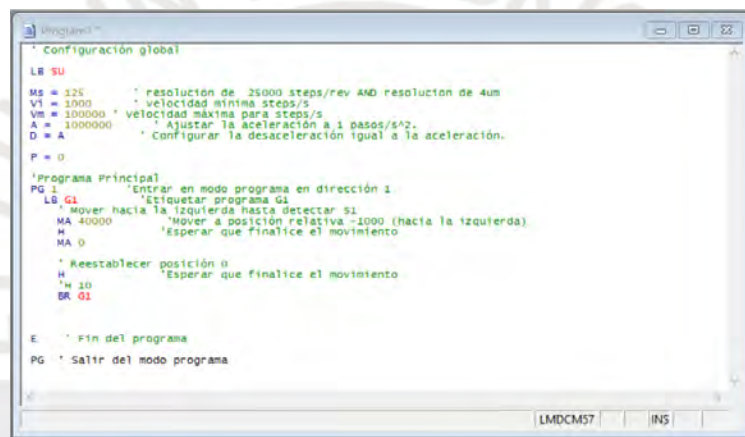


Figure 15 Sliding Freestanding Triboelectric Nanogenerator bench setup

The linear motor was effectively managed through its dedicated driver, utilizing the LMD software in conjunction with the Motion Terminal. The motor's operation was meticulously programmed using the specialized Mcode programming language provided by Schneider Electric, ensuring precise control and synchronization.

To establish seamless communication between the driver and the laptop, a reliable RS-422 communication protocol was employed. This communication link was established through the use of a dedicated USB to RS422 cable, ensuring robust data exchange and real-time monitoring capabilities.

For reference and further analysis, the pertinent control code utilized in this setup is thoughtfully presented below:



```
Program1
* Configuración global
L8 SU
M8 = 325      * resolución de 25000 steps/rev AND resolución de 4um
V1 = 1000    * velocidad mínima steps/s
Vm = 100000  * velocidad máxima para steps/s
A = 1000000  * Ajustar la aceleración a 1 pasos/s^2.
D = A       * Configurar la desaceleración igual a la aceleración.
P = 0
* Programa Principal
PG 1      * Entrar en modo programa en dirección 1
L8 G1    * Etiquetar programa G1
M8 40000 * Mover hacia la izquierda hasta detectar S1
H       * Esperar que finalice el movimiento
M8 0    * Reestablecer posición 0
H 10   * Esperar que finalice el movimiento
BR G1
E      * Fin del programa
PG     * Salir del modo programa
LMDCM57  IN5
```

Figure 16 LMD Software Motion Terminal – Program Code

The Faraday cage was constructed using aluminum framing for its edges, with an impenetrable steel base, while the sides and upper portion were fitted with copper mesh with a 40-mesh count. This equates to 40 holes per square inch, approximately 425 microns in hole size, enabling the filtration of low-frequency radio waves. The 3D design rendering of the entire set up is in the Figure 17 One side of the Faraday cage is hinged to serve as an access point for manipulating the FS-TENG, adjusting pressure with the LabJack, changing the Freestanding layer, and making electrical connections for measurements. On the left side, as depicted in Figure [reference], a shaft passes through one of the faces of the Faraday cage, supporting the FS-TENG's Freestanding layer, which is driven by oscillatory movements at a frequency of 1Hz. This shaft was manufactured from Teflon, considering the stiffness-to-weight ratio, and coated with copper film to prevent radiation penetration. To secure both the

shaft and the TENG to the linear motor, acrylic plates were used, also chosen for their favorable stiffness-to-weight ratio for this application.

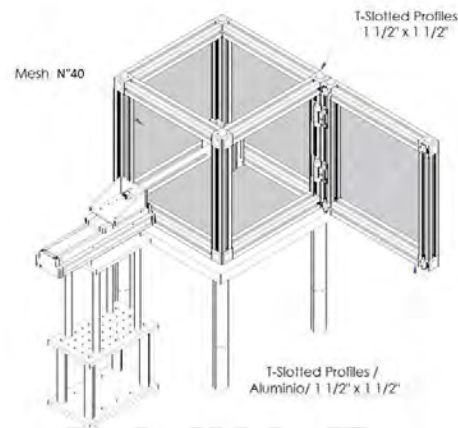


Figure 17 Sliding Freestanding Triboelectric Nanogenerator Bench 3D Drawing

The control of pressure between the triboelectric layers was effectively managed by adjusting the LabJack's height, wherein a greater height setting corresponded to an increase in applied pressure. The inclusion of foam proved to be indispensable in ensuring not only the uniform distribution of pressure across the entire surface of the layers but also in its capacity to absorb any excess force resulting from irregularities present on the layer surfaces.

In the context of this research, it's worth noting that a consistent LabJack height of 8.1cm was maintained for all comparative tests, as visually represented in the accompanying figure 18 This standardization was crucial in facilitating reliable and meaningful comparisons among various experimental setups and configurations.

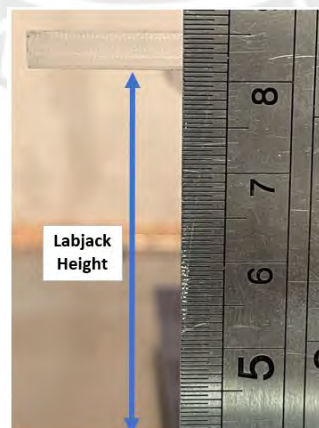


Figure 18 Labjack Height of 8.1 centimeters

The final test setup, as illustrated in the figure, demands strict adherence to the requirement that the Faraday cage door must remain closed throughout the entire testing process. This precaution is essential to ensure the integrity of the test environment.

In order to facilitate accurate and meaningful comparisons between the various triboelectric layers being tested, a standardized test duration of 20 minutes has been established for the purpose of charging them. This standardized duration is critical for maintaining consistency in the testing methodology and results analysis.

Furthermore, it is worth noting that individual FSTENG setups have been designated for each specific material under examination. This decision was influenced by the findings of preliminary tests, which revealed wear and tear on the triboelectric layer of the stator (Teflon) when shared among materials. Implementing separate setups for each material not only ensures the reliability of the testing conditions but also enhances the overall experimental accuracy and reliability.

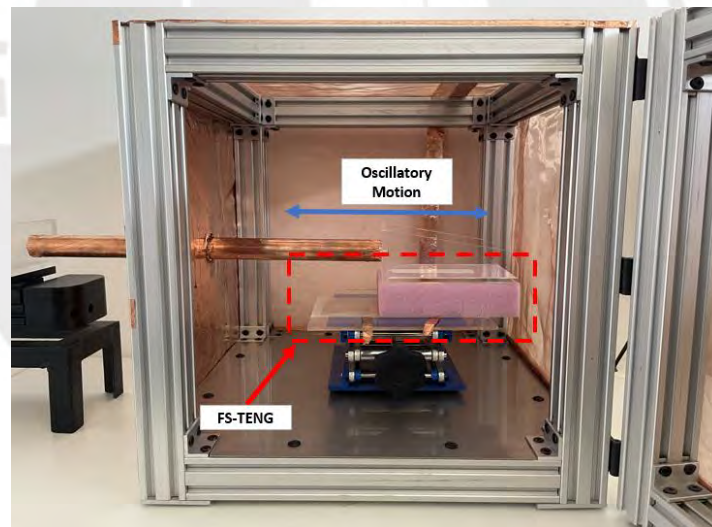


Figure 19 Sliding freestanding Triboelectric Nanogenerator with the oscillatory motion

2.4 Electrical Tests

Electrical devices are subject to characterization based on various electrical properties, including open-circuit voltage, short-circuit current, power output, and the identification of optimal operating resistances, among others. This section focuses primarily on the comprehensive assessment of two key parameters: open-circuit voltage and short-circuit current.

Furthermore, the study delves into the performance of these devices by subjecting them to a series of load tests involving capacitors with varying capacitances. The experiments utilize FSTENGs (Sliding Freestanding Triboelectric Nanogenerators) to execute the tests, providing the opportunity for meticulous evaluation and meaningful comparisons of the resultant data. This approach yields valuable insights into the behavior and efficiency of these innovative devices.

2.4.1 Open Circuit Voltage (Voc)

Open-circuit voltage provides information about the electrical potential that the device can generate or maintain when it is not connected to a load. This is essential for understanding the level of energy that the device can supply under ideal conditions.

To measure the open-circuit voltage, a Tektronix DPO2022 oscilloscope with a X10 attenuation probe was used. Each part of the probe was connected to each electrode, following the schematic below:

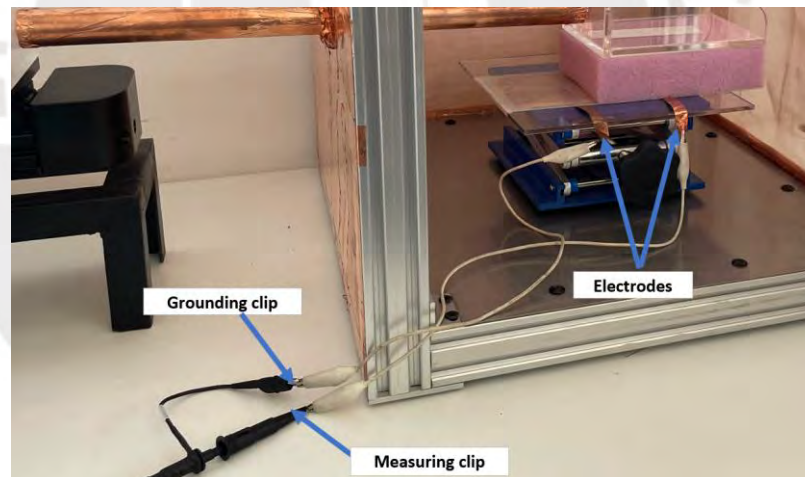


Figure 20 Open Circuit Voltage Measurements Setup

Certainly, measuring rectified signals holds significant importance in various applications. These rectified signals serve as the primary source of energy for charging components like capacitors or triggering the operation of light-emitting diodes (LEDs). By quantifying and analyzing these signals, engineers and researchers gain valuable insights into the efficiency, voltage levels, and behavior of rectification processes, which are fundamental in a

wide range of electrical and electronic systems. This knowledge, in turn, contributes to the optimization and enhancement of such systems, ensuring reliable and efficient performance.

To measure the rectified voltage, a configuration with a diode bridge rectifier (FBR) was used as follows:

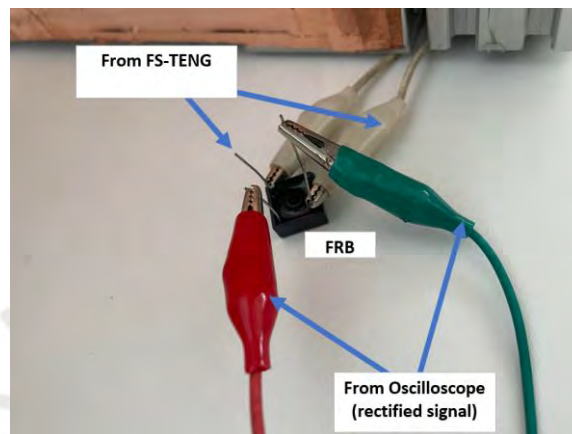


Figure 21 Open Circuit Voltage Measurement Setup with Full Bridge Rectifier

2.4.2 Short Circuit Current (I_{sc})

Closely mirroring the measurements of open-circuit voltage, the characterization of the FSTENG device also entails the crucial measurement of short-circuit currents. In this scenario, a low-noise preamplifier from Stanford Research Systems served to measure the current signal. The input of the signal was directly connected to the FS-TENG, and the output was linked to the oscilloscope. By configuring the sensitivity to $1\mu\text{A}/\text{V}$, accurate measurements of short-circuit current signals were achieved. It's worth noting that the connections for measuring the rectified short-circuit current closely resembled the schematic shown in the previous section.

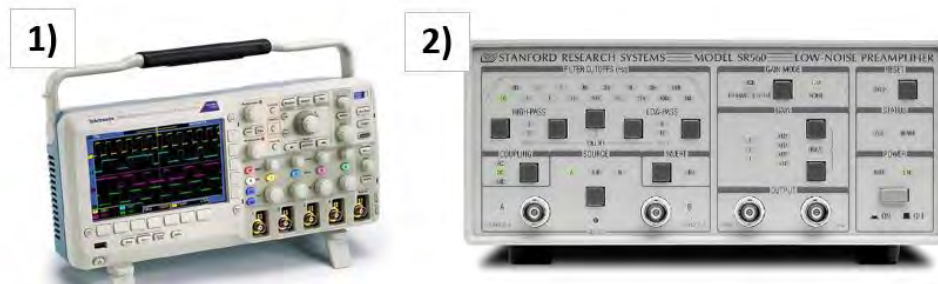


Figure 22 1) Oscilloscope DPO 2022, 2) Low-Noise Preamplifier Model SR560 Stanford Research Systems

2.4.3 Capacitor Charging and powering LEDs

In order to substantiate the feasibility of deploying FSTENG prototypes in power generation applications, tests were conducted to charge capacitors with varying capacitances. Furthermore, their efficacy in illuminating an LED was also assessed. These evaluations not only provide empirical evidence of the devices' performance but also underscore their potential utility in scenarios demanding energy conversion and utilization. The experimental results serve as a testament to the practicality and versatility of FSTENGs within the realm of energization applications.

To charge the capacitors, the configuration depicted in Figure 23 was employed.

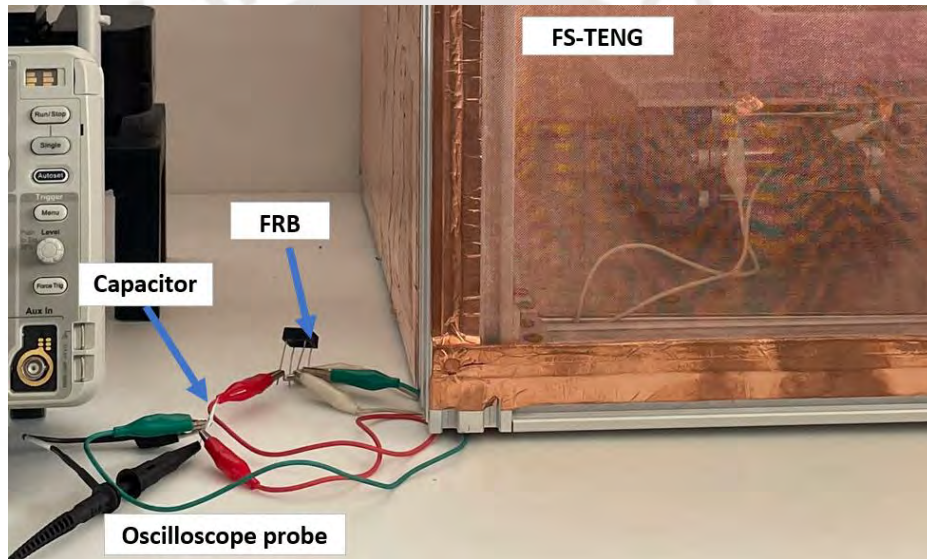


Figure 23 Capacitor charging and voltage measurement setup.

The same applies to powering the LEDs, where a diode bridge rectifier was employed, serving as a bridge between the TENG and the LED.

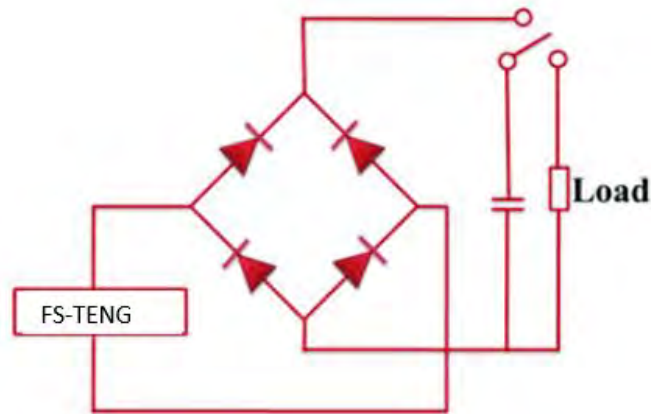


Figure 24 Sliding Freestanding Triboelectric Nanogenerator Circuit for Capacitor Charging

In addition to conducting tests on the test bench to ensure experiment repeatability, we also performed tests involving manually initiated random movements. These manual movements introduced higher frequencies and exerted greater pressure than those experienced on the test bench. The anticipation was that these conditions would yield even more significant electrical outputs compared to those generated during testing on the bench.

Chapter 3 Result and Discussion

3.1 Dynamic Light Scattering Test results

Dynamic Light Scattering (DLS) is a technique for accurately measuring the size of nanoparticles (NPs) in a colloidal suspension. It analyses the motion of NPs and calculates their hydrodynamic diameter using the Stokes-Einstein equation. By measuring fluctuations in scattered laser light, DLS generates data on NP size and size distribution. Figure 25 shows a dynamic light scattering (DLS) particle size measurement of the Barium Titanate Nanoparticles Dispersion. The peak of the DLS particle size measurement is at 114nm.

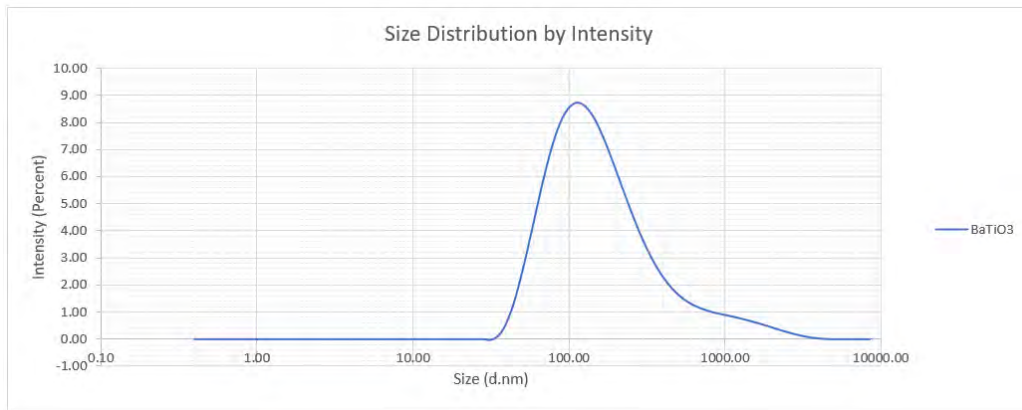


Figure 25 BaTiO3 Nanoparticles Hydrodynamic Diameter distribution

It's worth noting that the manufacturer's specification states that the particles are smaller than 100 nm. The discrepancy between the DLS measurement and the manufacturer's specification arises because the DLS measurement represents hydrodynamic radii, which tend to be larger than the actual particle radii due to the effects of solvation and particle interactions.

3.2 Fourier Transform-Infrared Spectroscopy results

Barium Titanate Nanoparticles (BTO-NP)

The FTIR spectrum of barium titanate particles were collected in transmittance mode and is displayed in Figure [insert figure number]. Upon analysing the graph, distinct vibrational peaks are observed at positions of 502 cm^{-1} , 510 cm^{-1} , 858 cm^{-1} , 1422 cm^{-1} , and 1749 cm^{-1} . These peaks correspond to stretching modes in Ti-O (both normal and bending modes), Ti-OH, COO-[74], Ba-OH[75].

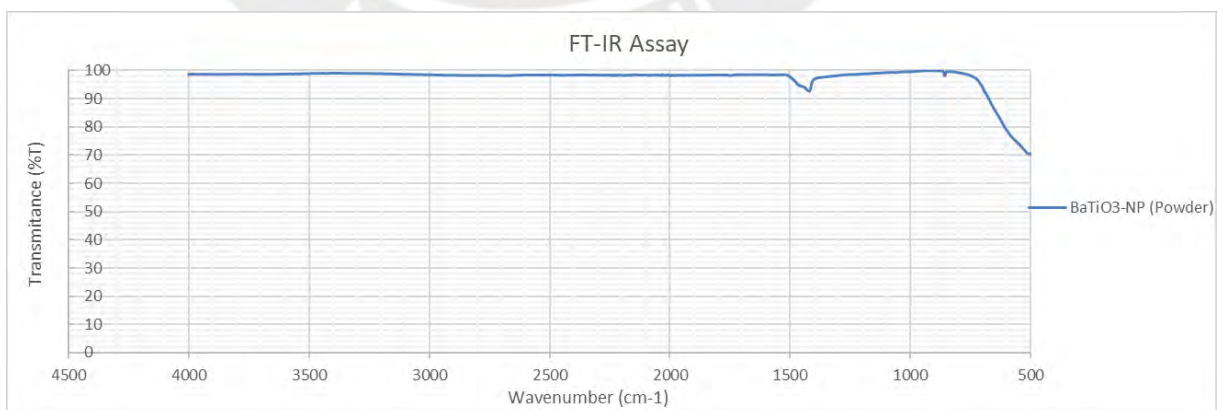


Figure 26 BaTiO3 Nano-particles FT- IR Complete Spectrum

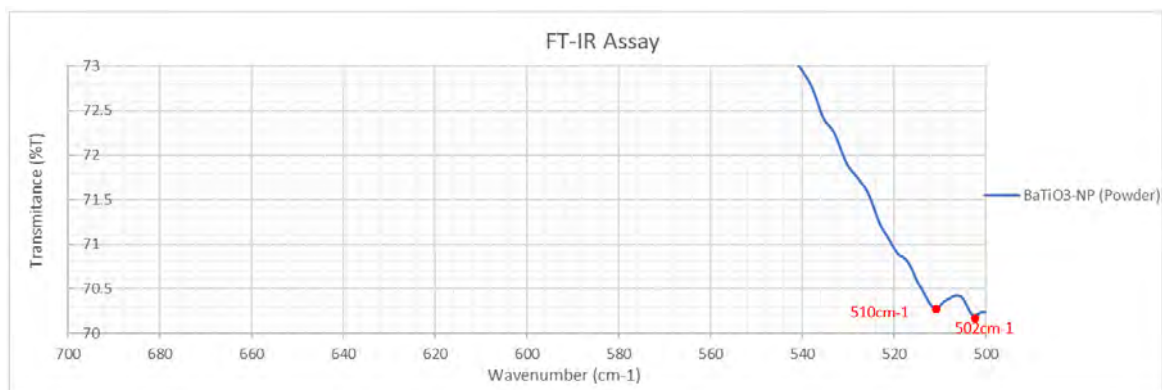


Figure 27 BaTiO₃ Nano-particles FT- IR, Peaks on 502 cm⁻¹, 510 cm⁻¹ correspond stretching modes in Ti-O (both normal and bending modes), respectively.

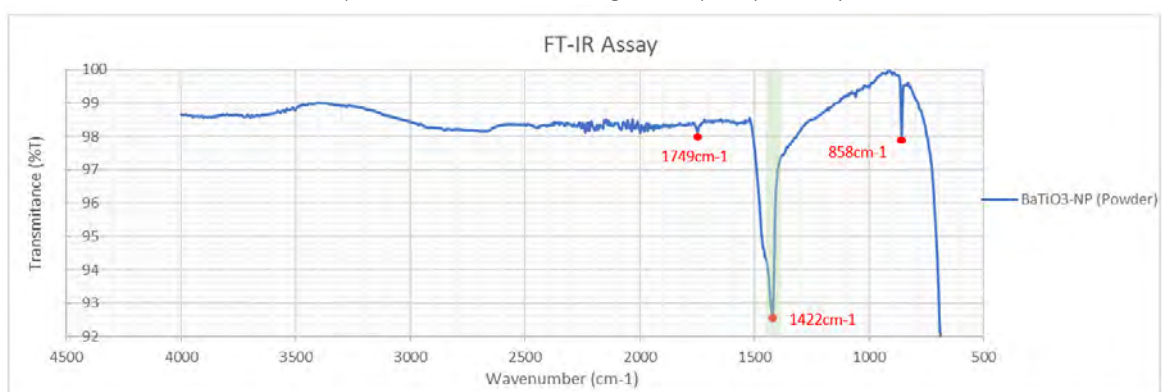


Figure 28 BaTiO₃ Nano-particles FT- IR, Peaks on 858 cm⁻¹, 1422 cm⁻¹, and 1749 cm⁻¹ correspond Ti-OH, COO⁻, Ba-OH, respectively.

Starch film and Starch/BTO composites

The FTIR spectra of Starch/Composite films containing varying concentrations of NP-BTO exhibited similar spectral shapes but differing intensities, as depicted in Figure 34. This observation suggests that the presence of BTO fillers primarily impacts the long-range ordering and crystalline structure of the films.

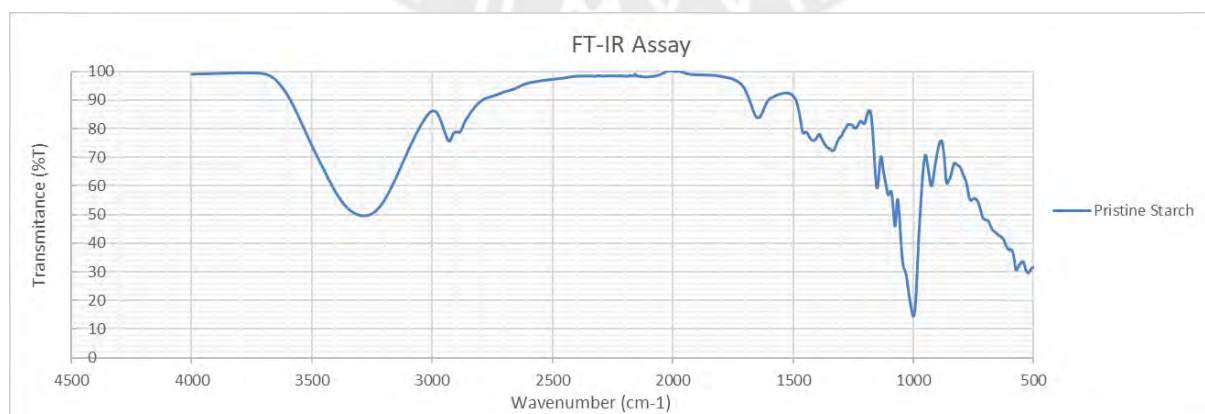


Figure 29 Pristine Starch FT- IR Spectrum

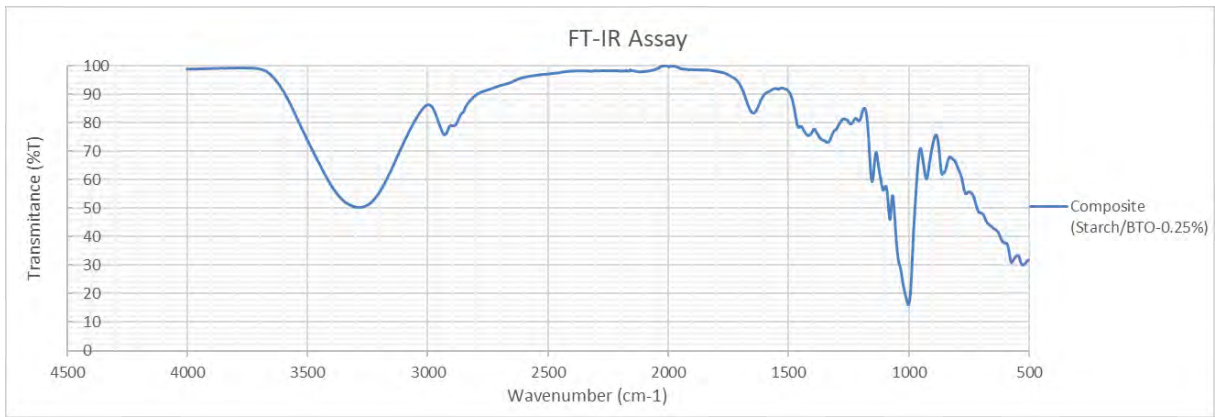


Figure 30 Starch/NP-BTO 0.25% w/w Composite FT- IR Spectrum

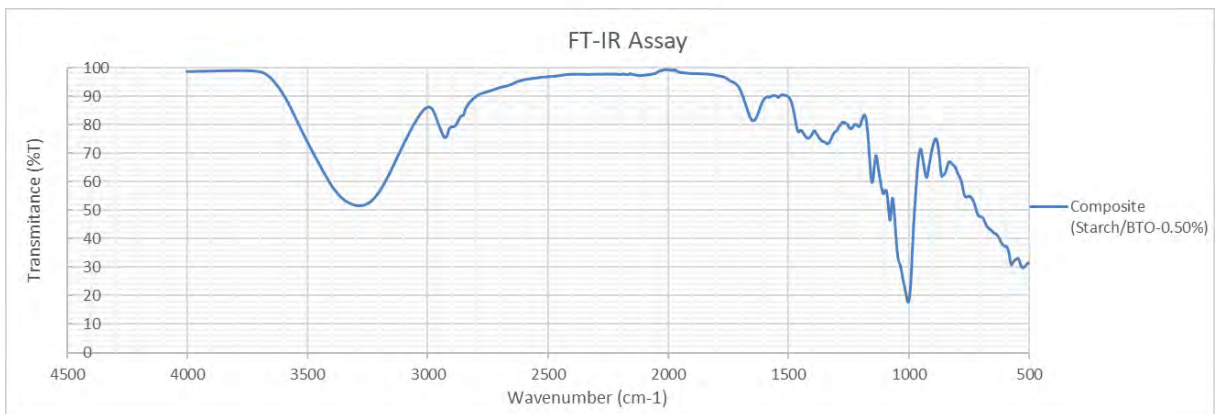


Figure 31 Starch/NP-BTO 0.50% w/w Composite FT- IR Spectrum

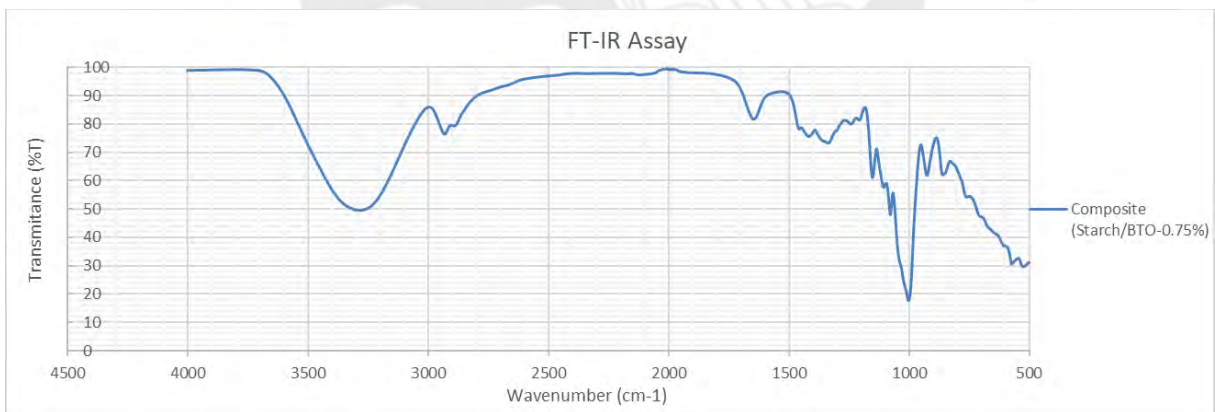


Figure 32 Starch/NP-BTO 0.75% w/w Composite FT- IR Spectrum

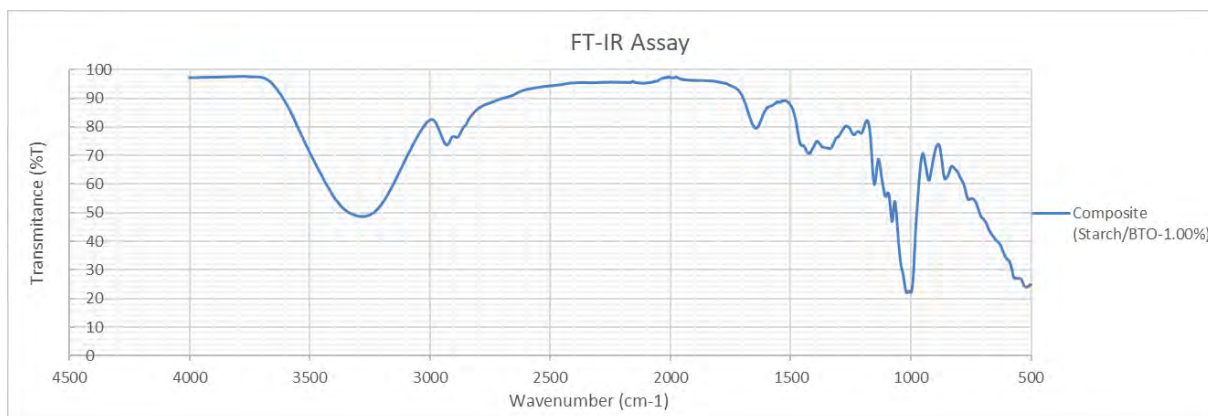


Figure 33 Starch/NP-BTO 1.00% w/w Composite FT- IR Spectrum

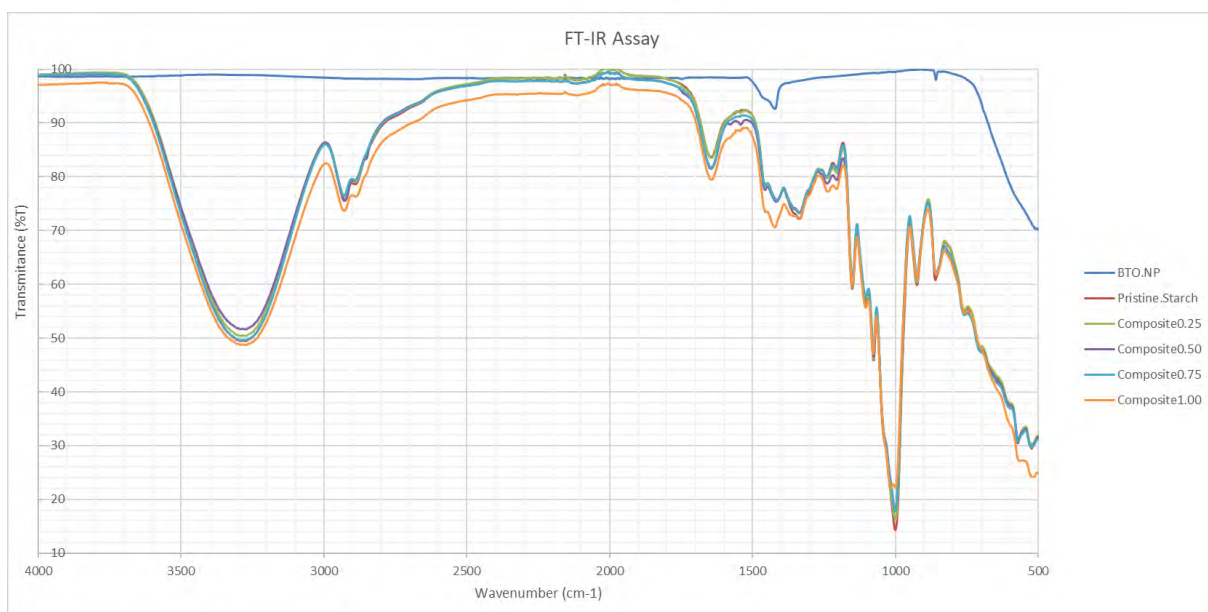


Figure 34 Starch/Composites FT – IR Spectra

3.3 Broadband Dielectric Spectroscopy results

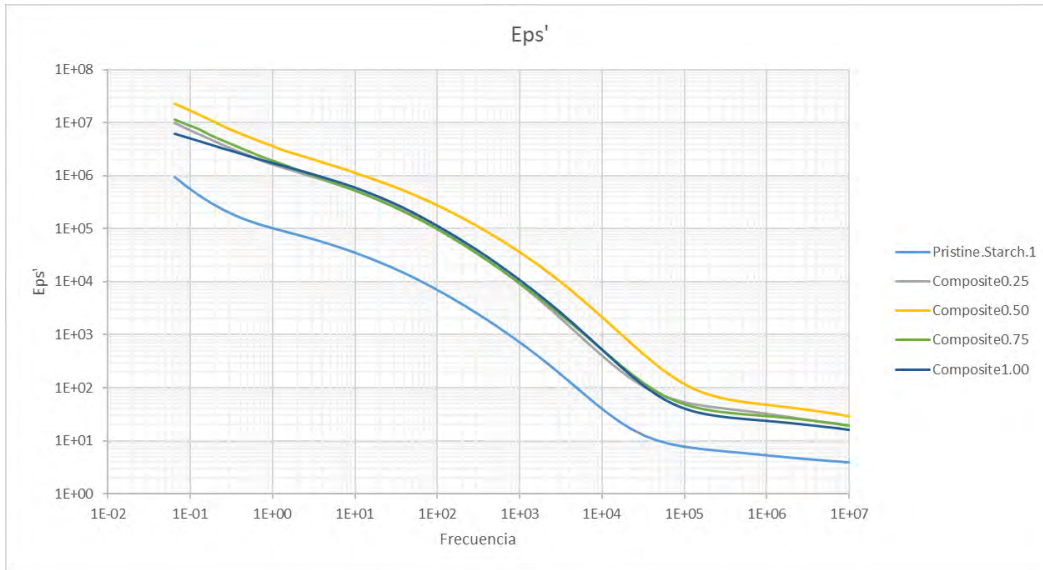


Figure 35 The real part of the Dielectric Permittivity for Starch/Composite Samples

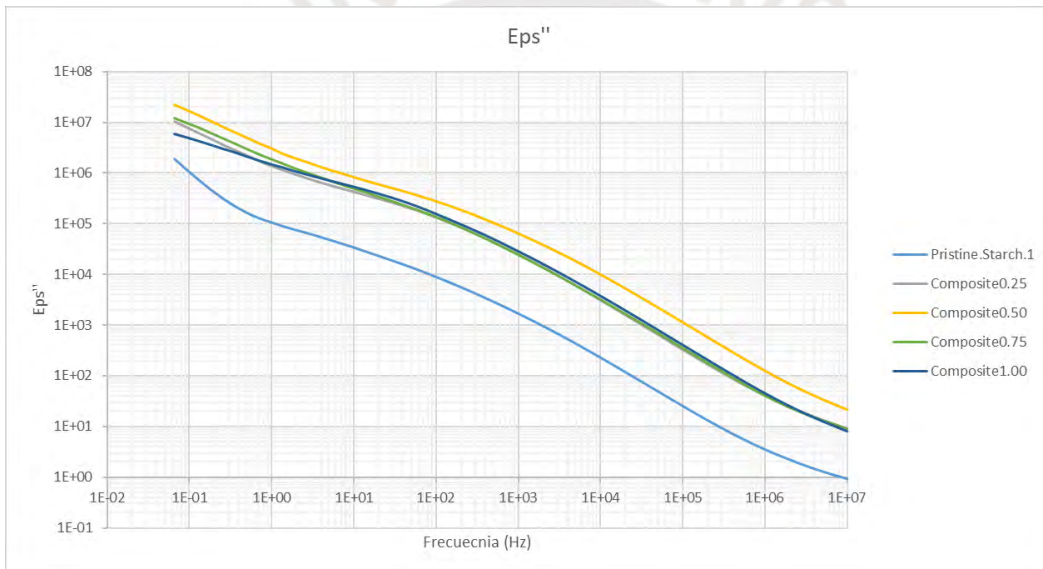


Figure 36 The real part of the Dielectric Permittivity for Starch/Composite Samples

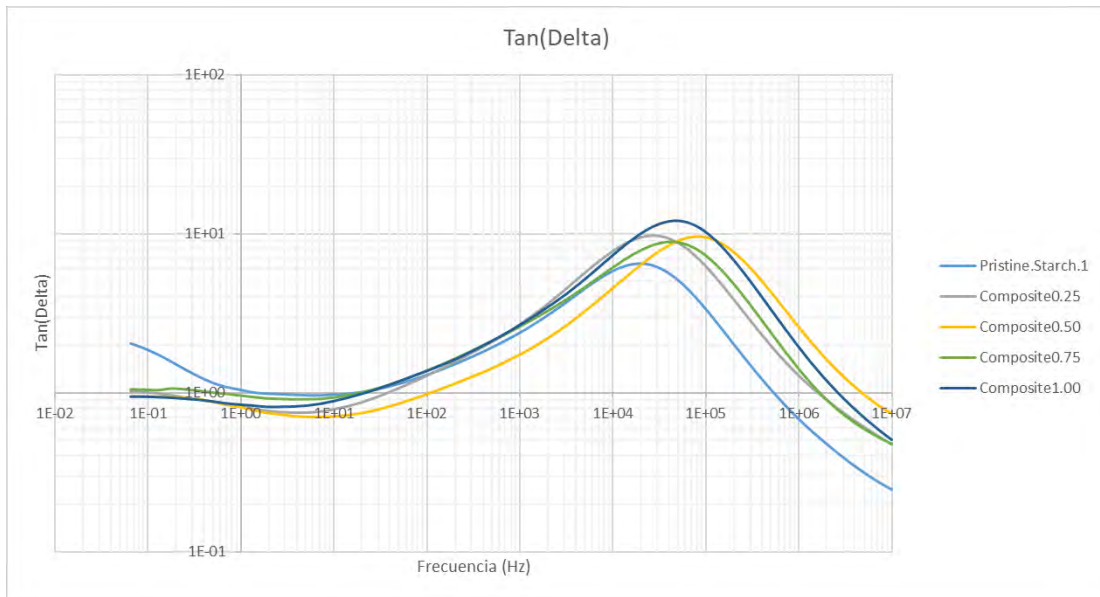


Figure 37 Dielectric Loss of the Starch/Composite Samples

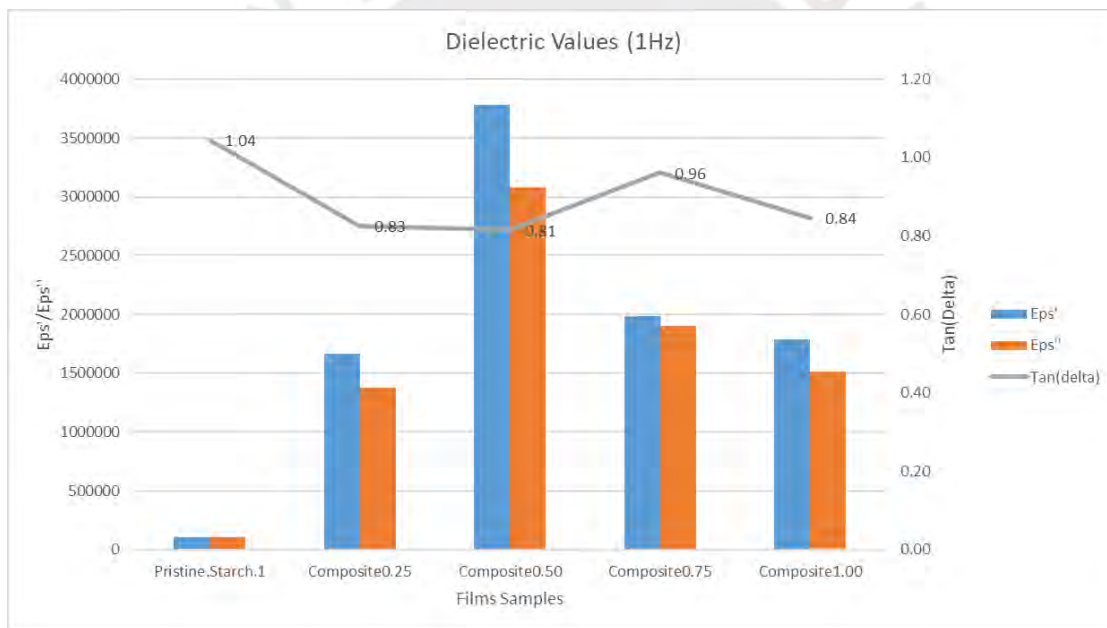


Figure 38 Dielectric properties of Starch/Composite samples

Table 3 : Dielectric properties for Starch/composite samples

	Frecuency: 1Hz				
	Pristine.Starch.1	Composite0.25	Composite0.50	Composite0.75	Composite1.00
Eps'	102,884	1,665,730	3,777,800	1,981,440	1,788,710
Eps''	107,512	1,375,230	3,078,580	1,904,160	1,511,210
Tan(delta)	1.04	0.83	0.81	0.96	0.84

3.4 Electrical Outputs Results

3.4.1 Open Circuit Voltage

FS-TENG Pristine Starch Freestanding Layer

The voltage graph reveals a distinct alternating pattern, aligning with our expectations, given its origin from oscillatory motions—a clear indicator of correlated behavior. Additionally, each cycle exhibits an approximate one-second period, showcasing peak values that span from 14.3 V to -17.1 V.

Upon subjecting the signal to rectification, the initial anticipation was to yield exclusively positive values. Surprisingly, in this instance, the negative segment of the waveform becomes mirrored above the X-axis. Notably, the maximum amplitude now registers at 18.1 V. When we compare this with the prior graph, it becomes evident that the voltage has experienced a 1 V increase. This intriguing phenomenon can be attributed to the gradual accumulation of charge on the FS-TENG over time. The interval between data points allowed for the voltage to escalate, thanks to the mounting charge density.

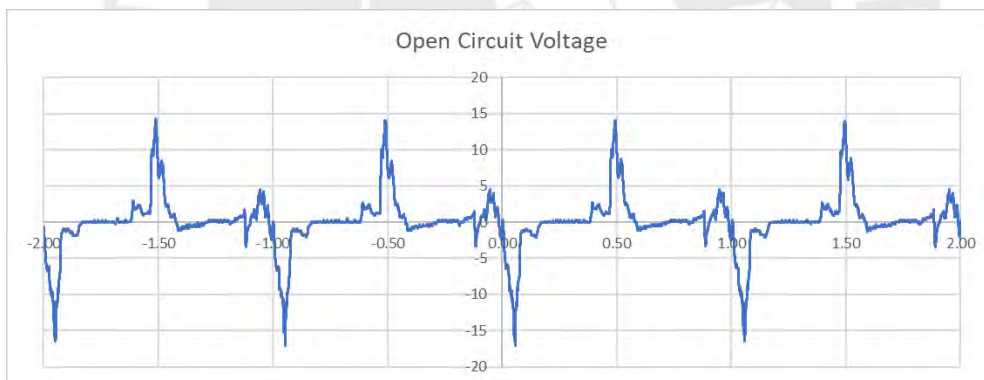


Figure 39 Open circuit voltage for FS-TENG Pristine Starch (f=1Hz)

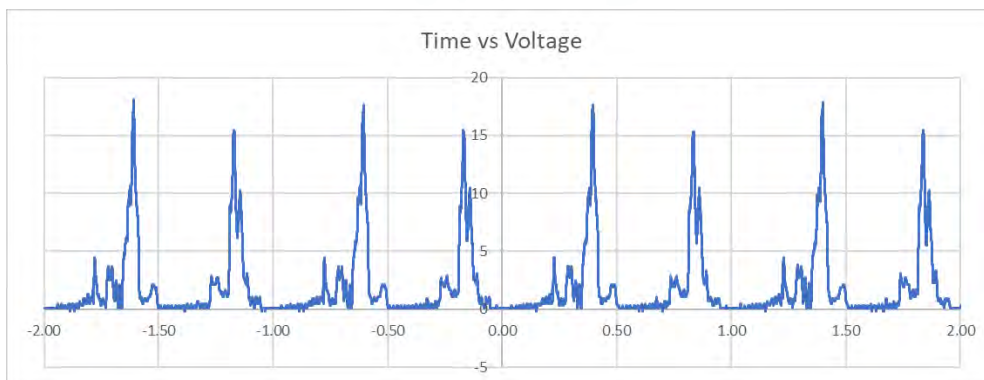


Figure 40 Rectified Open circuit voltage for FS-TENG Pristine Starch (f=1Hz)

In this initial scenario, it is readily apparent that the dominant frequency component of the signal is 1 Hz. This observation was further corroborated by subjecting the signal to a Fast Fourier Transform (FFT) analysis using MATLAB software, which precisely identified a frequency of 1.067 Hz.

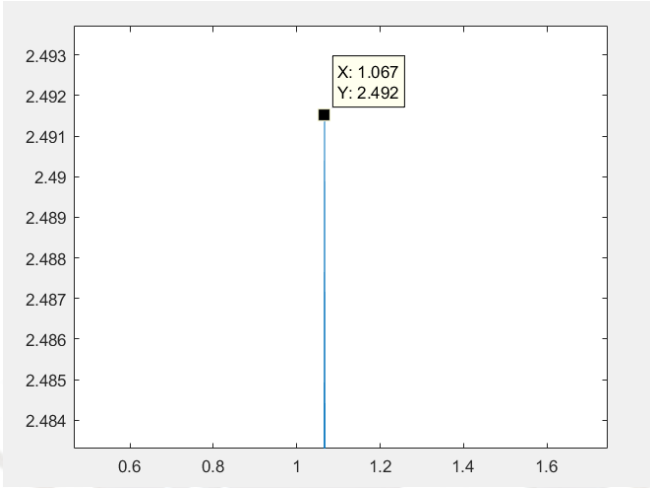


Figure 41 Fast Fourier Transform of Pristine Starch Open circuit voltage Signal

Moreover, it is noteworthy that the signal exhibits additional frequency components aside from the prominent 1 Hz frequency. These additional frequencies are indicative of inherent noise within the physical system. The sources contributing to this noise are multifaceted, encompassing a spectrum of potential factors such as electromagnetic interference and inherent limitations within the measurement equipment.

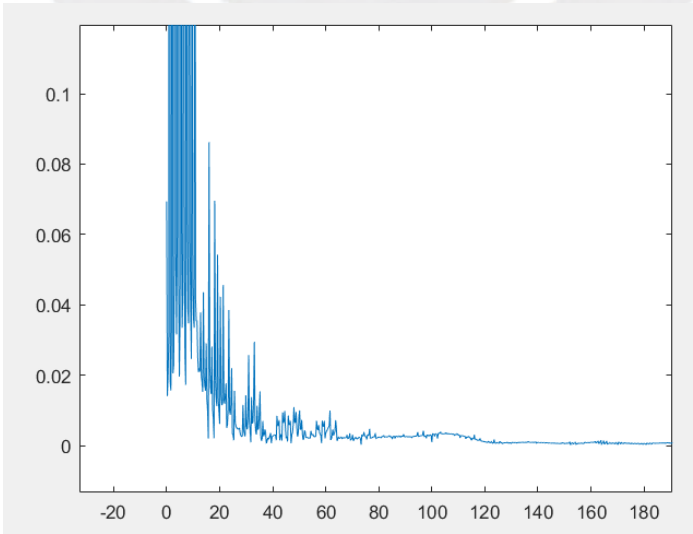


Figure 42 Fast Fourier Transform of Pristine Starch Open circuit voltage Signal

Nonetheless, the salient point to emphasize is that despite the presence of these extraneous frequencies, the core waveform of the signal remains distinctly discernible. Given this clarity, there is no imperative need to employ signal filtering techniques in our subsequent analytical endeavors.

The experimental setup extended to manual oscillatory movements, yielding noteworthy observations. In these graphs, we discern significantly elevated voltages, with peaks reaching as low as -251.00 volts. Notably, when employing a diode rectifier bridge, voltage peaks of up to 452 volts were achieved. This remarkable variation in voltage can be attributed to the absence of precise pressure regulation over the Sliding Freestanding Triboelectric Nanogenerator (SF-TENG).

Upon conducting an in-depth analysis, it becomes evident that variations in the applied pressure exerted on the SF-TENG play a pivotal role in voltage generation. A direct correlation emerges, indicating that higher applied pressure leads to a substantial augmentation of voltage output. Furthermore, the profound influence of oscillation frequency on voltage is manifest. An increase in the oscillation frequency further amplifies the observed voltage levels.

In summary, the manual oscillation experiments not only underscore the sensitivity of the SF-TENG to pressure control but also highlight the immense potential for voltage enhancement through both meticulous pressure manipulation and strategic frequency modulation.

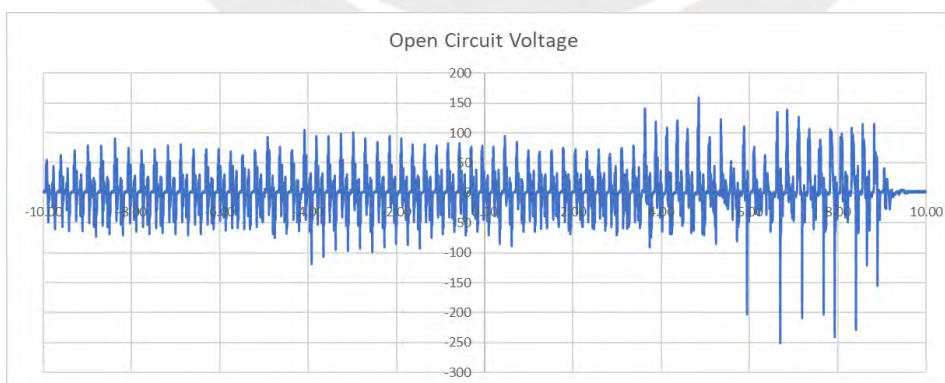


Figure 43 Open circuit voltage for FS-TENG Pristine Starch (Random Movements)

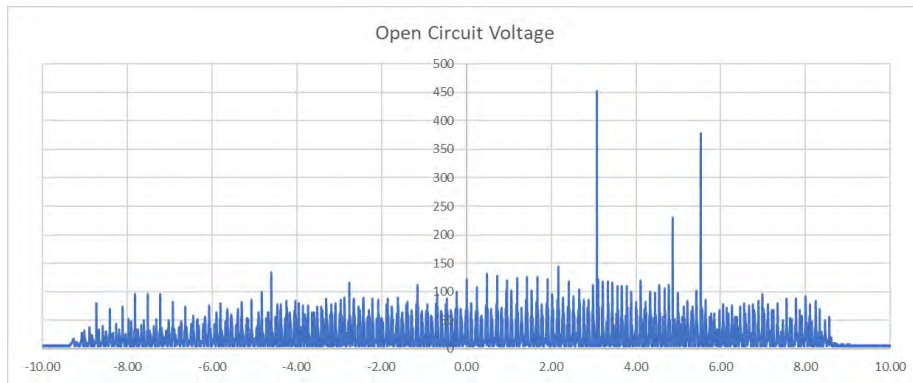


Figure 44 Rectified Open circuit voltage for FS-TENG Pristine Starch (Random Movements)

SF-TENG Starch/NP-BTO 0.25% w/w Composite

Considering the substantial increase in the dielectric constant achieved by incorporating Barium Titanate (BTO) into the starch-based material, one would naturally anticipate a corresponding rise in the output voltages. However, the empirical results reveal an intriguing departure from this expectation. Instead of an upward trend, we observe a slight decrease in peak voltages, with values fluctuating within the range of 13.7 volts to -15.1 volts.

This unexpected outcome is not limited to the BTO inclusion alone. Even when employing a Full Bridge Rectifier (FBR), the voltage levels only experience a marginal increase, peaking at 15.3 volts. Such consistent behavior across these different material configurations suggests the presence of an uncontrolled variable that may be exerting an influence on the anticipated voltage enhancement.

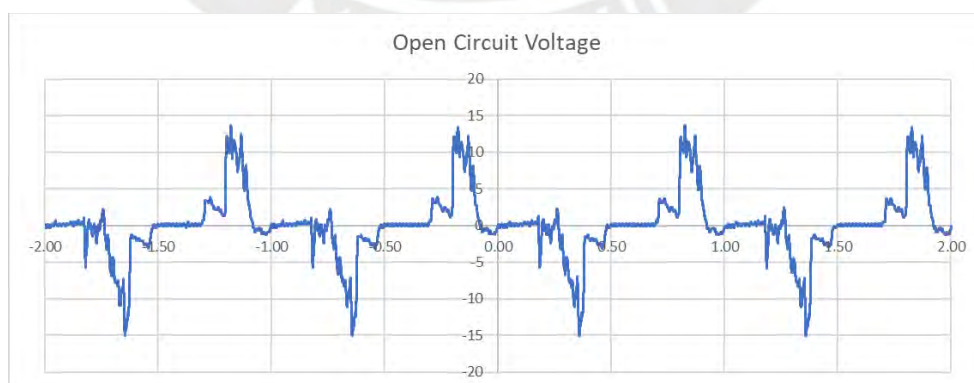


Figure 45 Open circuit voltage for SF-TENG Starch/NP-BTO 0.25% w/w Composite (f=1Hz)

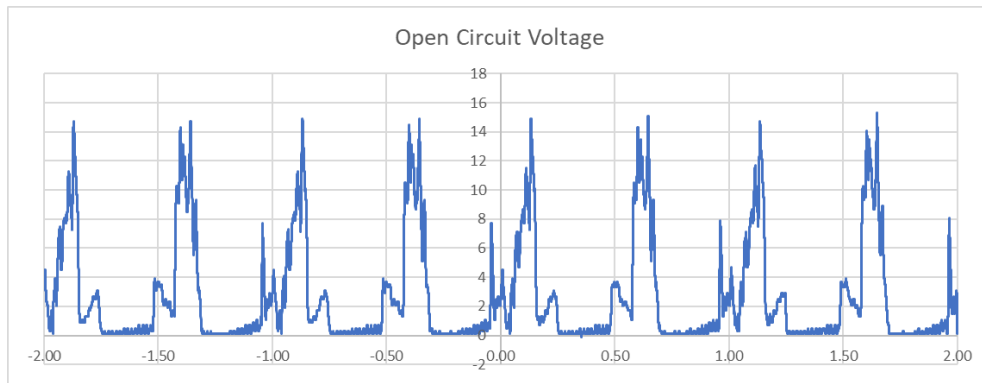


Figure 46 Rectified Open circuit voltage for SF-TENG Starch/NP-BTO 0.25% w/w Composite ($f=1\text{Hz}$)

Despite the observed reduction in the previous trial, this phenomenon doesn't carry over when subjected to manual movements. Here, the influence of manually applied pressure and higher frequencies takes precedence in driving voltage increments. Remarkably, under these conditions, voltage levels surged to as high as 253 volts, and with the application of a Full Bridge Rectifier (FBR), values reached an impressive 407 volts. These results unmistakably demonstrate the presence of more dominant factors contributing to the voltage surge.

These findings highlight that in the context of manual movements, factors such as pressure variations and increased oscillation frequencies have a more substantial impact on voltage generation than the dielectric constant alone. Understanding these influential variables is crucial for optimizing and harnessing the full potential of voltage enhancement in the system.

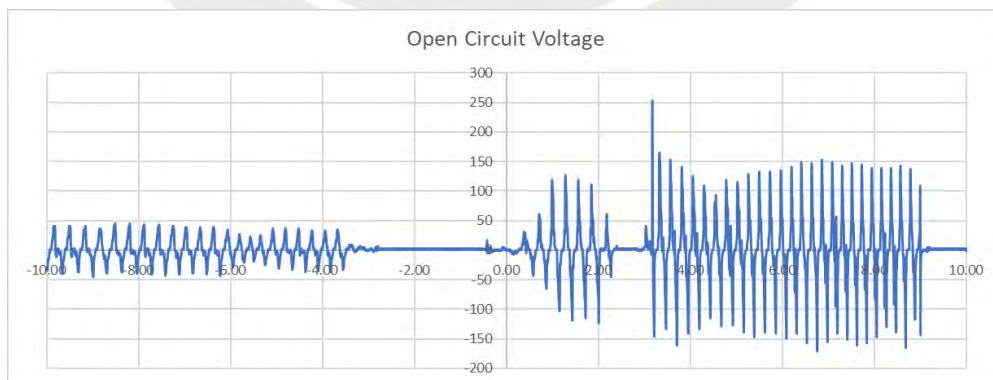


Figure 47 Open circuit voltage for SF-TENG Starch/NP-BTO 0.25% w/w Composite (Random Movements)

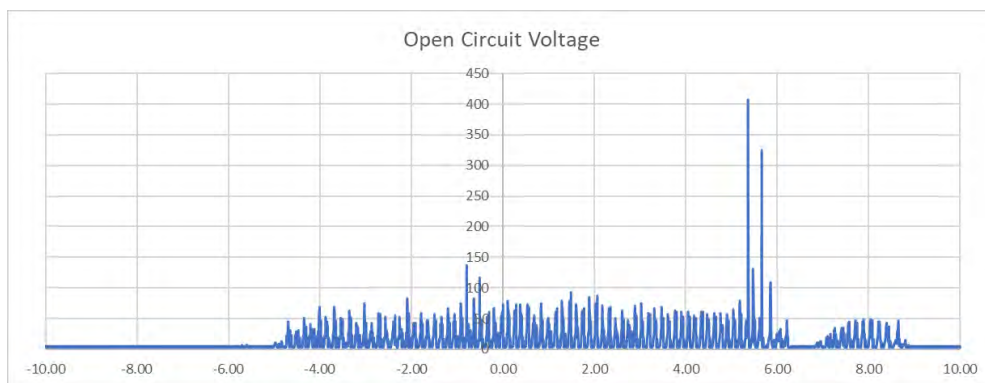


Figure 48 Rectified Open circuit voltage for SF-TENG Starch/NP-BTO 0.25% w/w Composite (Random Movements)

SF-TENG Starch/NP-BTO 0.50% w/w Composite

Despite the 0.5% BTO sample exhibiting the highest dielectric constant, it is surprising to note that it shows the lowest voltage value, dropping below 10 volts both in the presence and absence of a Full Bridge Rectifier (FRB). During the fabrication process of this film, a significant issue was observed: the emergence of cracks within its structure. As a result, it became necessary to assemble the film incrementally, piece by piece, in order to eventually form the complete film. This approach led to irregularities on the material's surface, resulting in a highly uneven texture compared to other homogeneous films.

This surface irregularity may partially account for the unusually low voltage values observed during testing. However, it is intriguing to note that, despite following the same manufacturing procedure as other films, some of them experienced this issue only to a minor extent and managed to maintain the integrity of their structures, achieving a more uniform surface. The mystery surrounding the formation of cracks in the 0.5% BTO film raises important questions about additional factors that may have influenced the outcome and warrants further investigation.

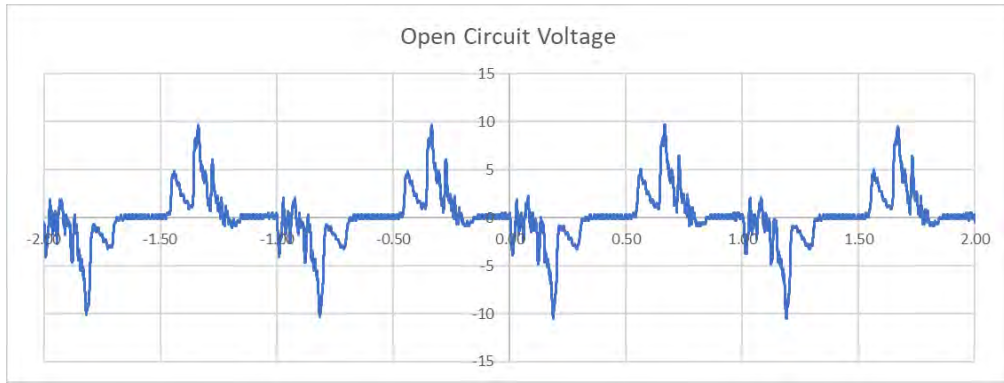


Figure 49 Open circuit voltage for SF-TENG Starch/NP-BTO 0.50% w/w Composite (f=1Hz)

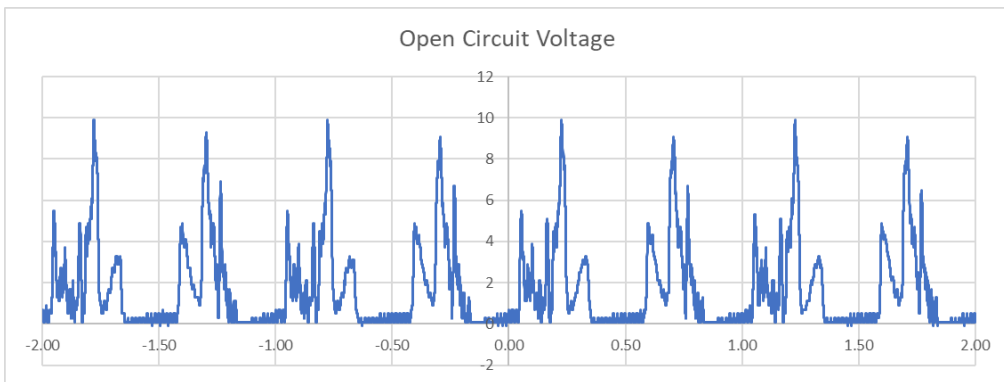


Figure 50 Rectified Open circuit voltage for SF-TENG Starch/NP-BTO 0.50% w/w Composite (f=1Hz)

Despite the noticeable decline in voltages observed when subjected to random motion testing, it is noteworthy that the difference compared to other TENGs appears to decrease significantly. During these tests, voltage peaks of up to 248V have been identified, which is a remarkable phenomenon.

Additionally, when employing a Full Bridge Rectifier (FBR), even higher voltage peaks have been recorded, reaching up to 310V.

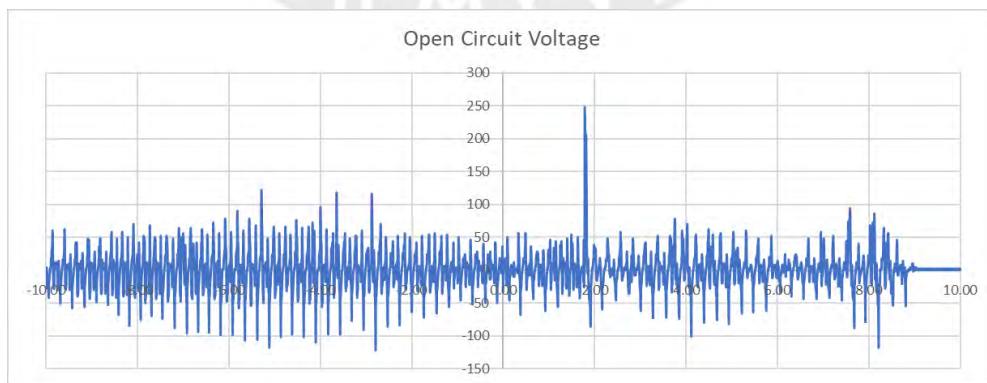


Figure 51 Open circuit voltage for SF-TENG Starch/NP-BTO 0.50% w/w Composite (Random Movements)

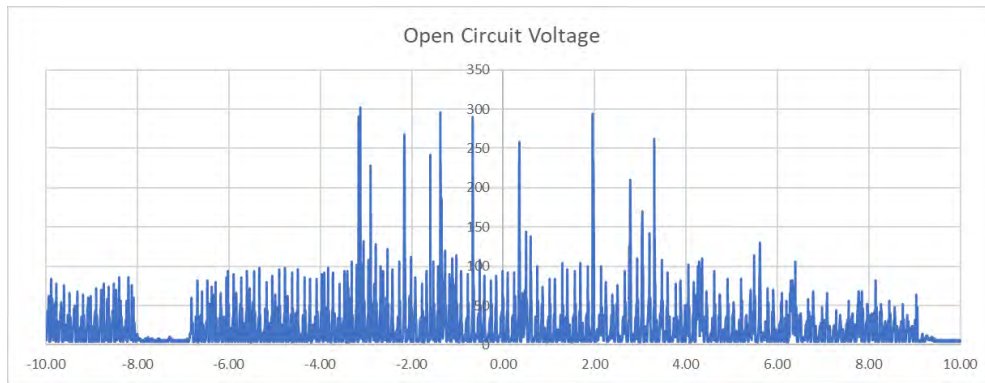


Figure 52 Rectified Open circuit voltage for SF-TENG Starch/NP-BTO 0.50% w/w Composite (Random Movements)

SF-TENG Starch/NP-BTO 0.75% w/w Composite

In this particular case, we can clearly observe the growth trend taking place. This trend is substantiated by the results of the BDS test, which unequivocally show an increase in the dielectric constant when compared to pure starch. Additionally, there is a noticeable rise in voltage levels, which fluctuate within the range of -21.9 to 23.1 volts. However, it's worth noting that the increase in voltage is not in direct proportion to the change in the dielectric constant.

Remarkably, in this scenario, the dielectric constant has increased its value by a substantial factor of 14 compared to the pristine starch sample. However, intriguingly, this significant increase in the dielectric constant is translated into a relatively modest voltage increment of just 4 volts when compared to the baseline starch sample.

These results underscore the complexity of the relationship between dielectric properties and voltage generation in our experimental setup. While a substantial enhancement in the dielectric constant is achieved, the translation of this improvement into voltage output appears to be influenced by various other factors, which necessitate further investigation and analysis to gain a comprehensive understanding of the underlying mechanisms at play

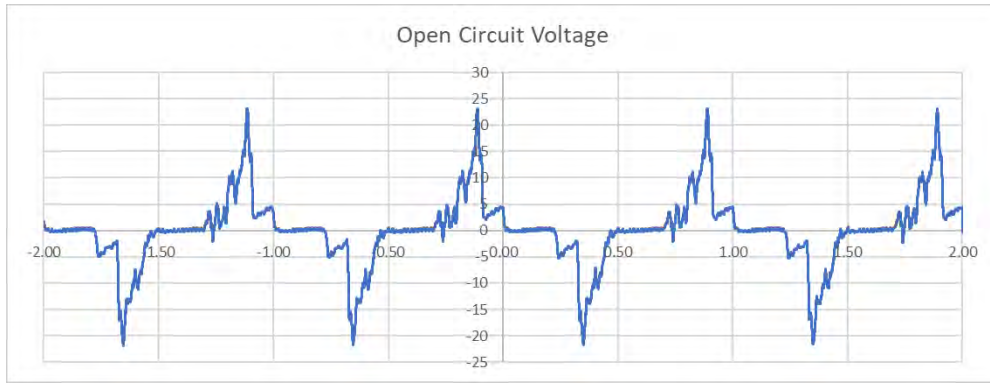


Figure 53 Open circuit voltage for SF-TENG Starch/NP-BTO 0.75% w/w Composite (f=1Hz)

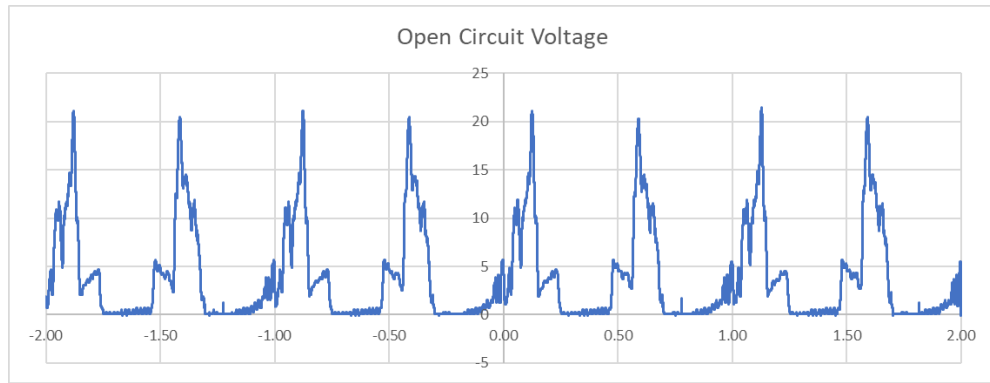


Figure 54 Rectified Open circuit voltage for SF-TENG Starch/NP-BTO 0.75% w/w Composite (f=1Hz)

In the context of the random motion test, we have observed a consistent adherence to the previously recorded trend, resulting in the generation of significantly high voltages, as illustrated in the graphs. It is important to note that we have recorded voltage peaks of up to 276 volts. This remarkable voltage elevation is primarily attributed to the increase in charge density within the material of the freestanding layer during the initial tests conducted without the use of the FRB (full bridge rectifier).

During these initial tests, the material of the freestanding layer accumulates a higher charge density, which subsequently leads to an increased voltage output when we conduct tests with the FRB. This phenomenon occurs because, by the time we employ the FRB, the freestanding layer has accumulated sufficient charge, thereby contributing to the detection of even higher voltage peaks.

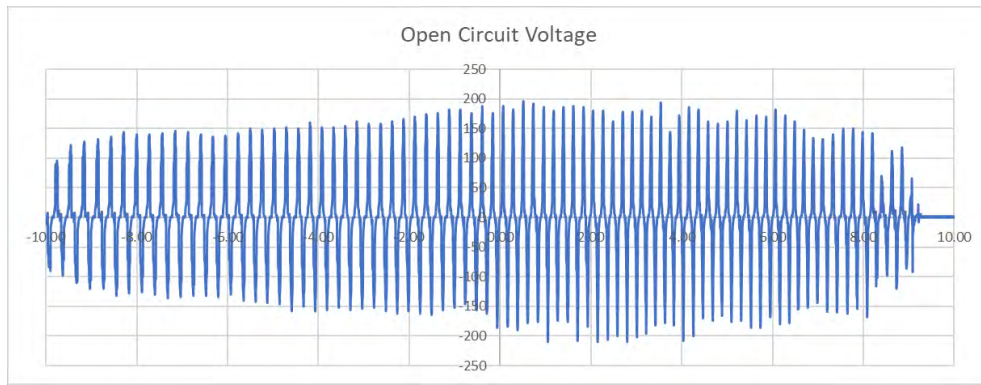


Figure 55 Open circuit voltage for SF-TENG Starch/NP-BTO 0.75% w/w Composite (Random Movements)

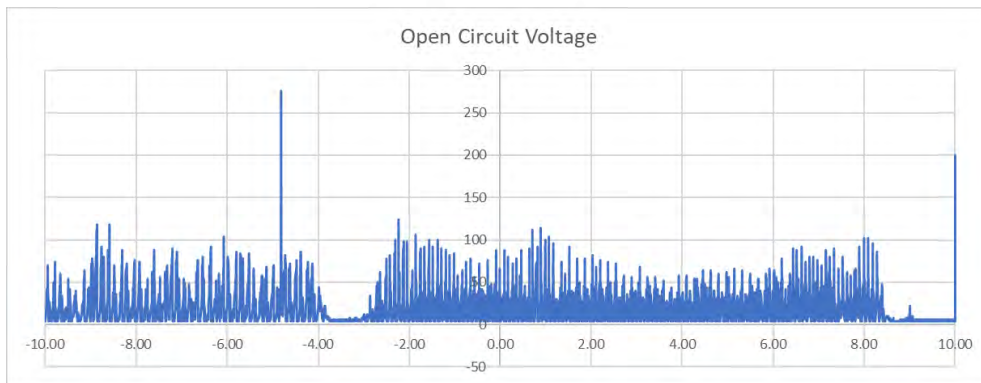


Figure 56 Rectified Open circuit voltage for SF-TENG Starch/NP-BTO 0.75% w/w Composite (Random Movements)

SF-TENG Starch/NP-BTO 1.00% w/w Composite

In the case of the last composite sample 1% BTO, voltage readings exhibit a notable range from 20.3 V to -22.3 V. However, when readings are taken with the FRB (Full Bridge Rectifier), an intriguing phenomenon occurs where the negative portion of the signal reflects onto the positive, resulting in peak values reaching up to 23.4 V.

It's worth noting that diode bridge rectifiers like the FRB are passive components in the circuit, meaning they do not actively amplify the signal. Instead, the increase in voltages can be attributed to the gradually rising charge density over time and the constant friction within the system.

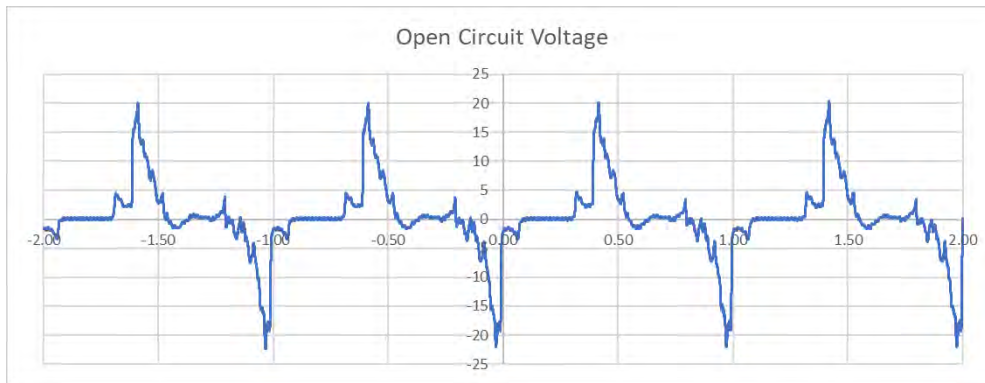


Figure 57 Open circuit voltage for SF-TENG Starch/NP-BTO 1.00% w/w Composite (f=1Hz)

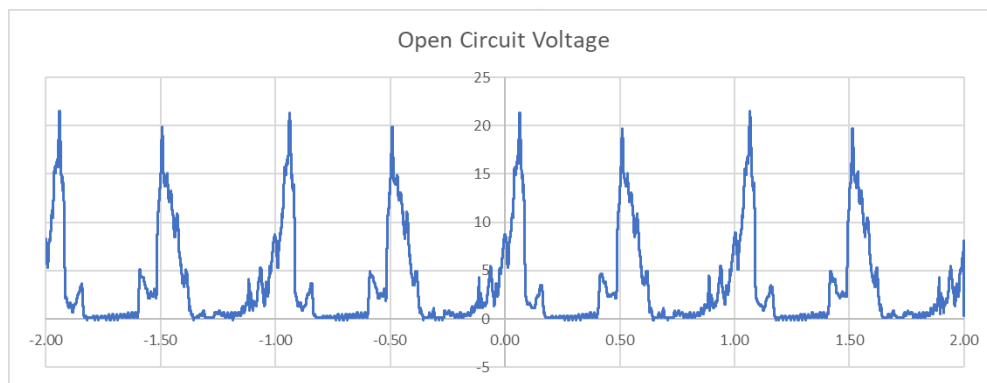


Figure 58 Rectified Open circuit voltage for SF-TENG Starch/NP-BTO 1.00% w/w Composite (f=1Hz)

When voltage readings were taken while operating the TENG (Triboelectric Nanogenerator) with random movements, voltages exceeding the measurement range of the oscilloscope were reached, indicating values beyond the 456V limit. To capture readings of higher voltages, the use of high-voltage probes would be necessary. Consequently, in this study, it was not feasible to determine an upper voltage limit for this SF TENG.

It is advisable to conduct further experiments of this nature, taking into consideration measurement instruments with greater capacity. These experiments underscore the potential applicability of this type of SF TENG for the generation of high voltages.

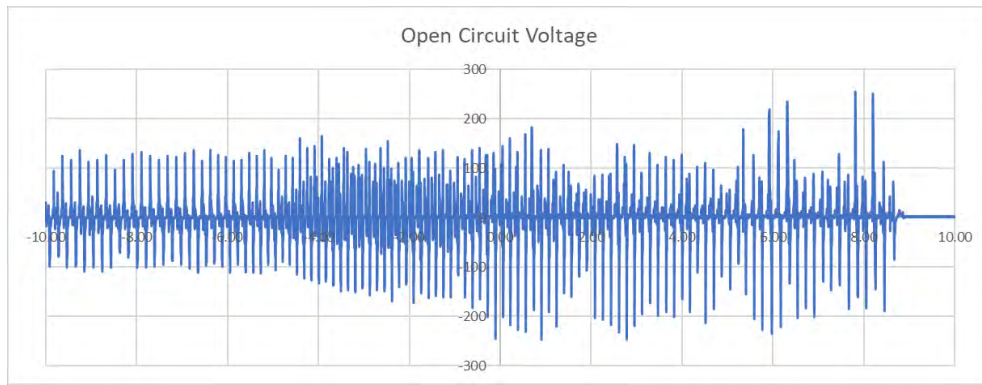


Figure 59 Open circuit voltage for SF-TENG Starch/NP-BTO 1.00% w/w Composite (Random Movements)

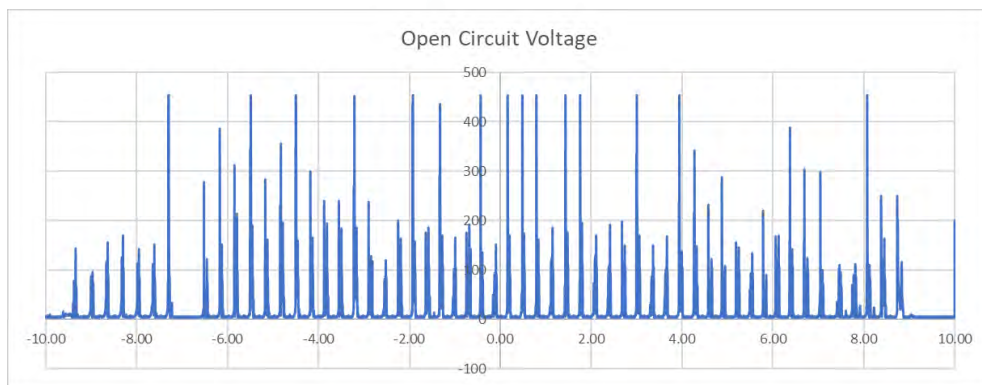


Figure 60 Rectified Open circuit voltage for SF-TENG Starch/NP-BTO 1.00% w/w Composite (Random Movements)

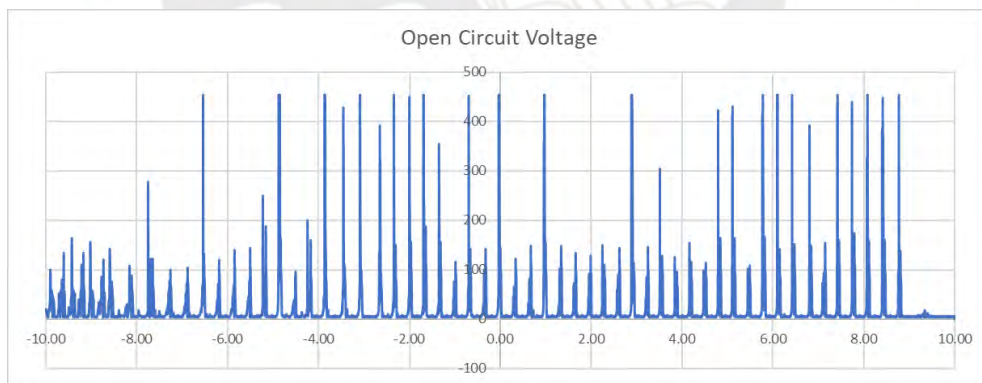


Figure 61 Rectified Open circuit voltage for SF-TENG Starch/NP-BTO 1.00% w/w Composite (Random Movements)

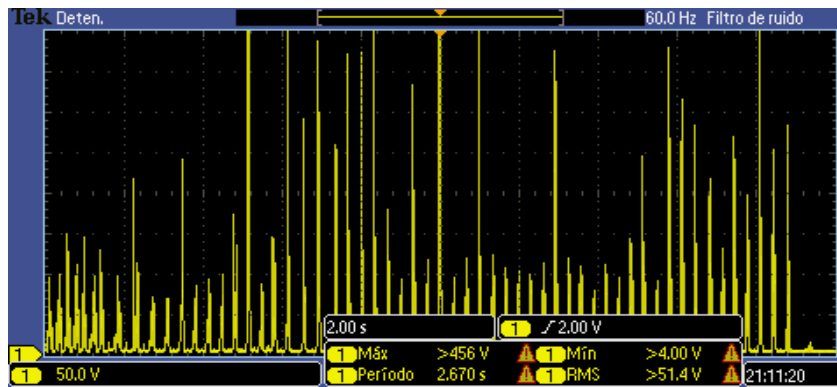


Figure 62 Voltage Measurements taken by Oscilloscope DPO2022

3.4.2 Short Circuit Current

FS-TENG Pristine Starch Freestanding Layer

In the case of short-circuit current measurements, an expected alternating behavior aligned with the movement was anticipated. Due to the inherent nature of Triboelectric Nanogenerators (TENGs) to provide low currents, in the instance of pure starch, we observed current values oscillating between peaks of $2.06 \mu\text{A}$ and $-1.78 \mu\text{A}$.

Interestingly, when integrated into the circuit, the Full Bridge Rectifier (FBR) exhibited a similar pattern as the voltage, converting negative currents into positive ones. As a result, a slight increase was observed, reaching up to $2.22 \mu\text{A}$. Once again, this phenomenon can be attributed to the increasing charge density over time

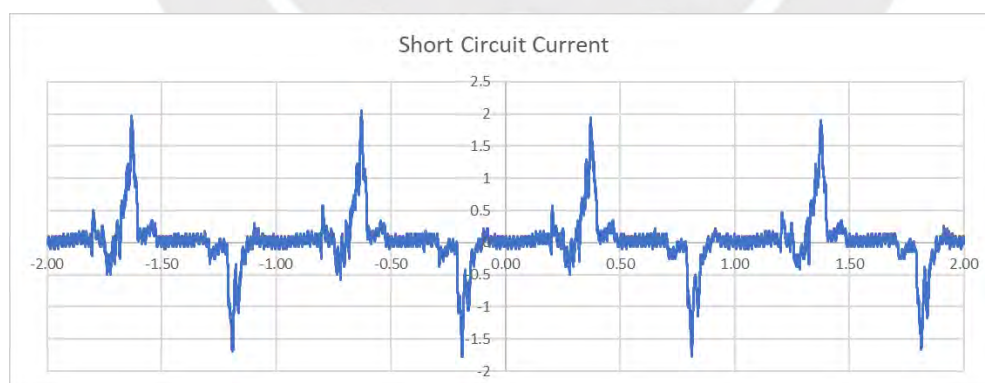


Figure 63 Short circuit current for FS-TENG Pristine Starch ($f=1\text{Hz}$)

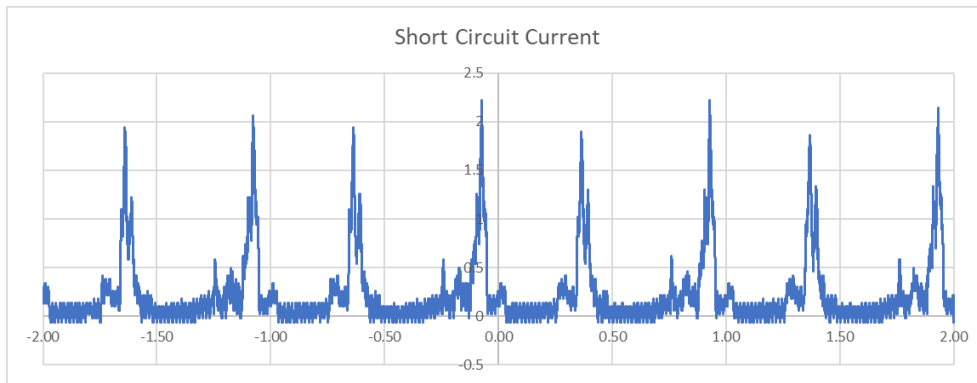


Figure 64 Rectified Short circuit current for -SF-TENG Pristine Starch (f=1Hz)

SF-TENG Starch/NP-BTO 0.25% w/w Composite

As observed during the current measurements for this Sliding Freestanding Triboelectric Nanogenerator (SF-TENG), the current values exhibit a notable decrease compared to the pristine starch layer. These current values fluctuate within a range, oscillating between peaks of $1.78 \mu\text{A}$ and $-1.82 \mu\text{A}$.

Interestingly, when an FRB (Full Bridge Rectifier) is introduced into the circuit, we observe a slight increase in current values, reaching $1.94 \mu\text{A}$. It's essential to clarify that the primary function of the FRB is not to amplify current but to rectify it. In this context, the FRB converts the alternating current (AC) generated by the SF-TENG into a unidirectional or direct current (DC), effectively eliminating the negative portions of the current waveform.

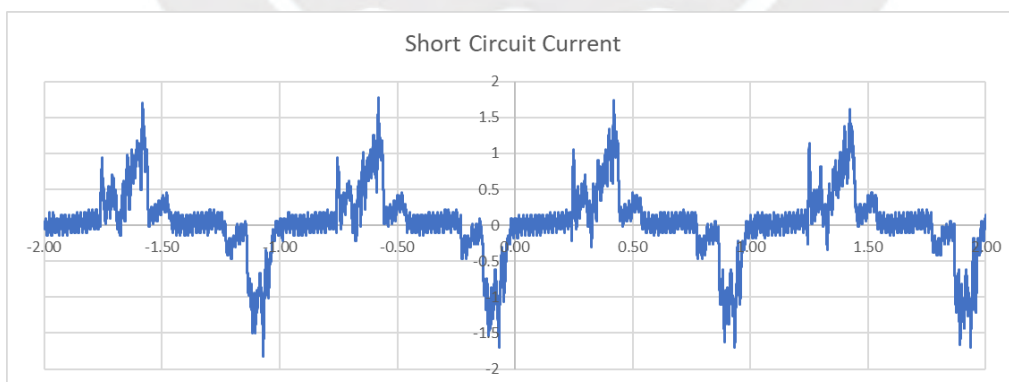


Figure 65 Short circuit current for SF-TENG Starch/NP-BTO 0.25% w/w Composite (f=1Hz)

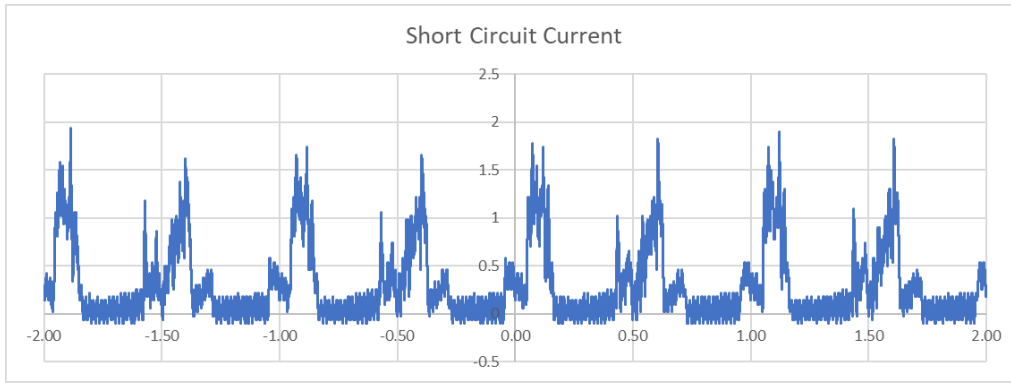


Figure 66 Rectified Short circuit current for SF-TENG Starch/NP-BTO 0.25% w/w Composite (f=1Hz)

SF-TENG Starch/NP-BTO 0.50% w/w Composite

As expected, given the significant reduction in voltage behavior observed for this freestanding layer, a corresponding decrease in current generation was also evident, with alternating peak values ranging from 1.17 μA to -0.99 μA .

This decline in current is closely linked to the surface irregularities present on the freestanding layer, as previously discussed in the context of voltage analysis. Surface imperfections can impact the efficiency of triboelectric charge generation by disrupting the necessary friction and separation processes required to induce charge transfer.

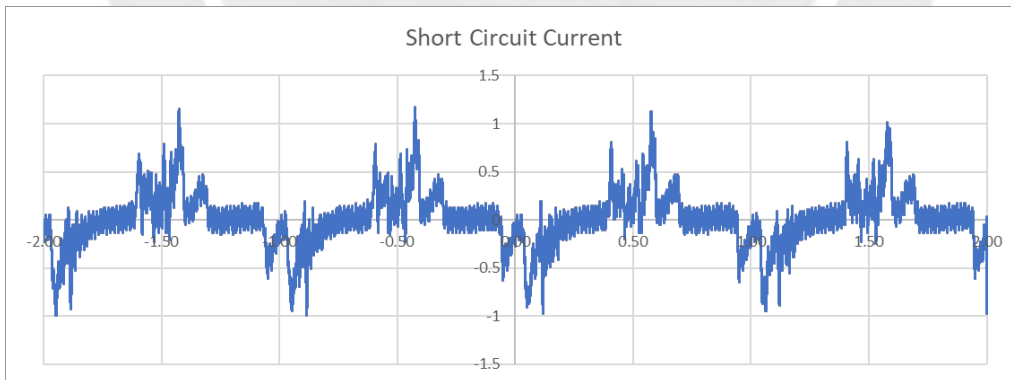


Figure 67 Short circuit current for SF-TENG Starch/NP-BTO 0.50% w/w Composite (f=1Hz)

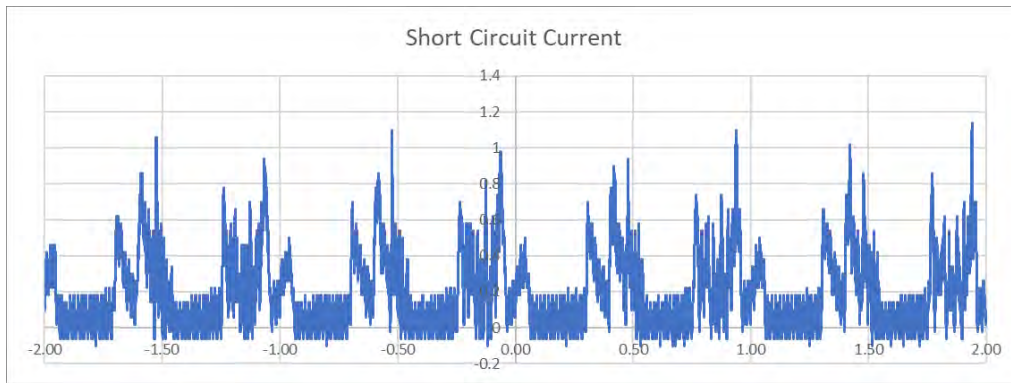


Figure 68 Rectified Short circuit current for SF-TENG Starch/NP-BTO 0.50% w/w Composite (f=1Hz)

SF-TENG Starch/NP-BTO 0.75% w/w Composite

In the freestanding layer of the composite material containing 0.75% BTO, an increase in current values was evident compared to pristine starch, with currents ranging between 2.46 μA and -2.3 μA . When the Full Bridge Rectifier (FBR) was utilized, it produced a peak current of 2.42 μA .

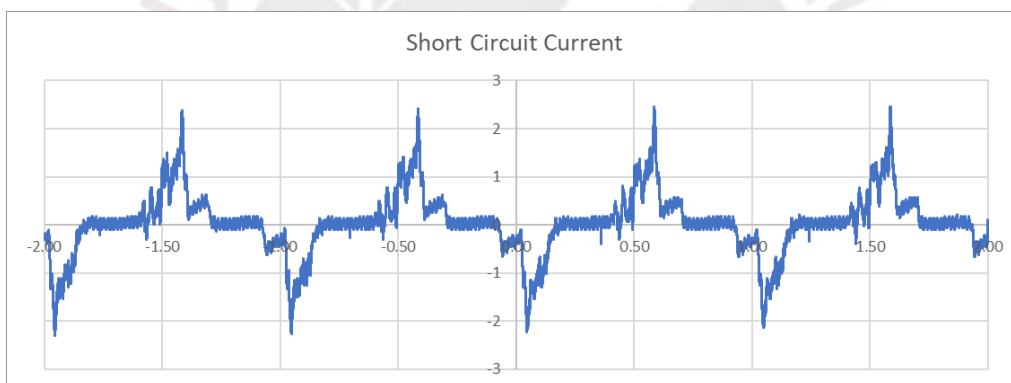


Figure 69 Short circuit current for SF-TENG Starch/NP-BTO 0.75% w/w Composite (f=1Hz)

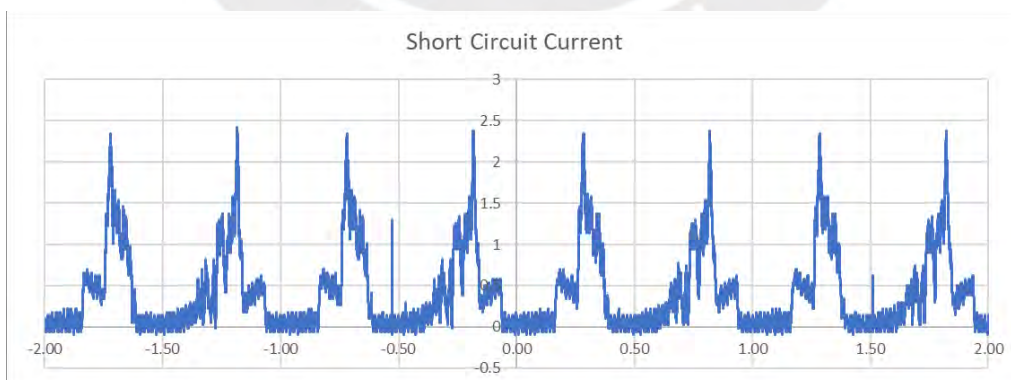


Figure 70 Rectified Short circuit current for SF-TENG Starch/NP-BTO 0.75% w/w Composite (f=1Hz)

SF-TENG Starch/NP-BTO 1.00% w/w Composite

Regarding the final composite material layer containing 1.00% BTO, the short-circuit current remains slightly higher than that of pure starch, with values oscillating between 2.14 μA and -1.86 μA .

Thus, it has become evident that the increase in voltages was more pronounced when the dielectric constant was augmented compared to the current. This observation suggests that the effect of the dielectric permittivity on voltages is greater when compared to its influence on currents.

This phenomenon aligns with the expected behavior in dielectric materials, where a higher dielectric constant enhances the material's ability to store electric potential energy. Consequently, this can result in a more substantial impact on voltage generation than on current flow.

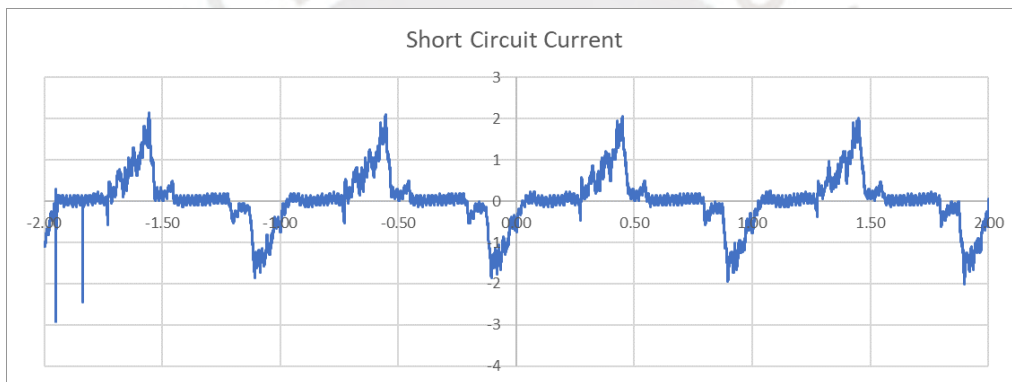


Figure 71 Short circuit current for SF-TENG Starch/NP-BTO 1.00% w/w Composite ($f=1\text{Hz}$)

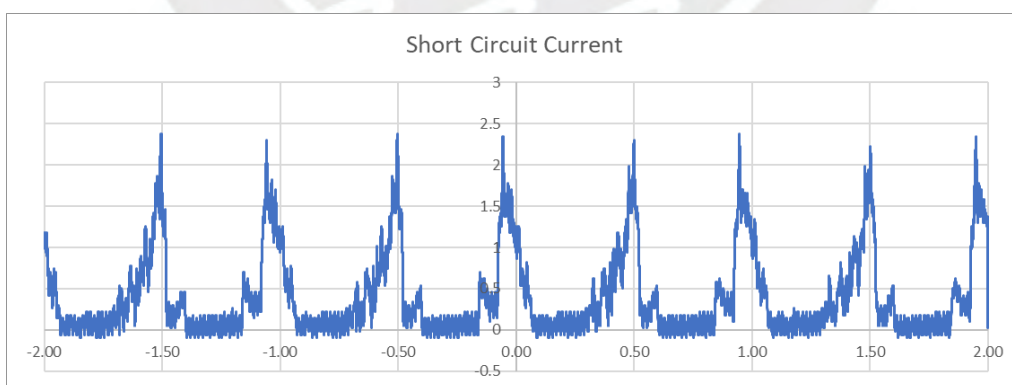


Figure 72 Rectified Short circuit current for SF-TENG Starch/NP-BTO 1.00% w/w Composite ($f=1\text{Hz}$)

3.4.3 Capacitor Charging

A series of experimental tests were undertaken to assess the charging characteristics of capacitors with varying capacitances. Notably, it was observed that the charging times exhibited a slight increase when charging a capacitor with a capacitance of 3.4 μ F. Concurrently, the maximum charging voltage displayed variability across different layers of composite materials. Specifically, the highest recorded voltage, amounting to 2.3V, was achieved in the case of a starch layer containing 1.00% by weight of BaTiO₃ nanoparticles, with an associated charging duration of 100 seconds. In contrast, pristine starch exhibited lower voltage values, reaching a maximum of 1.4V, but required a longer charging time of 200 seconds. These findings underscore the intricate interplay between material composition, charging time, and voltage attainment in the examined capacitor system.

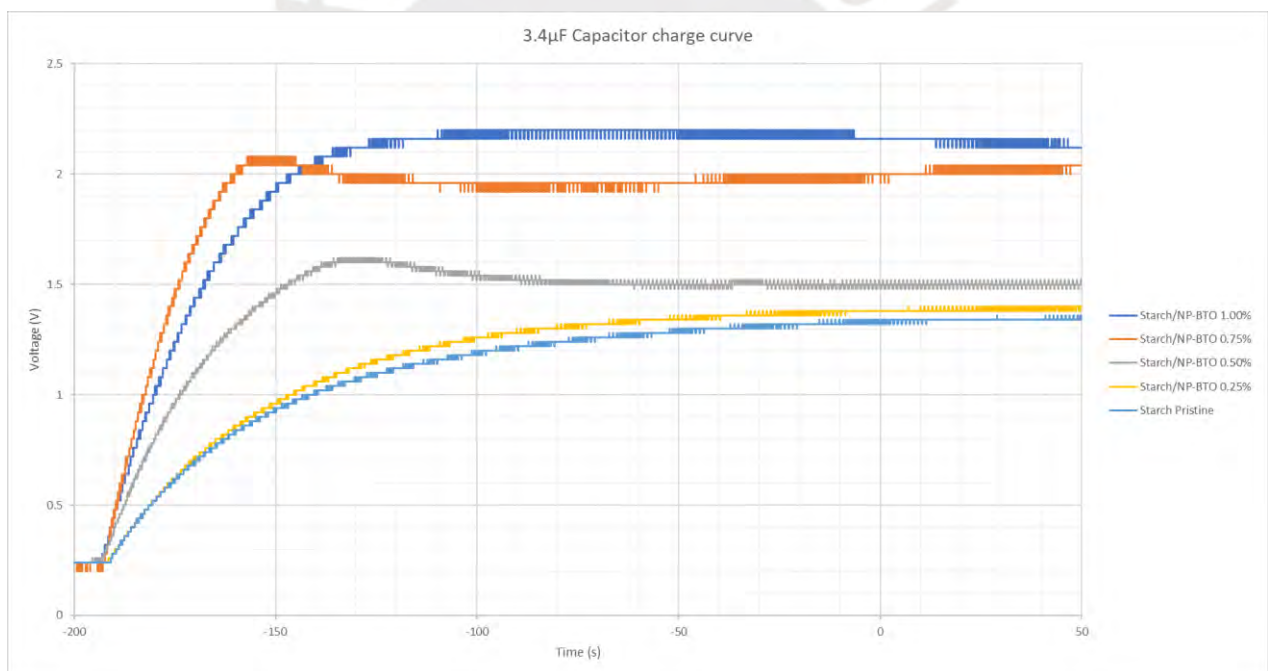


Figure 73 Starch/Composite Freestanding layers charging 3.4 μ F Capacitor

Summary

The electrical results demonstrate a dominant frequency of approximately 1 Hz in the open circuit voltage, which is confirmed through FFT analysis. Notably, a gradual charge accumulation in the SF-TENG over time leads to increased voltages after the application of the Full Bridge Rectifier (FRB).

When manual oscillatory motions are applied to the system, significantly higher

voltages are achieved, reaching values as low as -251.00 volts. The use of an FRB amplifies these values to 452 volts, underscoring the critical influence of controlled pressure and frequency modulation on voltage generation.

Furthermore, the results indicate that the increase in voltages is more pronounced when the dielectric constant is augmented, highlighting the significant impact of dielectric permittivity on voltage generation compared to its influence on currents. This aligns with the expected behaviour in dielectric materials, where a higher dielectric constant enhances the material's ability to store electric potential energy, resulting in a more substantial impact on voltage generation than on current flow. These findings have important implications for optimizing the SF-TENG system.

In addition, a summary table displaying the maximum voltage and current values achieved during the experiments is presented below

Table 4 : Maximum FS-Teng outputs registered

		Frequency: 1Hz				
		Pristine.Starch.1	Composite0.25	Composite0.50	Composite0.75	Composite1.00
Voc (V)		17.50	14.50	9.90	23.00	23.00
Isc (uA)		2.02	1.78	1.11	2.30	2.30
Vcap (V)	100nF	1.46	1.70	2.57	4.92	3.80
	1mF	1.16	1.42	1.67	2.36	2.16
		Frequency: Random movements				
Voc (V)		256.00	396.00	250.00	224.00	>456.00

CONCLUSIONS

In conclusion, the primary objective of this study has been successfully accomplished through the development of a composite material derived from biopolymers and inorganic fillers. This composite material was designed for utilization as a triboelectric surface, facilitating the creation of a highly efficient triboelectric nanogenerator (TENG). The specific objectives encompassed the extraction of biopolymers from natural resources, specifically potatoes, and the comprehensive characterization of the electrical, physicochemical, and morphological properties of the resulting composite materials.

The investigations have revealed that these composite materials possess highly desirable properties, including remarkable dielectric permittivity (ϵ') values. For instance, at a frequency of 1 Hz, the composite material with a filler ratio of 0.50 exhibited an ϵ' value of 3,777,800, signifying its outstanding dielectric characteristics. Additionally, the ϵ'' values, representing the imaginary component of the permittivity, were also notable. The composite material with a filler ratio of 0.50 displayed an ϵ'' value of 3,078,580 at 1 Hz.

Regarding the electrical performance of the triboelectric nanogenerator (TENG), it demonstrated impressive voltage outputs as well. At a frequency of 1 Hz, the TENG achieved a peak V_{oc} (open-circuit voltage) of 23.00 V and a peak I_{sc} (short-circuit current) of 2.30 μ A. During random movements, the TENG attained remarkable voltage outputs, with a V_{oc} exceeding 456.00 V, underscoring its exceptional capability for voltage generation.

These remarkable dielectric properties, combined with the excellent electrical performance of the triboelectric nanogenerator, underscore the immense potential of these materials for energy harvesting applications. The investigation into both dielectric properties and voltage outputs is a valuable contribution to the broader field of materials science and energy harvesting.

Future research endeavors can explore opportunities to further optimize the properties of composite materials and refine the design of the TENG to achieve even greater levels of performance and efficiency while leveraging the exceptional dielectric properties exhibited by these materials.

BIBLIOGRAPHY

- [1] Zhang T, Yang H. High efficiency plants and building integrated renewable energy systems: Building-integrated photovoltaics (BIPV). *Handbook of Energy Efficiency in Buildings: A Life Cycle Approach*, Elsevier; 2018, p. 441–595. <https://doi.org/10.1016/B978-0-12-812817-6.00040-1>.
- [2] Mostafa MH, Abdel Aleem SHE, Ali SG, Abdelaziz AY. Energy-management solutions for microgrids. *Distributed Energy Resources in Microgrids: Integration, Challenges and Optimization*, Elsevier; 2019, p. 483–515. <https://doi.org/10.1016/B978-0-12-817774-7.00020-X>.
- [3] Patade VY, Meher LC, Grover A, Gupta SM, Nasim M. Omics approaches in biofuel technologies: Toward cost effective, eco-friendly, and renewable energy. *Omics Technologies and Bio-engineering: Volume 2: Towards Improving Quality of Life*, Elsevier; 2018, p. 337–51. <https://doi.org/10.1016/B978-0-12-815870-8.00018-8>.
- [4] Li X, Jiang C, Ying Y, Ping J. Biotriboelectric Nanogenerators: Materials, Structures, and Applications. *Adv Energy Mater* 2020;10. <https://doi.org/10.1002/aenm.202002001>.
- [5] Beeby SP, Cao Z, Almussallam A. Kinetic, thermoelectric and solar energy harvesting technologies for smart textiles. *Multidisciplinary Know-How for Smart-Textiles Developers*, Elsevier Ltd; 2013, p. 306–28. <https://doi.org/10.1533/9780857093530.2.306>.
- [6] Wang ZL. Triboelectric nanogenerators as new energy technology for self-powered systems and as active mechanical and chemical sensors. *ACS Nano* 2013;7:9533–57. <https://doi.org/10.1021/nn404614z>.
- [7] Wang ZL, Jiang T, Xu L. Toward the blue energy dream by triboelectric nanogenerator networks. *Nano Energy* 2017;39:9–23. <https://doi.org/10.1016/j.nanoen.2017.06.035>.
- [8] Zhang JXJ, Hoshino K. Implantable Sensors. *Molecular Sensors and Nanodevices*, Elsevier; 2014, p. 415–65. <https://doi.org/10.1016/b978-1-4557-7631-3.00007-7>.
- [9] Zheng Q, Shi B, Li Z, Wang ZL. Recent Progress on Piezoelectric and Triboelectric Energy Harvesters in Biomedical Systems. *Advanced Science* 2017;4. <https://doi.org/10.1002/advs.201700029>.
- [10] Wang ZL. Triboelectric Nanogenerator (TENG)—Sparking an Energy and Sensor Revolution. *Adv Energy Mater* 2020;10. <https://doi.org/10.1002/aenm.202000137>.
- [11] Chen A, Zhang C, Zhu G, Wang ZL. Polymer Materials for High-Performance Triboelectric Nanogenerators. *Advanced Science* 2020;7. <https://doi.org/10.1002/advs.202000186>.
- [12] Kim DW, Lee JH, Kim JK, Jeong U. Material aspects of triboelectric energy generation and sensors. *NPG Asia Mater* 2020;12. <https://doi.org/10.1038/s41427-019-0176-0>.
- [13] Zhang R, Olin H. Material choices for triboelectric nanogenerators: A critical review. *EcoMat* 2020;2. <https://doi.org/10.1002/eom2.12062>.
- [14] Shao JJ, Jiang T, Wang ZL. Theoretical foundations of triboelectric nanogenerators (TENGs). *Sci China Technol Sci* 2020;63:1087–109. <https://doi.org/10.1007/s11431-020-1604-9>.

- [15] Ahmed A, Hassan I, El-Kady MF, Radhi A, Jeong CK, Selvaganapathy PR, et al. Integrated Triboelectric Nanogenerators in the Era of the Internet of Things. *Advanced Science* 2019;6. <https://doi.org/10.1002/advs.201802230>.
- [16] Pan S, Zhang Z. Fundamental theories and basic principles of triboelectric effect: A review. *Friction* 2019;7:2–17. <https://doi.org/10.1007/s40544-018-0217-7>.
- [17] Lowell J. The role of material transfer in contact electrification. vol. 10. 1977.
- [18] Wang ZL, Wang AC. On the origin of contact-electrification. *Materials Today* 2019;30:34–51. <https://doi.org/10.1016/j.mattod.2019.05.016>.
- [19] Shen X, Wang AE, Sankaran RM, Lacks DJ. First-principles calculation of contact electrification and validation by experiment. *J Electrostat* 2016;82:11–6. <https://doi.org/10.1016/j.elstat.2016.04.006>.
- [20] Baytekin HT, Patashinski AZ, Branicki M, Baytekin B, Soh S, Grzybowski BA. The mosaic of surface charge in contact electrification. *Science (1979)* 2011;333:308–12. <https://doi.org/10.1126/science.1201512>.
- [21] Sobolev YI, Adamkiewicz W, Siek M, Grzybowski BA. Charge mosaics on contact-electrified dielectrics result from polarity-inverting discharges. *Nat Phys* 2022;18:1347–55. <https://doi.org/10.1038/s41567-022-01714-9>.
- [22] Rathore S, Sharma S, Swain BP, Ghadai RK. A Critical Review on Triboelectric Nanogenerator. *IOP Conf Ser Mater Sci Eng*, vol. 377, Institute of Physics Publishing; 2018. <https://doi.org/10.1088/1757-899X/377/1/012186>.
- [23] Lowell J, Rose-Innes AC. Contact electrification. *Adv Phys* 1980;29:947–1023. <https://doi.org/10.1080/00018738000101466>.
- [24] Duke CB, Fabish TJ. Contact electrification of polymers: A quantitative model. *J Appl Phys* 1978;49:315–21. <https://doi.org/10.1063/1.324388>.
- [25] Willatzen M, Lew Yan Voon LC, Wang ZL. Quantum Theory of Contact Electrification for Fluids and Solids. *Adv Funct Mater* 2020;30. <https://doi.org/10.1002/adfm.201910461>.
- [26] Wang ZL. On the first principle theory of nanogenerators from Maxwell's equations. *Nano Energy* 2020;68. <https://doi.org/10.1016/j.nanoen.2019.104272>.
- [27] Somkuwar VU, Pragya A, Kumar B. Structurally engineered textile-based triboelectric nanogenerator for energy harvesting application. *J Mater Sci* 2020;55:5177–89. <https://doi.org/10.1007/s10853-020-04359-2>.
- [28] Zhang R, Örtengren J, Hummelgård M, Olsen M, Andersson H, Olin H. A review of the advances in composites/nanocomposites for triboelectric nanogenerators. *Nanotechnology* 2022;33. <https://doi.org/10.1088/1361-6528/ac4b7b>.
- [29] Kim WG, Kim DW, Tcho IW, Kim JK, Kim MS, Choi YK. Triboelectric Nanogenerator: Structure, Mechanism, and Applications. *ACS Nano* 2021;15:258–87. <https://doi.org/10.1021/acsnano.0c09803>.
- [30] Zi Y, Wu C, Ding W, Wang ZL. Maximized Effective Energy Output of Contact-Separation-Triggered Triboelectric Nanogenerators as Limited by Air Breakdown. *Adv Funct Mater* 2017;27. <https://doi.org/10.1002/adfm.201700049>.

- [31] Wu F, Li C, Yin Y, Cao R, Li H, Zhang X, et al. A Flexible, Lightweight, and Wearable Triboelectric Nanogenerator for Energy Harvesting and Self-Powered Sensing. *Adv Mater Technol* 2019;4. <https://doi.org/10.1002/admt.201800216>.
- [32] He W, Fu X, Zhang D, Zhang Q, Zhuo K, Yuan Z, et al. Recent progress of flexible/wearable self-charging power units based on triboelectric nanogenerators. *Nano Energy* 2021;84. <https://doi.org/10.1016/j.nanoen.2021.105880>.
- [33] Kim SM, Ha J, Kim JB. Theoretical study of contact-mode triboelectric nanogenerators: Analytical and numerical study. *Integrated Ferroelectrics* 2017;183:54–9. <https://doi.org/10.1080/10584587.2017.1375821>.
- [34] Niu S, Liu Y, Wang S, Lin L, Zhou YS, Hu Y, et al. Theory of sliding-mode triboelectric nanogenerators. *Advanced Materials* 2013;25:6184–93. <https://doi.org/10.1002/adma.201302808>.
- [35] Niu S, Liu Y, Chen X, Wang S, Zhou YS, Lin L, et al. Theory of freestanding triboelectric-layer-based nanogenerators. *Nano Energy* 2015;12:760–74. <https://doi.org/10.1016/j.nanoen.2015.01.013>.
- [36] Wang Y, Jie W, Yang C, Wei X, Hao J. Colossal Permittivity Materials as Superior Dielectrics for Diverse Applications. *Adv Funct Mater* 2019;29. <https://doi.org/10.1002/adfm.201808118>.
- [37] Lee JW, Cho HJ, Chun J, Kim KN, Kim S, Ahn CW, et al. APPLIED SCIENCES AND ENGINEERING Robust nanogenerators based on graft copolymers via control of dielectrics for remarkable output power enhancement. n.d.
- [38] Min G, Xu Y, Cochran P, Gadegaard N, Mulvihill DM, Dahiya R. Origin of the contact force-dependent response of triboelectric nanogenerators. *Nano Energy* 2021;83. <https://doi.org/10.1016/j.nanoen.2021.105829>.
- [39] Paosangthong W, Torah R, Beeby S. Recent progress on textile-based triboelectric nanogenerators. *Nano Energy* 2019;55:401–23. <https://doi.org/10.1016/j.nanoen.2018.10.036>.
- [40] Tang Q, Guo H, Yan P, Hu C. Recent progresses on paper-based triboelectric nanogenerator for portable self-powered sensing systems. *EcoMat* 2020;2. <https://doi.org/10.1002/eom2.12060>.
- [41] Zou H, Zhang Y, Guo L, Wang P, He X, Dai G, et al. Quantifying the triboelectric series. *Nat Commun* 2019;10. <https://doi.org/10.1038/s41467-019-09461-x>.
- [42] Ohsawa A. Statistical analysis of fires and explosions attributed to static electricity over the last 50 years in Japanese industry. *J Phys Conf Ser*, vol. 301, Institute of Physics Publishing; 2011. <https://doi.org/10.1088/1742-6596/301/1/012033>.
- [43] Levit L, Steinman A. ESD Controls in Cleanroom Environments: Relevance to Particle Deposition. *Developments in Surface Contamination and Cleaning: Second Edition*, vol. 1, Elsevier Inc.; 2008, p. 173–95. <https://doi.org/10.1016/B978-0-323-29960-2.00006-X>.
- [44] Hu Y, Wang D, Liu J, Gao J. A case study of electrostatic accidents in the process of oil-gas storage and transportation. *J Phys Conf Ser*, vol. 418, Institute of Physics Publishing; 2013. <https://doi.org/10.1088/1742-6596/418/1/012037>.

- [45] Kikunaga K, Terasaki N. Demonstration of static electricity induced luminescence. *Sci Rep* 2022;12. <https://doi.org/10.1038/s41598-022-12704-5>.
- [46] Liu S, Zheng W, Yang B, Tao X. Triboelectric charge density of porous and deformable fabrics made from polymer fibers. *Nano Energy* 2018;53:383–90. <https://doi.org/10.1016/j.nanoen.2018.08.071>.
- [47] Seol M, Kim S, Cho Y, Byun KE, Kim H, Kim J, et al. Triboelectric Series of 2D Layered Materials. *Advanced Materials* 2018;30. <https://doi.org/10.1002/adma.201801210>.
- [48] Luo J, Wang ZL. Recent progress of triboelectric nanogenerators: From fundamental theory to practical applications. *EcoMat* 2020;2. <https://doi.org/10.1002/eom2.12059>.
- [49] Sridhar R, Lakshminarayanan R, Madhaiyan K, Barathi VA, Limh KHC, Ramakrishna S. Electrosprayed nanoparticles and electrospun nanofibers based on natural materials: Applications in tissue regeneration, drug delivery and pharmaceuticals. *Chem Soc Rev* 2015;44:790–814. <https://doi.org/10.1039/c4cs00226a>.
- [50] Li C, Yin Y, Wang B, Zhou T, Wang J, Luo J, et al. Self-Powered Electrospinning System Driven by a Triboelectric Nanogenerator. *ACS Nano* 2017;11:10439–45. <https://doi.org/10.1021/acsnano.7b05626>.
- [51] Tao K, Chang H, Wu J, Tang L, Miao J. MEMS/NEMS-enabled energy harvesters as self-powered sensors. *SpringerBriefs in Applied Sciences and Technology*, Springer Verlag; 2019, p. 1–30. https://doi.org/10.1007/978-3-030-05554-7_1.
- [52] Yang H, Pang Y, Bu T, Liu W, Luo J, Jiang D, et al. Triboelectric micromotors actuated by ultralow frequency mechanical stimuli. *Nat Commun* 2019;10. <https://doi.org/10.1038/s41467-019-10298-7>.
- [53] Chen J, Yang B, Lim YD, Su L, Yang J, Guo R, et al. Field emission cathode based on three-dimensional framework carbon and its operation under the driving of a triboelectric nanogenerator. *Nano Energy* 2018;49:308–15. <https://doi.org/10.1016/j.nanoen.2018.04.052>.
- [54] Zi Y, Wu C, Ding W, Wang X, Dai Y, Cheng J, et al. Field Emission of Electrons Powered by a Triboelectric Nanogenerator. *Adv Funct Mater* 2018;28. <https://doi.org/10.1002/adfm.201800610>.
- [55] Chen J, Lim YD, Zhao Y, Chen J, Yang B, Wu Z, et al. Triboelectric Nanogenerator Driven Carbon Nanotube Cathode: A Sustainable Self-Powering Electron Source. *ACS Appl Electron Mater* 2021;3:476–84. <https://doi.org/10.1021/acsaelm.0c01029>.
- [56] Xiang H, Li Z, Liu H, Chen T, Zhou H, Huang W. Green flexible electronics based on starch. *Npj Flexible Electronics* 2022;6. <https://doi.org/10.1038/s41528-022-00147-x>.
- [57] Torres FG, Troncoso OP, Díaz DA, Amaya E. Morphological and thermal characterization of native starches from Andean crops. *Starch/Staerke* 2011;63:381–9. <https://doi.org/10.1002/star.201000155>.
- [58] Torres FG, Troncoso OP, Grande CG, Díaz DA. Biocompatibility of starch-based films from starch of Andean crops for biomedical applications. *Materials Science and Engineering C* 2011;31:1737–40. <https://doi.org/10.1016/j.msec.2011.08.004>.

- [59] Li H, Xu M, Shi R, Zhang A, Zhang J. Advances in Electrostatic Spinning of Polymer Fibers Functionalized with Metal-Based Nanocrystals and Biomedical Applications. *Molecules* 2022;27. <https://doi.org/10.3390/molecules27175548>.
- [60] Tuzlakoglu K, Pashkuleva I, Rodrigues MT, Gomes ME, Van Lenthe GH, Müller R, et al. A new route to produce starch-based fiber mesh scaffolds by wet spinning and subsequent surface modification as a way to improve cell attachment and proliferation. *J Biomed Mater Res A* 2010;92. <https://doi.org/10.1002/jbm.a.32358>.
- [61] Maniglia BC, Fahmy AR, Jekle M, Le-Bail P, Le-Bail A. Three-Dimensional (3D) Food Printing Based on Starch-Based Inks: Crucial Factors for Printing Precision. *Food Printing: 3D Printing in Food Industry*, 2022. https://doi.org/10.1007/978-981-16-8121-9_7.
- [62] Torres FG, Troncoso OP, Torres C, Díaz DA, Amaya E. Biodegradability and mechanical properties of starch films from Andean crops. *Int J Biol Macromol* 2011;48:603–6. <https://doi.org/10.1016/j.ijbiomac.2011.01.026>.
- [63] Gómez C, Torres FG, Nakamatsu J, Arroyo OH. Thermal and structural analysis of natural fiber reinforced starch-based biocomposites. *International Journal of Polymeric Materials and Polymeric Biomaterials* 2006;55:893–907. <https://doi.org/10.1080/00914030500522547>.
- [64] Alsufyani T, M'sakni NH. Part A: Biodegradable Bio-Composite Film Reinforced with Cellulose Nanocrystals from *Chaetomorpha linum* into Thermoplastic Starch Matrices. *Polymers (Basel)* 2023;15. <https://doi.org/10.3390/polym15061542>.
- [65] Zhang R, Olin H. Advances in Inorganic Nanomaterials for Triboelectric Nanogenerators. *ACS Nanoscience Au* 2022;2:12–31. <https://doi.org/10.1021/acsnanoscienceau.1c00026>.
- [66] Shao Y, Feng C ping, Deng B wen, Yin B, Yang M bo. Facile method to enhance output performance of bacterial cellulose nanofiber based triboelectric nanogenerator by controlling micro-nano structure and dielectric constant. *Nano Energy* 2019;62:620–7. <https://doi.org/10.1016/j.nanoen.2019.05.078>.
- [67] Luo G, Zhang G, Zhang Y, Li A, Sun Y, Tu R, et al. Wide temperature range of stable dielectric properties in relaxor BaTiO₃-based ceramics by co-doping synergistic engineering. *Mater Chem Phys* 2023;302. <https://doi.org/10.1016/j.matchemphys.2023.127629>.
- [68] Tse MY, Wei X, Wong CM, Huang LB, Lam KH, Dai J, et al. Enhanced dielectric properties of colossal permittivity co-doped TiO₂/polymer composite films. *RSC Adv* 2018;8:32972–8. <https://doi.org/10.1039/c8ra07401a>.
- [69] Yang C, Tse MY, Wei X, Hao J. Colossal permittivity of (Mg + Nb) co-doped TiO₂ ceramics with low dielectric loss. *J Mater Chem C Mater* 2017;5:5170–5. <https://doi.org/10.1039/c7tc01020f>.
- [70] Arbatti M, Shan X, Cheng Z. Ceramic-polymer composites with high dielectric constant. *Advanced Materials* 2007;19:1369–72. <https://doi.org/10.1002/adma.200601996>.
- [71] Chiang CK, Popielarz R. Polymer Composites with High Dielectric Constant. *Ferroelectrics* 2002;275:1. <https://doi.org/10.1080/00150190190021786>.

- [72] Barber P, Pellechia PJ, Ploehn HJ, Zur Loye HC. High-dielectric polymer composite materials from a series of mixed-metal phenylphosphonates, $ATi(C_6H_5PO_3)_3$ for dielectric energy storage. *ACS Appl Mater Interfaces* 2010;2:2553–9. <https://doi.org/10.1021/am1003987>.
- [73] Mishra P, Bhat BR, Bhattacharya B, Mehra RM. Synthesis and Characterization of High-Dielectric-Constant Nanographite–Polyurethane Composite. *JOM* 2018;70:1302–6. <https://doi.org/10.1007/s11837-018-2877-1>.
- [74] Singh M, Yadav BC, Ranjan A, Kaur M, Gupta SK. Synthesis and characterization of perovskite barium titanate thin film and its application as LPG sensor. *Sens Actuators B Chem* 2017;241:1170–8. <https://doi.org/10.1016/j.snb.2016.10.018>.
- [75] Momin A. Synthesis and characterization of barium titanate ($BaTiO_3$) nanoparticle. vol. 1. 2012.

